ABSTRACT

Title of Dissertation: Contributions to the Measurement and Analysis of Helicopter Blade Tip Vortices

Manikandan Ramasamy, Doctor of Philosophy, 2004

Dissertation directed by: Minta Martin Professor J. Gordon Leishman
Department of Aerospace Engineering

The physical structure and the evolution of helicopter blade tip vortices, particularly the effect of the filament strain and flow rotation effects on the turbulent structure, were investigated through model-scale hovering rotor experiments as well as by developing a mathematical model from the Navier-Stokes (N–S) equations. The flow properties were measured using a high-resolution, three-component Laser Doppler Velocimetry (LDV) system. Images of the tip vortices were also obtained using laser sheet flow visualization.

A strain field on the tip vortices was introduced by placing a solid boundary downstream of the rotor. As the vortices approached this boundary, they were convected radially outwards enabling measurements to be obtained in a known strain field. Comparing these measurements with vortex measurements in free-air provided considerable insight into the interdependence of strain and diffusion and their impact on the

evolution of rotor tip vortices. The measurements also served to validate a mathematical model developed to predict the core growth of the tip vortices, which included the effects of both filament strain and diffusion.

The measurements also laid the groundwork for the development of a comprehensive engineering tip vortex core growth model, which combined the effects of vortex filament strain and Reynolds number effects. Laser sheet flow visualization of the vortex core structure indicated the presence of three distinct regions — an inner laminar region, an intermediate transition region and an outer turbulent region. Analysis of the velocity profiles measured across the vortex core at various wake ages further supported this hypothesis. The effects of flow rotation on the turbulence present inside the vortex core was quantified based on a Richardson number concept. This results in a laminar flow structure until a particular distance from the vortex center that correlated with the location where the Richardson number fell below a threshold value

Based on these observations an eddy viscosity intermittency function was developed, which modeled the flow transition within the three regions of the core. This function was incorporated into a comprehensive tip vortex model formulated in terms of vortex Reynolds number. The empirical constants used in the present model were obtained from the present measurements, as well as several other sources. The dependence of the results on vortex Reynolds number ensured that the model successfully predicted the core growth of tip vortices for both sub-scale as well as full-scale rotors.

Contributions to the Measurement and Analysis of Helicopter Blade Tip Vortices

by

Manikandan Ramasamy

Dissertation submitted to the Faculty of the Graduate School of the
University of Maryland, College Park in partial fulfillment
of the requirements for the degree of
Doctor of Philosophy
2004

Advisory Committee:

Minta Martin Professor J. Gordon Leishman, Chairman/Advisor
Gessow Professor Inderjit Chopra
Associate Professor James Baeder
Professor Roberto Celi
Professor James H. Duncan

DEDICATION

To my parents

who opened up a world of possibilities to me

with their endless love and support

ACKNOWLEDGEMENTS

I would like to take this opportunity to thank all those at University of Maryland who have helped me during my doctoral research endeavor for the past 4 years. First and foremost, i would like to express my deepest gratitude towards my advisor Prof. Leishman for his patience, encouragement, guidance, and expertise without whom this work would not have come to fruition. There are no adequate words to convey my appreciation for all the support he gave in completing this gargantuan task. I would also like to thank my advisory committee Prof. Baeder, Prof. Celi, Prof. Chopra, and Prof. Duncan for their critical comments and suggestions, which continuously improved the quality of this work.

I could have never accomplished this task without the aid of my friends and colleagues at the rotorcraft center who have been an invaluable source of knowledge and are very helpful. In particular, i would like to thank Shreyas Ananthan and Karthikeyan Duraiswamy for spending numerous hours discussing my research. I would also like to thank Jaynarayanan Sitaraman, Sudharsna Koushik, and Sandeep Gupta for their help in various parts of this work. I would also like to thank Dr.Bhagwat and Dr.Martin for helping me throughout this work amidst their busy schedule.

It would, of course, be completely amiss for me without recognizing the immense contributions that my friends outside the rotorcraft center have made towards my work. Especially, Raksh Babu Bobba, Karthikeyan Chandrashekar, Mr. and Mrs. Akshay, Jita Mitra, and Ragunath Shankaranarayanan helped me enjoy the life outside my research. Many thanks goes to my friend Dr.Karumbu Meyyappan and his wife ”Aachi” for being patient and kind over the past few years. I would also like to thank Dr. Manivannan Ethirajan and his brother, my friend, Tamilmani Ethirajan

without whom i may not be here on the first place.

I would also like to thank my wife for providing a shoulder to lean and for the love, patience, and understanding – she allowed me to spend most of the time on this dissertation. I would like to thank my parents and my sister for instilling in me a determination to succeed and love of knowledge that were necessary foundations in my pursuit of this degree. The love and encouragement of my family kept me going through it all. They are constantly in my thought and their love and support has been a major stabilizing force. Their unquestioning faith in me and my abilities has helped me to make all this possible, and for that, and for everything else, I dedicate this dissertation to them.

TABLE OF CONTENTS

LIST OF TABLES viii

LIST OF FIGURES ix

LIST OF SYMBOLS xv

1 Introductory 1

1.1 Introduction 1

1.2 Tip Vortices and Rotor Wakes 3

1.3 Motivation 6

1.4 Challenges in Making Measurements in the Rotor Flow Field 17

1.5 Challenges in Modeling the Tip Vortices 22

1.6 Previous Work 24

1.7 Objectives of the Dissertation 31

2 Approach 33

2.1 Experimental Approach 33

2.1.1 Rotor Facility 34

2.1.2 Ground Plane 35
2.1.3 Flow Visualization 37
2.1.4 LDV System 39
2.1.5 Alignment Technique 41
2.1.6 Data Acquisition 44
2.1.7 Aperiodicity Correction 46
2.2 Theoretical Approach 50
2.2.1 Introduction 50
2.2.2 Structure of the Tip Vortex 60
2.2.3 Effects of Flow Rotation on Tip Vortex Development 61
2.2.4 Analogy of Rotating and Stratified Flows 63
2.2.5 Richardson Number Effects 64
2.2.6 New Vortex Model 66
2.2.7 Modeling of Eddy Viscosity 72
2.2.8 Solution Procedure 77
2.2.9 Determination of Empirical Constants 78

3 Results and Discussion **84**

3.1 Experimental Results 85
3.1.1 Wake Displacements and Strains 85
3.1.2 Velocity Field Measurements 94
3.2 Analysis of the Measurements 102
3.2.1 Treatment of Diffusion 102
3.2.2 Treatment of Strain or “Stretching” 104
3.2.3 Correction for Strain Effects 105
3.2.4 Combined Growth Model 108

3.2.5 A Model for δ 113
3.3 Generalized Transitional Vortex Model 125
3.3.1 Swirl Velocity and Circulation 126
3.3.2 Peak Swirl Velocity and Core Radius 136
3.3.3 Core Growth 136
3.3.4 Combining Filament Strain and Flow Rotation Effects 138

4 Conclusions **150**
4.1 Summary of Contributions 151
4.2 Conclusions 153
4.3 Recommendations for Further Research 156
4.3.1 Measurement Techniques 156
4.3.2 Tip Vortex Analysis 156

A Aperiodicity Correction **158**

REFERENCES **163**

LIST OF TABLES

1.1 Value of n for various rotor experiments. 24

2.1 Values of equivalent peak swirl velocity from various rotorcraft experiments. 80

LIST OF FIGURES

1.1 Photograph of tip vortices trailing the rotor blades of the Bell AH-1 Cobra. (Courtesy of the US Navy.) 2

1.2 Typical flow phenomena found on a helicopter in forward flight [27]. . 5

1.3 Schematic showing the locations of BVI on a four-bladed rotor operating in forward flight. 7

1.4 Schematic illustrating the effects of the positive straining or "stretching" of a vortex filament in a velocity gradient. 9

1.5 Schematic illustrating the effects of the viscous diffusion of a tip vortex filament. 10

1.6 Schematic showing the wake structure of a helicopter rotor. (a) In the baseline case, the rotor operates in free air. (b) In the other case, the rotor operates in the presence of ground, which stretches the vortex filaments. 13

1.7 Plot showing the difference in wake geometry of a 4-bladed helicopter rotor operating in forward flight ($C_T = 0.064 \quad \mu = 0.15$) with and without strain effects considered in the calculation [37] (a) Top view, (b) Rear view. 14

1.8 A representative flow visualization image of a tip vortex emanating from a rotor blade showing three distinct regions: (1) Laminar region, (2) Transitional region, (3) Turbulent region [38]. 16
1.9 Representative flow visualization picture of a tip vortex showing the seed "void" near the vortex center. 20
1.10 Representative measured data showing the presence of a low density of seed particles near the center of the tip vortex. 21

2.1 Schematic showing the experimental setup to stretch the tip vortex filaments using ground plane. 34
2.2 Photograph of the ground plane used for stretching the tip vortex filaments. 36
2.3 Schematic of experimental setup for flow visualization. 38
2.4 Setup of three-component LDV system. 40
2.5 Location of the transmitting beams relative to the rotor blade tip measured using beam profiler. 43
2.6 Schematic showing the LDV and vortex coordinate systems for performing coordinate transformation. 45
2.7 Standard deviation of radial and axial locations of rotor tip vortices at different wake ages. 47
2.8 Correlation of the standard deviation between radial and axial spatial locations of the rotor tip vortices at different wake ages. 48
2.9 Swirl velocity distribution for an aging vortex as predicted by the laminar Lamb–Oseen model. 52
2.10 Core radius as a function of wake age for an aging vortex as predicted by the laminar Lamb–Oseen model. 53

2.11 Determination of the value of apparent to actual viscosity ratio, δ from various experiments [101]. 55
2.12 Vortex core growth predicted by Squire's model, ($\zeta_0 = 30\,\text{deg}$) in comparison with experimental data. 56
2.13 Iversen–type correlation of peak swirl velocity with equivalent downstream distance for fixed-wing and rotor tip vortex measurements. . . 58
2.14 Swirl velocity distribution predicted by Iversen model at various vortex Reynolds numbers. 59
2.15 Variation of δ with Reynolds number based on Iversen's model. . . . 60
2.16 Swirl velocity distribution of a tip vortex using Lamb–Oseen and Iversen models compared to measurements. 62
2.17 Representative plot of Richardson number with radial coordinate for a vortex flow. 65
2.18 Eddy viscosity intermittency function across the vortex: (1) Laminar region, (2) Transitional region, (3) Turbulent region. 73
2.19 Eddy viscosity intermittency function across the vortex in terms of similarity variable: (1) Laminar region, (2) Transitional region, (3) Turbulent region. 74
2.20 Variation of peak swirl velocity versus Reynolds number for Lamb–Oseen and Iversen models. 82

3.1 Flow visualization images of a rotor blade tip vortex at (a) $\zeta = 15^\circ$, (b) $\zeta = 60^\circ$, (c) $\zeta = 90^\circ$, (d) $\zeta = 270^\circ$. 86
3.2 Results showing the axial locations of the tip vortices relative to the rotor tip-path-plane. 88

3.3 Results showing the radial locations of the tip vortices relative to the rotor tip-path-plane. 89
3.4 Estimated components of the tip vortex convection velocities compared to the baseline free-air condition. 90
3.5 Schematic explaining the procedure to calculate strain calculation from the spatial location of the tip vortices. 92
3.6 Estimated strain experienced by the vortex filaments as they approached the ground plane compared to the baseline free-air condition. 93
3.7 Swirl velocity profiles in the tip vortex at very early wake ages ($\zeta = 0^\circ$ to $\zeta = 60^\circ$). 95
3.8 Swirl velocity profiles in the tip vortex within one rotor revolution ($\zeta < 360^\circ$). 96
3.9 Swirl velocity profiles in the tip vortex at older wake ages (between $\zeta = 350^\circ$ to $\zeta = 550^\circ$), showing the vortex still diffuses under the action of viscosity. 97
3.10 Swirl velocity profiles in the tip vortex near the solid boundary ($\zeta > 700^\circ$), suggesting a strain dominated vortex flow. 98
3.11 Measured growth of the vortex core radius as a function of wake age. 100
3.12 Measured circulation as a function of wake age. 102
3.13 Trends in the core growth when correcting the measurements for the effects of filament strain. 107
3.14 Representative growth of the viscous core radius of a rectilinear vortex filament as a function of time (wake age) for uniformly imposed strain rates [37]. 111

3.15 Representative growth of the viscous core radius of a rectilinear vortex filament as a function of time (wake age) for linearly imposed strain rates [37]. 112
3.16 Predictions of core growth under the assumptions of viscous diffusion with $\delta = 8$ in a known strain field. 114
3.17 Correlation of peak swirl velocity with equivalent downstream distance for fixed-wing tip vortex measurements. 117
3.18 Correlation of peak swirl velocity with equivalent downstream distance for rotor tip vortex measurements. 118
3.19 Effective diffusion parameter, δ, as a function of vortex Reynolds number, Re_v. 120
3.20 Effective viscosity parameter, a_1, as a function of vortex Reynolds number, Re_v. 122
3.21 Measured core size of tip vortices at various wake ages - before and after correction for aperiodicity effects. 124
3.22 Swirl velocity distribution using new model for $Re_v = 48,000$, (1) Laminar region, (2) Transitional region, (3) Turbulent region. 127
3.23 Ratio of circulation to circulation ar large distance, $Re_v = 48,000$, (1) Laminar region, (2) Transitional region, (3) Turbulent region. 128
3.24 Predicted swirl velocity profiles at $Re_v = 200$. 129
3.25 Predicted swirl velocity profiles at $Re_v = 25,000$. 130
3.26 Predicted swirl velocity profiles at $Re_v = 48,000$. 130
3.27 Predicted swirl velocity profiles at $Re_v = 75,000$. 131
3.28 Predicted swirl velocity profiles at $Re_v = 1 \times 10^5$. 131
3.29 Predicted swirl velocity profiles at various vortex Reynolds numbers. . 133

3.30 Variation of Richardson number for various models with non-dimensional radial distance, $Re_v = 48,000$. 134
3.31 Variation of peak swirl velocity with vortex Reynolds number. 135
3.32 Variation of peak swirl velocity with wake age for various vortex Reynolds numbers. 137
3.33 Variation of vortex core radius with wake age for various vortex Reynolds numbers. 139
3.34 Variation of δ with vortex Reynolds number. 140
3.35 Variation of δ with vortex Reynolds number to determine a_1. 141
3.36 Effective viscosity parameter, a_1, as a function of vortex Reynolds number. 144
3.37 Core growth predicted by the new vortex model at different vortex Reynolds numbers. 146
3.38 Variation of core growth predicted by the new model for different values of uniform strain rates at $Re_v = 4.8 \times 10^4$. 147
3.39 Core growth predicted by the new model for measured values of strain rates. 148

A.1 Flow visualization image of the vortex core, showing the measurement grid and the coordinate system relative to the vortex axis. 160
A.2 Example of a swirl velocity profile before and after correcting for aperiodicity of the vortex position. 162

Nomenclature

$a,\ b$	Empirical constants
A	Rotor disk area, m^2
a_1	Squire's coefficient
AR	Aspect ratio of the rotor blade
c	Rotor blade chord, m
C_0	Constant
C_T	Rotor thrust coefficient, $T/(\rho A\Omega^2 R^2)$
$\bar{d}$	Non-dimensional downstream distance
e	Correlation coefficient
g	Core circulation function
k	Empirical constant
l	Prandtl's mixing length, m
l	Filament length, m
N_b	Number of blades
p	Probablity density function
r	Radial distance, m
r_c	Viscous core radius, m
r_0	Initial core radius, m
$\bar{r}$	Non-dimensional radial distance, r/r_c
$\bar{r}_l$	Position vector of the filament, m
r_p, z_p	LDV measurement location w.r.t. rotor axes
r_v, z_v	Vortex core location w.r.t. rotor axes
R	Rotor radius, m
Re_ν	Vortex Reynolds number, Γ_ν/ν

Ri	Richardson number
t	Time, s
T	Rotor thrust, N
VIF	Vortex intermittency function
V_1	Peak swirl velocity, m/s
$V_{1\,new}$	Peak swirl velocity in new model, m/s
V_g	Velocity of the tip vortex measured by the two green beams, m/s
V_v	Radial velocity of the tip vortex measured by two violet beams, m/s
V_b	Radial velocity of the tip vortex measured by two blue beams, m/s
V_r	Radial velocity of the tip vortex, m/s
V_z	Axial velocity of the tip vortex, m/s
V_θ	Swirl Velocity, m/s
V_∞	Free stream velocity, m/s
V_ε	Filament strain rate, m/s
z	Downstream distance, m
α	Oseen constant = 1.25643
α_I	Iversen's constant, = 0.01854
α_{new}	New empirical constant, = 0.0655
γ	Reduced circulation, = rV_θ, m^2/s
γ_v	Reduced circulation at large distances, m^2/s
$\overline{\gamma}$	Non-dimensional circulation, = γ/γ_v
Γ	Circulation, = $2\pi rV_\theta$, m^2/s
Γ_v	Tip vortex strength (circulation), m^2/s
Γ_1	Circulation at core radius, m^2/s
σ_r, σ_z	Standard deviation of vortex location in

	radial and axial directions, respectively, m
δ	Ratio of apparent to actual viscosity
ε	Filament strain
ζ	Wake (vortex) age, deg
η	Similarity variable, $= r^2/4\gamma_v t$
η_1	Similarity variable at the core radius,$= r_c^2/4\gamma_v t$
η_a	Empirical constant
$\overline{\eta}$	Scaled similarity variable, $= \eta/{\alpha_{new}}^2$
κ	Newly developed function, $= {\alpha_{new}}^2$ VIF
μ	Dynamic viscosity, kg/m s^{-1}
ν	Kinematic viscosity, $m^2 s^{-1}$
ν_t	Eddy or turbulent viscosity
ν_T	Total kinematic viscosity, $= \nu + \nu_t$
ρ	Density of the fluid, kg/m^3
σ	Shear stress, N/m^2
σ_e	Effective rotor solidity, $= N_b c/\pi R$
ψ	Azimuthal position, deg.
$\bar{\omega}$	Vorticity, $m^2 s^{-1}$
Ω	Rotor rotational speed, rad s^{-1}

Chapter 1

Introductory

1.1 Introduction

The ability to hover, combined with the capability to move forward, sideward or backwards and, above all, to take off and land vertically at any place, makes helicopters the most versatile flying machines in existence today. However, these capabilities come at a price. By default, helicopters are more aerodynamically and mechanically complex, have more limited range and payload capabilities, and cannot match the speeds of fixed-wing airplanes. Yet, the benefits of helicopters far outweigh their shortcomings and are vital to the mission of a modern military, as well as being essential for many types of civil roles.

The forces required for lifting, propelling, and controlling the helicopter comes from the rotor [1]. The action of moving large mass of air through the rotor disk as a result of the static pressure jump in the plane of the rotor results in a reaction force that produces a lifting force on the rotor. The need to have a finite length blade as well as the result of the static pressure difference between the upper and lower surfaces of the blade, constant pressure lines that are more parallel to the span of the blade away

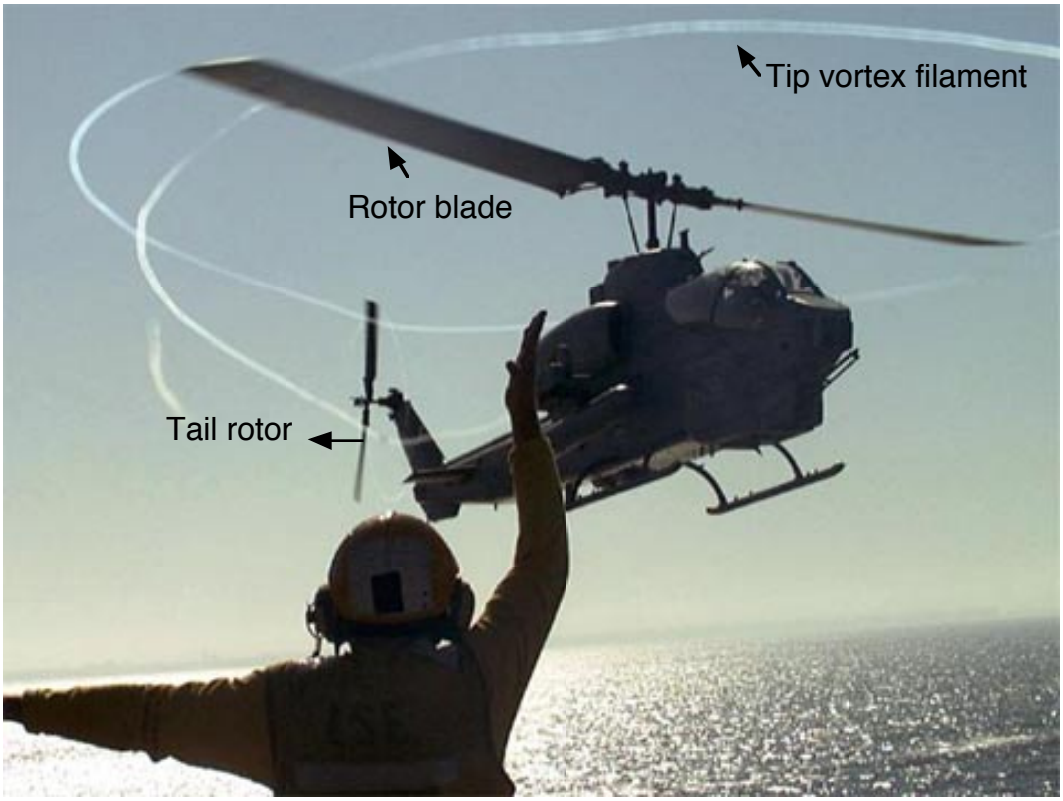

Figure 1.1: Photograph of tip vortices trailing the rotor blades of the Bell AH-1 Cobra. (Courtesy of the US Navy.)

from the tip become less parallel near the tip forming a spanwise pressure gradient [2]. On the pressure side (lower side), this pressure gradient tend to move the streamlines outward towards the tip whereas on the suction side (upper side) they tend to move the streamlines inboard from the tip [3,4]. This establishes the fundamental source of rotational flow around the tip of the blade [4] and results in the formation of strong tip vortices from each blade, as shown by the photograph in Fig. 1.1.

Understanding the characteristics of the tip vortex (trailing edge vortex in the case of fixed wings) is necessary for both fixed- and rotating-wing analyses [5–8]. The persistence of tip vortices is one of the major factors limiting the capacity of large

airports [6]. Resolving this issue requires complete understanding of the induced velocities and strength history of the tip vortices as they trail behind the aircraft [9,10]. This, in turn, depends on the understanding of various properties of tip vortices such as their turbulent, diffusive and dissipative characteristics [11, 12]. Even though, this has been the subject of much research over the past five decades [e.g., Refs. 11, 13–15], a satisfactory understanding has not yet been obtained. Also, there have been no general mathematical models developed to completely relate the properties of the trailed vortices to the aerodynamic lifting characteristics of the generating wing.

1.2 Tip Vortices and Rotor Wakes

During the past two decades, considerable research has been conducted into the problem of measuring the development of blade tip vortices trailed into the wakes of helicopter rotors [7,8,16–19]. The structure of the tip vortices defines the induced velocity field at the rotor, as well as being largely responsible for a number of adverse problems. These problems include unsteady airloads and high noise levels associated with blade vortex interactions (BVI) [8, 20–22], and significant vibration levels associated with rotor wake/airframe interactions [23–26]. The reduction of rotor noise has become an extremely important goal from both military and civil perspectives. Community acceptance (or tolerance) of helicopters will depend largely upon the successful reduction of the noise and vibration levels associated with helicopters. This, in part, requires a better understanding of the blade tip vortices and better predictions of the physics of problems such as BVI.

Determining the characteristics of tip vortices accurately is fundamental to the case of the rotating-wing when compared with the fixed-wing. This argument can be

justified using Fig. 1.2, which shows representative aerodynamic phenomena found on a helicopter in forward flight. Notice the possible interactions between the tip vortices and various helicopter components [27]. The spatial distance between the tip vortices and the blades, or between the vortices themselves, is considerably smaller, even in normal flight conditions such as hover or forward flight. As a result, a small change in the structure of the tip vortices and their positions relative to the rotor blades can have substantial effects on rotor airloads (e.g., Refs. 9,28,29) and BVI noise (e.g., Ref. 30–32). Furthermore, the rotor wake downwash on the fuselage, tail rotor and/or the empennage can lead to a further degradation in overall helicopter performance [26, 33,34]. This is not the case with fixed-wings, which trail rectilinear vortices that travel downstream away from the generating wing, and so have a decreasing influence on the wing as the vortices age.

BVI Noise and Vibration

BVI noise is a result of the interaction of a rotating blade with the tip vortex emanating from the previous blade – see Fig. 1.3. The interaction of the tip vortex changes the angle of attack on the blade locally and can result in large temporal airloads and an intense acoustic pulse [34–36]. The severity of the noise level depends upon the location of the interaction on the rotor disk, the miss distance between the blade and the vortex, and the vortex properties themselves (swirl velocity, core size etc.) [21]. The blades may also interact with vortex filaments that are relatively old in terms of rotor revolutions. During this time, the vortex filaments will have undergone some amount of viscous and turbulent diffusion, as well as encountering steep velocity gradients that can also affect their evolution [37,38]. This further complicates the aerodynamic environment at the plane of the rotor, and so results in highly unsteady airloads that

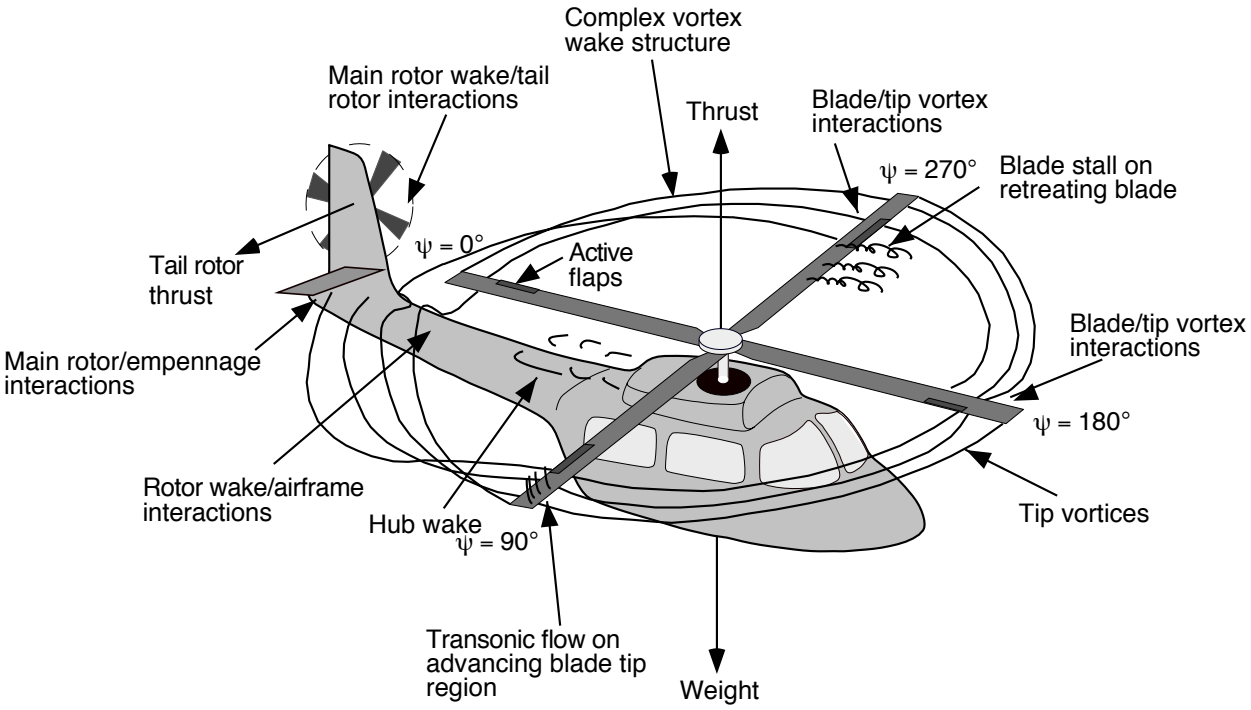

Figure 1.2: Typical flow phenomena found on a helicopter in forward flight [27].

are extremely difficult to predict.

Rotor vibration is another adverse characteristic of the helicopter that has its source in the unsteady aerodynamics of the main rotor [26, 39]. Tip vortices from several revolutions (or blades) can form a bundle and can manifest as a single merged vortex that has a strength much larger than an individual vortex filament. This results in an extensive localized region of downwash altering the angle of attack on the rotor blades [40,41]. Consequently, this reduces the lift produced near the tip at a frequency of N_b/rev. These unsteady airloads are transmitted through the hub as vertical airframe vibration [40, 41]. These excessive vibrations contribute greatly to aircrew and passenger discomfort and fatigue, and affect the maintainability, reliability, and operability of the helicopter.

Any strategy aimed at alleviating or controlling these vortex induced adverse phenomena must stem from a better understanding of the structure, strength and various characteristics of the tip vortices emanating from the tip of the rotor blades [7, 8, 10, 38, 42–44]. This, in turn, should help in developing and validating tip vortex models with higher levels of fidelity to ensure sufficient confidence in the induced airloads predictions [45–49], vibrations [50] and noise levels associated with helicopter rotors [51].

1.3 Motivation

There has been much experimental work done to measure and otherwise characterize the structures of blade tip vortices [11, 12, 16, 52–57]. Typical experimental goals include the measurement of the induced velocity field close to the vortex, the viscous "core" size, and the rate of growth of the viscous core as the vortex ages in the

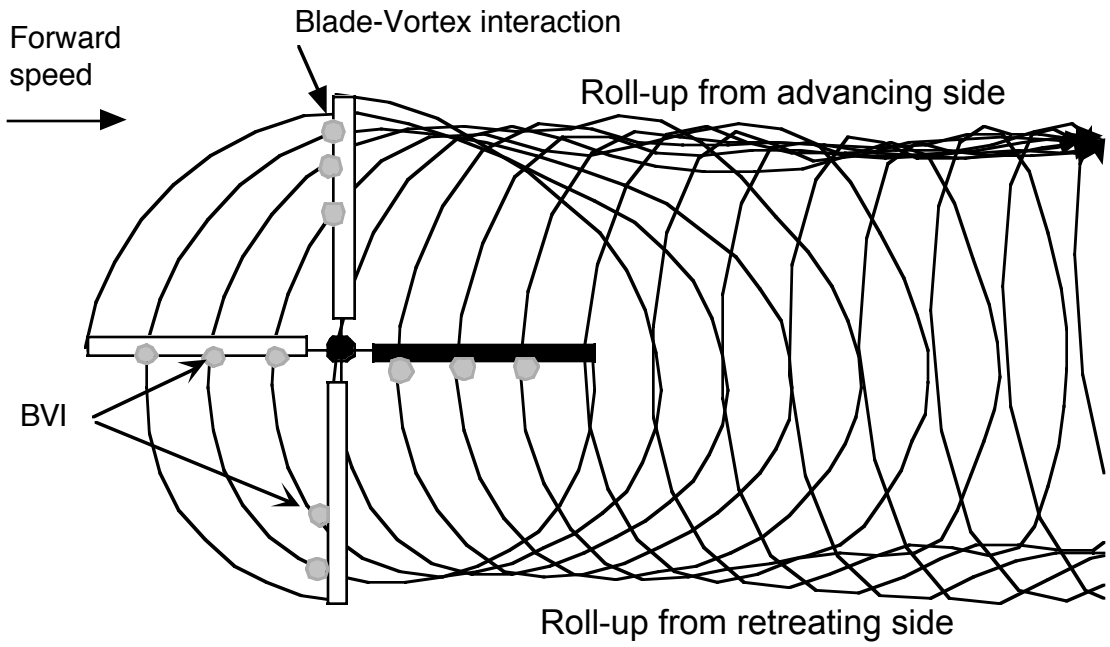

Figure 1.3: Schematic showing the locations of BVI on a four-bladed rotor operating in forward flight.

flow. However, as will be shown in this dissertation, the velocity field and viscous core size by themselves are insufficient quantities to develop comprehensive and fully satisfactory models of the tip vortices.

Most rotor wake measurements, if not all, fundamentally include the effects of stretching in the tip vortex behavior. The magnitude of this "stretching" depends on the flight conditions at which the measurements are made. Vortex filament stretching is often assumed negligible in most work and is not considered when explaining the physics of vortex flows, but its effects are combined in to the net behavior of the vortices. Ananthan et al. [37] showed that the effects of vortex filament strain on the performance of the rotor can be significant in normal flight conditions. A schematic explaining the effects of positive filament strain is shown in Fig. 1.4 as the vortex convects in the non-uniform flow. While viscous diffusion results in an increased core size and a decreased peak swirl velocity, as shown in Fig. 1.5, positive filament stretching results in a reduced core size and a concentration of vorticity. Conversely, a contraction results in an increased core size. Isolating vortex filament strain from viscous diffusion is, therefore, essential for developing better vortex models for use in helicopter rotor analyses.

The structure of tip vortices are usually modeled by making a completely laminar or turbulent flow assumption [13, 14, 58, 59]. However, flow rotation has been hypothesized to play a substantial role in determining the overall turbulence structure inside a vortex and, on the evolution of the tip vortices, in general [60–63]. Although there are measurements that have suggested a multi-region vortex structure [8, 43, 64] (i.e., laminar flow inside the vortex core, followed by a transition region and an outer turbulent flow region), there have been no general vortex models derived from the N–S equations that takes into account the effects of flow rotation in determining the

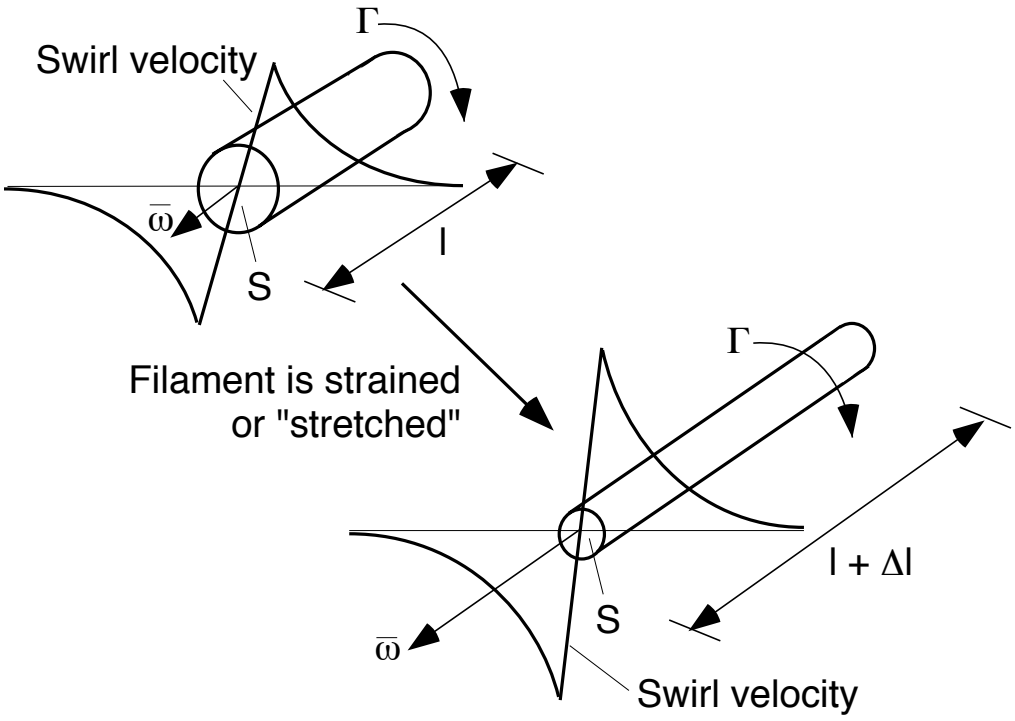

Figure 1.4: Schematic illustrating the effects of the positive straining or “stretching” of a vortex filament in a velocity gradient.

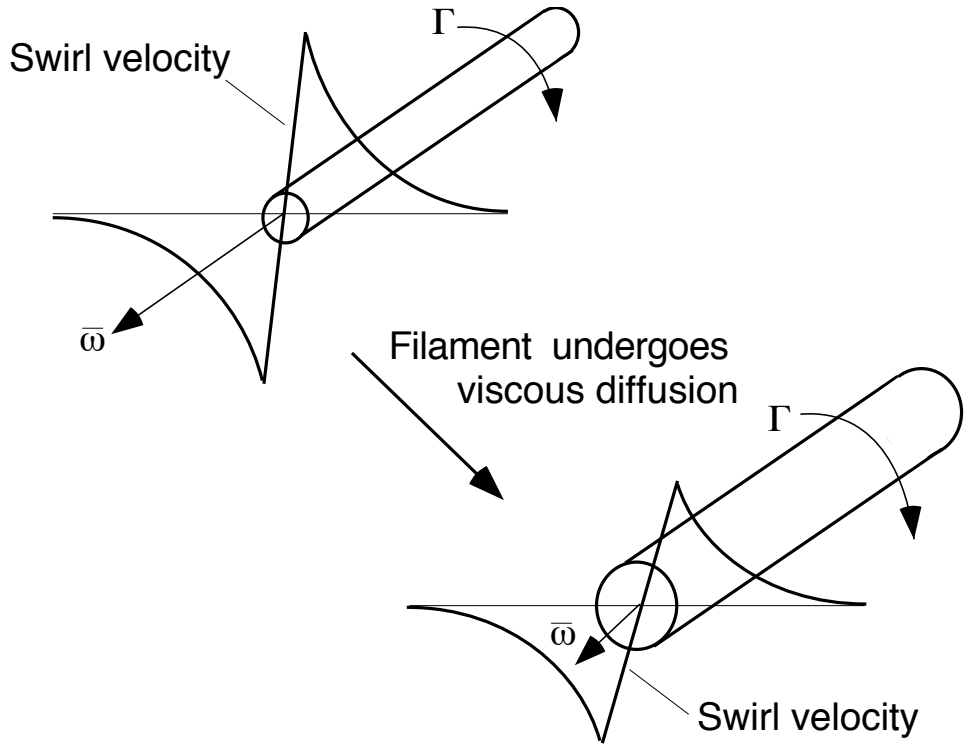

Figure 1.5: Schematic illustrating the effects of the viscous diffusion of a tip vortex filament.

turbulent structure and other characteristics of the tip vortices. In this regard, both Reynolds number and Richardson number effects must be considered [65, 66].

Besides filament stretching effects and flow rotation (Richardson number), another important but neglected issue is scaling effects [43]. The difficulty in developing an analytical model from the non-linear N–S equations, combined with the unavailability of computer resources to obtain a higher resolution numerical solution, has led to the development of semi-empirical models for the tip vortices trailing from helicopter rotor blades. The empirical constants that are used in these models are mostly estimated from sub-scale rotor or fixed-wing measurements. The ability to predict confidently the behavior of full-scale flight tests using the vortex models that are developed from sub-scale rotor measurements has not been justified. The vortex Reynolds number (Re_v), which is defined as the ratio of total circulation (Γ_v) to the viscosity (ν), (i.e., $Re_v = \Gamma_v/\nu$) for sub-scale rotor models, is smaller by orders of magnitude when compared with full-scale flight vehicles. Even though the vortex Reynolds number is known to affect various properties of the tip vortices, existing vortex models used in helicopter applications do not address such scaling issues. The only exception is Iversen's vortex model [59], which is a function of vortex Reynolds number, but it assumes a fully turbulent vortex.

Effects of Vortex Filament Strain

One significant difference affecting the evolution of tip vortices between fixed- and rotating-wings is the magnitude of the strain field exerted on the vortex filaments. In the case of fixed-wings, which trail rectilinear vortices, the velocity gradients are not large enough to have any substantial effect in many properties of the tip vortex such as its core growth, or peak swirl velocity. Yet, for a helicopter the proximity

of the vortices relative to the rotor means that filament strain may have effects on the developing characteristics of the tip vortices as they develop in the non-uniform velocity field.

A description of the vorticity in the rotor wake is governed by the three-dimensional, incompressible, Navier–Stokes equations. These can be represented in a velocity-vorticity $(\mathbf{V}\cdot\omega)$ formulation as

$$\frac{\partial\overline{\omega}}{\partial t} = -\underbrace{(\mathbf{V}\cdot\nabla)\overline{\omega}}_{\text{convection}} + \underbrace{(\overline{\omega}\cdot\nabla)\mathbf{V}}_{\text{strain}} + \underbrace{(\nu\Delta\cdot\overline{\omega})}_{\text{diffusion}} \tag{1.1}$$

This equation defines the change of vorticity of a fluid element moving with the flow in terms if the instantaneous value of vorticity, $\overline{\omega}$, and the local velocity $\mathbf{V}$. Notice that the strain or "stretching" term exists only in a three-dimensional flow. The significant complication in the solution of Eq. 1.1 arises from the velocity field $\mathbf{V}$, which is highly non-linear as a result of the self and mutually induced velocities of the entire rotor wake, as well as any external velocity.

Ananthan et al. [37] predicted the strain rate exerted on vortex filaments for many flight conditions using a free-vortex rotor wake model and the magnitude of the results suggested, in general, that the effects of strain cannot be neglected in rotor flow field analysis. Even normal flight conditions such as for a rotor operating in forward flight or in ground effect seem to produce substantial strain on the tip vortex filaments. For example, Fig. 1.6 shows the wake structure of a rotor operating in and out of ground effect. It can be observed that in the presence of ground, even though the wake contracts initially at early wake ages similar to the out of ground effect case, the tip vortices stretch radially as they approach the ground plane.

The amount of strain exerted on the tip vortex filaments for a 4-bladed rotor operating in forward flight was predicted by Ananthan et al. [37] using a free-vortex wake

(a) Baseline configuration – rotor operates in free-air

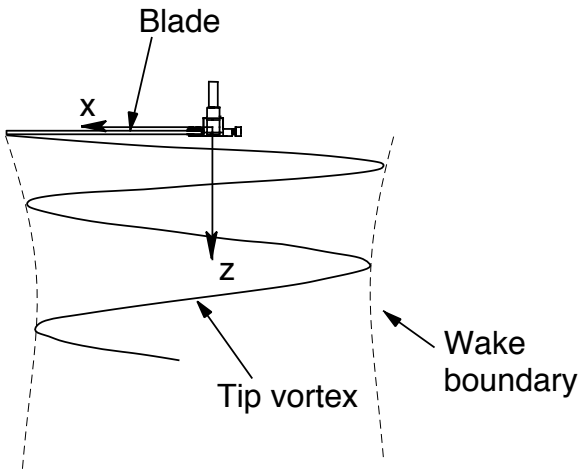

(b) Rotor operates next to ground plane

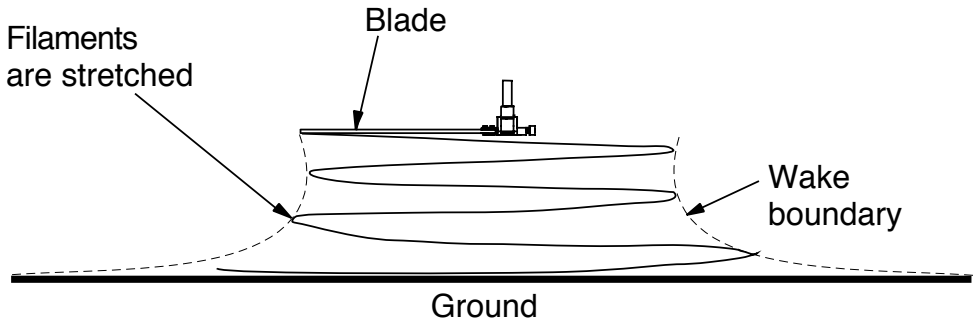

Figure 1.6: Schematic showing the wake structure of a helicopter rotor. (a) In the baseline case, the rotor operates in free air. (b) In the other case, the rotor operates in the presence of ground, which stretches the vortex filaments.

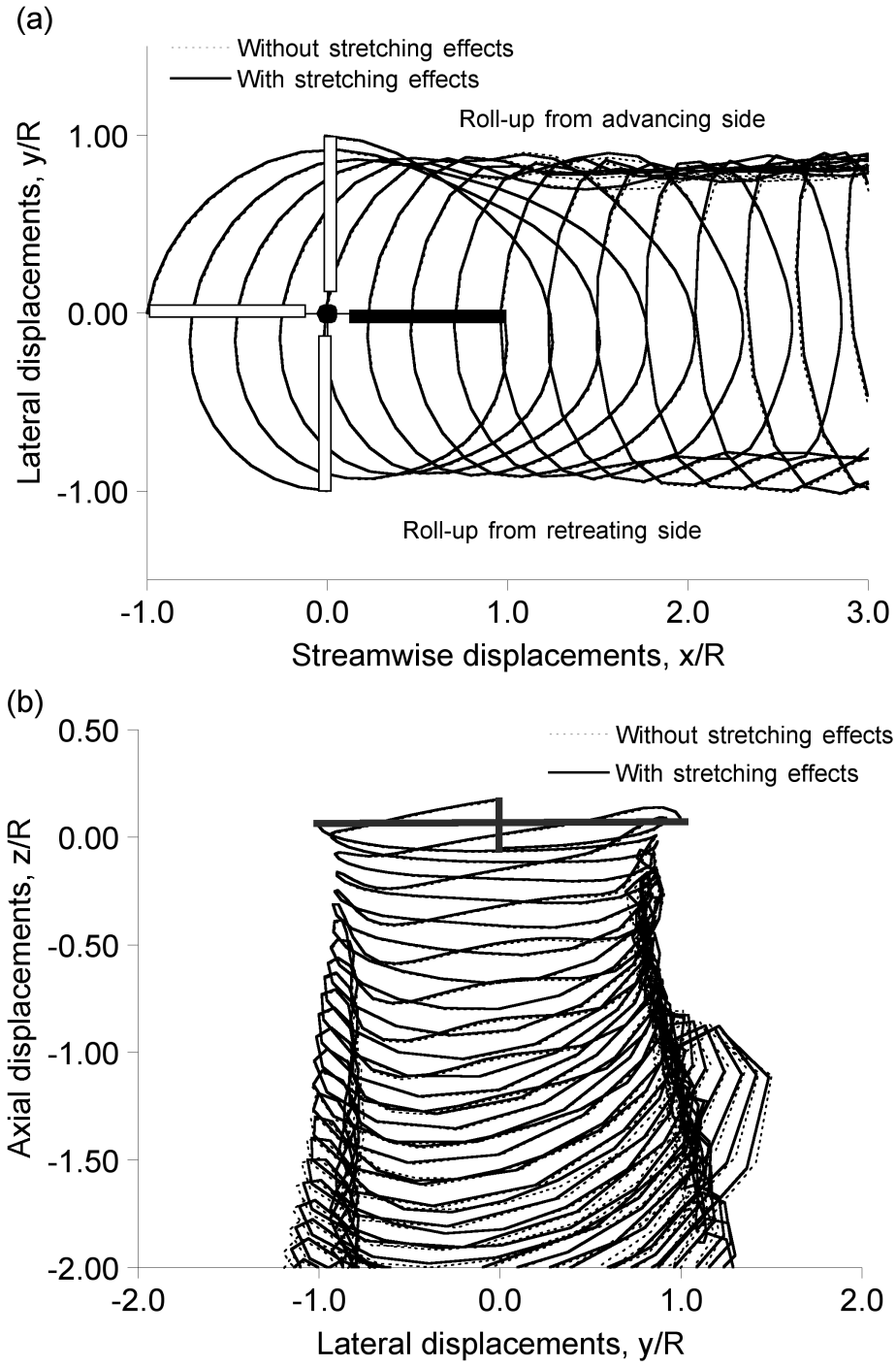

Figure 1.7: Plot showing the difference in wake geometry of a 4-bladed helicopter rotor operating in forward flight ($C_T = 0.064$ $\mu = 0.15$) with and without strain effects considered in the calculation [37] (a) Top view, (b) Rear view.

analysis. The change in wake geometry as a result of strain is shown in Fig. 1.7, along with a wake geometry where only pure diffusion is considered. Notable strain rates were even found near the rotor disk. Also, as the individual vortices bundle together, considerably large negative strain rates were produced that, in turn, resulted in a large increase in the vortex core size. This is significant enough to change the local airloads on the blades as they come close to the vortex filaments [26, 45–49].

Effects of Flow Rotation

Another assumption in the development of vortex models is the assumption of either fully laminar or fully turbulent flow inside the tip vortices. There are only few vortex models that represent a multi-region vortex structure, and even fewer of these models explain the underlying physics behind this characteristic. Flow visualization of a tip vortex emanating from the tip of a rotor blade is shown in Fig. 1.8. Notice that there exists three regions of flow. Region 1, where there is no interaction between adjacent layers of fluid, suggests a fully laminar flow. Region 2 is characterized by eddies of all sizes, indicating a transitional type of flow. It is apparent that the outer Region 3 is mostly turbulent in nature. Similar suggestions about the structure of the tip vortex has been given by Hoffman & Joubert [64] using fixed-wing measurements and by Tung et al. [43] using rotor measurements. The swirl or rotation of the flow in the vortex is hypothesized to play a role in determining the vortex structure through the effect on turbulent structures present inside the vortex [60–63]. None of the existing vortex models take into account the effects of flow rotation when determining the structure of the tip vortices, i.e., the growth rate and peak swirl velocity. These are issues that are considered in this dissertation.

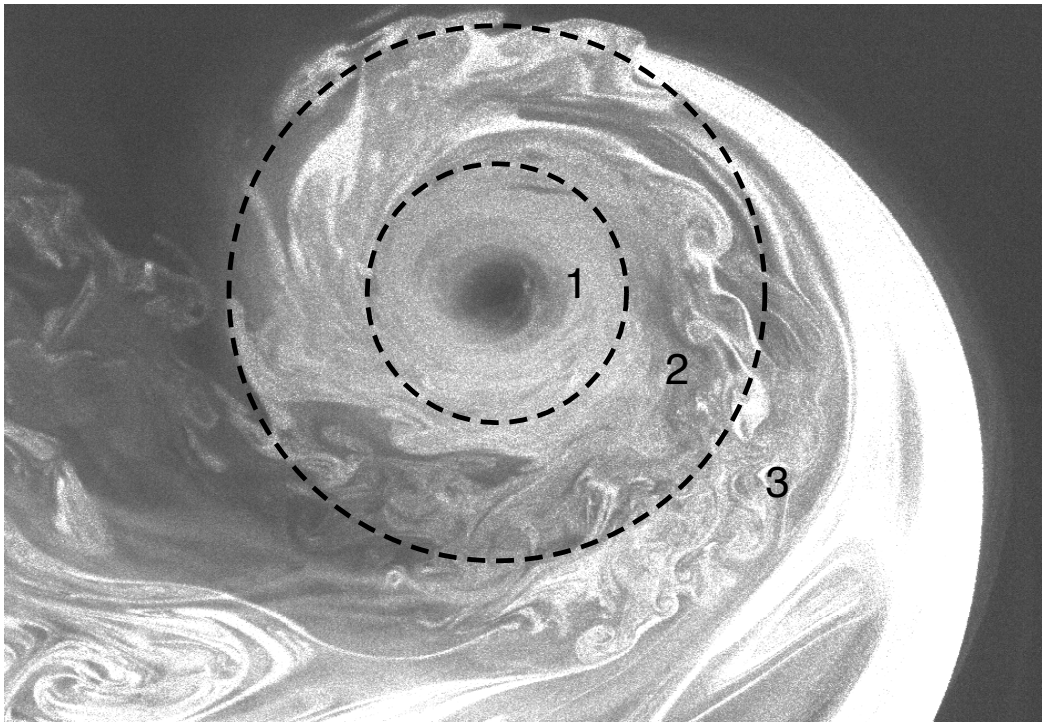

Figure 1.8: A representative flow visualization image of a tip vortex emanating from a rotor blade showing three distinct regions: (1) Laminar region, (2) Transitional region, (3) Turbulent region [38].

1.4 Challenges in Making Measurements in the Rotor Flow Field

The presence of a very complicated aerodynamic environment surrounding the rotor blades makes vortex flow measurements from rotating blades very challenging (e.g., see Ref. 27). The complexities include, but are not limited to, the persistence of tip vortices for many revolutions before diffusing or dissipating, resulting in self- and mutually-induced effects and the curved nature of the vortex filaments as opposed to the rectilinear tip vortex that trail the fixed wings. The aerodynamic environment surrounding the rotor is further complicated by the periodic nature of the vortex wake, the number and type of blade-vortex interactions, the interaction of vortex with other parts of the helicopter components, the unsteady pressure loads induced on the airframe, and the possibilities of flow separation and formation of shock on the retreating and advancing sides of the rotor disk, respectively.

The inherent difficulties in performing detailed vortex flow measurements inside rotor wakes and isolating the effects of the individual tip vortices, has forced rotorcraft analysts to augment mathematical models by using results from fixed-wing vortex flow measurements. Furthermore, measurements are not always consistent between similar rotor configurations, making it difficult to rely on some experimental data. A good summary of the numerous experiments, as well as the relative capabilities, limitations, uncertainties, and precision of the different measurement techniques is given by Martin et al. [68].

Periodicity of Rotor Wakes

Because the flow properties at a point in a rotor wake depends on the blade position, quantitative measurements of the velocity field must be phase-resolved. In most cases, this requires that the flow be periodic at the rotor frequency so that phase-averaging can be performed. However, there have been many experimental results that show the aperiodic nature of the rotor wake and the tip vortices. Aperiodicity is the inherent random movement of the phase resolved spatial location of the tip vortex cores. At a fixed measurement location (as used in LDV or PIV), aperiodicity of the flow will average out the flow properties at that location, and will appear in the measurement as a reduction in peak swirl velocity or as an increased core radius. Aperiodicity has been suggested to have its source from self-induced effects, as well as from the turbulence from the free stream flow [69]. Aperiodicity can also be a result of various vortex perturbations and instabilities [70] that appear to depend on the number of blades, rotor thrust, wake age, and operating conditions [8]. A correction scheme developed by Leishman [69] that uses the measured statistics of aperiodicity can be used to correct the swirl velocity profiles that are obtained at different wake ages. The details of this correction procedure are explained in detail in Section 2.1.8.

Flow Seeding Issues

A typical experimental procedure used to measure the various characteristics of the tip vortex involves flow visualization and velocity measurement using probes. LDV (and more recently PIV) have been used to make accurate flow measurements because of their ability to make high fidelity, non-intrusive measurements. Both flow visualization (using laser sheet) and velocity measurement using LDV/PIV require suitable distributions of smoke (or seed) particles to reflect light. Determining the optimum

location for the entrainment of smoke is a challenging problem because of the aforementioned complicated nature of the rotor wake, which results in velocities that are highly three-dimensional near the rotor. Most often, the seed will need be introduced at remote places from the region of interest. Furthermore, the size of the seeding particle is a matter of concern; the seed particles should be large enough to reflect the laser light, but small enough to accurately follow the flow.

Because of the rotating nature of the flow inside the tip vortices, the seed particles are pushed away from the center of the vortex as a result of centrifugal forces. This will result in very low density of light reflected near the center and will appear as seed void. An example is shown in Fig. 1.9. Even though this feature is helpful in determining the location of the tip vortices during laser sheet flow visualization, the absence (or presence of low density of seed particles, as shown in Fig. 1.10) near the core center will make acquiring velocity measurements using LDV or PIV more difficult.

Two non-intrusive measurement that have gained popularity in the past, as mentioned previously, are LDV and PIV. Even though PIV can make flow field measurements on a plane of interest at an instant in time (unlike LDV that makes point by point measurement), LDV is preferred over PIV for its spatial and temporal accuracy, even though it is ultimately much more tedious and time consuming. This is because of the various technical issues involved in getting the final results from PIV images, such as the determination of interrogation window size, number of interpolation vectors allowed, etc. However, some successful rotor tip vortex measurements using PIV has been reported by Heineck [71] and McAlister [7].

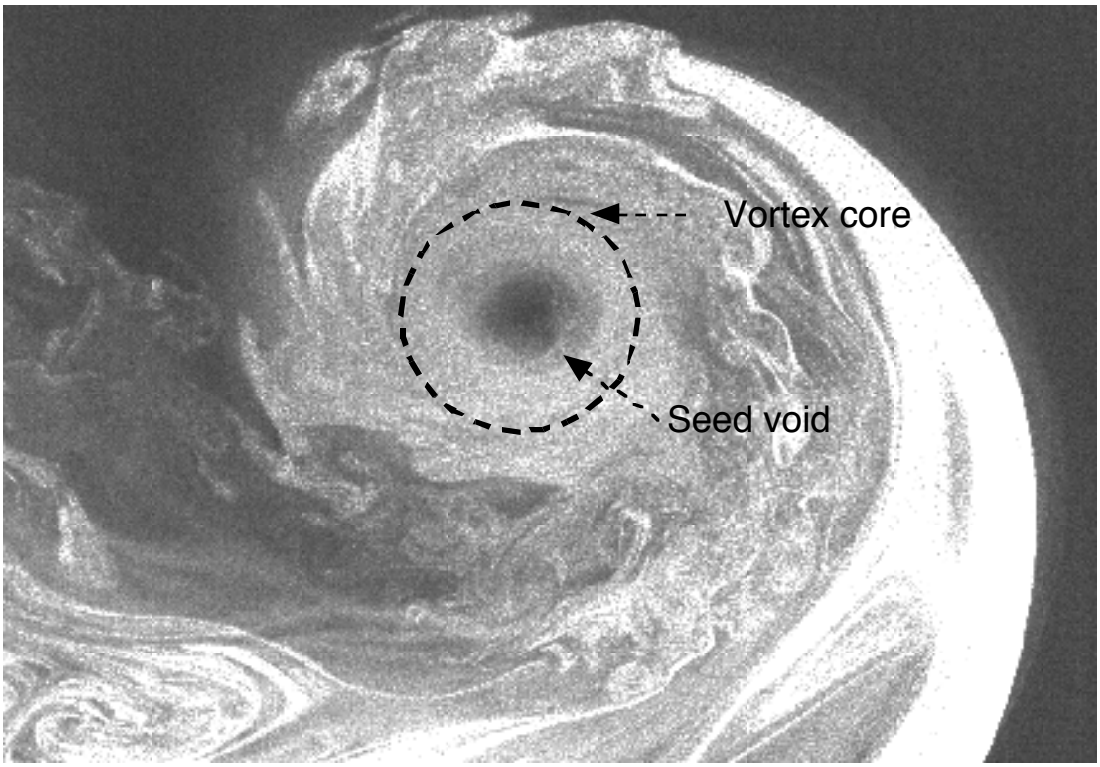

Figure 1.9: Representative flow visualization picture of a tip vortex showing the seed "void" near the vortex center.

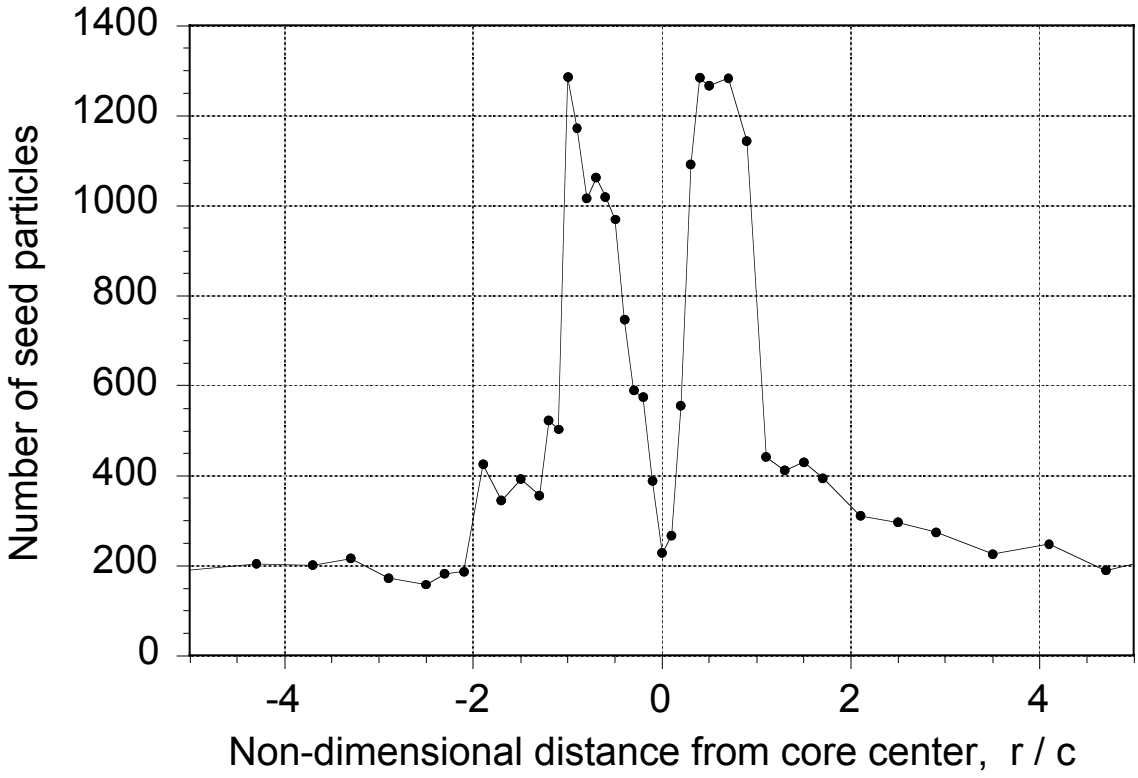

Figure 1.10: Representative measured data showing the presence of a low density of seed particles near the center of the tip vortex.

1.5 Challenges in Modeling the Tip Vortices

An exact solution to the three-dimensional Navier–Stokes (N–S) equations is required to completely describe a viscous trailing vortex. Because an exact solution to these non-linear sets of equations is not possible, most of the vortex models that exist today have been derived by making sweeping assumptions and approximations that lead to simplified solutions to the N–S equations. These assumptions include incompressible, one-dimensional flow [13,58,59], and completely laminar or turbulent flow inside the tip vortices [13,14,58,59]. Even though these assumptions result in solutions that can be applied in various applications, the vortex models that are developed based on these assumptions have been found to be inadequate to explain many essential properties of tip vortices as is shown in experiments. For example, the most frequently made one-dimensional assumption eliminates the effects of the three-dimensional induced velocity field on the development of tip vortices. This can be viewed as either a stretching or contraction of the filament, and as previously mentioned can change the induced velocity field. The effects of vortex filament stretching on the growth properties of the tip vortices were found to be substantial, as discussed earlier. From a modeling perspective (development and validation), this is a concern because of the need to to isolate stretching effects from the effects of viscous/turbulent diffusion.

Reynolds Number Scaling Issues

Despite the limitations of instrumentation in making rotor flow measurements, another concern from a modeling perspective is that the measurements must often be made on sub-scale rotors. This is a situation of necessity because of the enormous (and perhaps impractical) difficulties in making measurements with the necessary fidelity on full-

scale rotors. Furthermore, the costs and time involved in conducting experiments on full-scale rotors is enormous. However, amongst other issues, this raises questions about flow scaling effects, which at model scale may have vortex Reynolds numbers that may be up to two orders of magnitude less than those associated with full-scale rotors.

Several mathematical models of vortex flows have been proposed [10, 13, 14, 42, 43,58,59,63,64]. The most popular among the proposed models are the Lamb–Oseen model [58], which is fully laminar and the Squire [13] and Iverson models [59], which are both fully turbulent. However, most rotating-wings operate at conditions where the vortex Reynolds numbers are in the intermediate (transitional) regime, when the flow is neither fully laminar nor turbulent. This is especially true with sub-scale rotors, which generate tip vortices with much lower vortex Reynolds numbers.

A comparison of the vortex Reynolds numbers between full-scale and sub-scale rotors will throw some light in the scaling issues involved. The circulation in the tip vortex, Γ_v, is given approximately [1] by

$$\Gamma_v = k\,\Omega\,R\,c\left(\frac{C_T}{\sigma}\right) \tag{1.2}$$

where $k = 2$ in hover. This implies that the vortex Reynolds number, Re_v, is given by

$$Re_{\mathrm{v}} = \frac{\Gamma_v}{\nu} = \frac{2\,(\Omega R)\,c}{\nu}\left(\frac{C_T}{\sigma}\right) \tag{1.3}$$

Most vortex flow measurements are performed using sub-scale rotors that aerodynamically match (C_T/σ) and geometrically the blade aspect ratio, AR $(= R/c)$, of the full-scale rotors. The above expression in terms of aspect ratio AR can be written as

$$Re_{\mathrm{v}} = \frac{2\,(\Omega R)\,R}{\nu\,AR}\left(\frac{C_T}{\sigma}\right) \tag{1.4}$$

The ratio of the vortex Reynolds number between model-scale and full-scale is then

given by

$$\frac{Re_{\text{v Model-scale}}}{Re_{\text{v Full-scale}}} = \frac{(\Omega R)\, R\,|_{\text{Model-scale}}}{(\Omega R)\, R\,|_{\text{Full-scale}}} \approx \frac{1}{n} \tag{1.5}$$

The value of n varies with the scaling of the model rotor and the ratio of the tip speed between the model-scale and full-scale rotors. The value of n for some experiments

Experiments	$\Omega\, R$ Ratio	Scale	n	Re_{v}
UH-60 Black Hawk	1	1	1	$\approx 1 \times 10^6$
HART II Test [44]	1	1/2.5	2.5	$\approx 2.5 \times 10^5$
McAlister, 1996, 2003 [7, 19]	1/3	1/7	21	$\approx 1 \times 10^5$
Ramasamy & Leishman, 2003 [38]	1/3	1/15	45	$\approx 4.8 \times 10^4$

Table 1.1: Value of n for various rotor experiments.

are given in Table 1.1. Clearly these results raise issues about scaling effects because the vortex Reynolds number is already well known to affect both the structure and the diffusive growth rate of the tip vortices (e.g., Refs. 13, 59, 67). This dependency is, however, yet to be quantified precisely because of the dearth of high fidelity rotor vortex measurements over a sufficiently wide range of Reynolds numbers. It is clear that vortex models derived from model-scale experiments cannot necessarily be expected to give valid results when applied to full-scale rotors at full-scale flight conditions.

1.6 Previous Work

Numerous experiments have been performed in the past few decades in an effort to understand various characteristics of tip vortices and the complicated wake structure. The difficulty in making measurements in the rotor flow field, as mentioned earlier,

has resulted in rotor analysts using measurements from fixed-wings to develop vortex model for use in rotor analyses. Even though these measurements do not address filament strain effects, several valuable fixed-wing measurements are available and much can be learned about the basic properties of the tip vortices from these measurements alone. The current work builds on the measurements reported by Leishman and coworkers [24,26,67,69,72–79] to understand various characteristics of the tip vortices, ultimately with the goal of developing strategies to alleviate adverse vortex induced phenomena.

Full-Scale Flight Measurements

Among the very few full-scale tests with rotors and fixed-wings that have been performed in the past, the measurements made by Cook [16], Kraft [52], Boatwright [80] and Sarpkaya [6] are prominent. Cook [16] made measurements of the wake of a Sikorsky S-58 blade on a hover test stand using a one-dimensional hot wire probe. The location of the tip vortices were determined using flow visualization. The peak swirl velocity was found to range from 20% to 50% of the blade tip speed, which is in general agreement with most other measurements [7, 8, 19, 38, 81]. Cook also proposed a completely empirical vortex model from the measurements. It should be noted that Cooks's model, even though it accurately follows the measurements, does not explain any flow physics.

Kraft [52] has made measurements using two airplanes: one to create vortices and the other to make measurements on the vortices. The jet airplane that was used to create vortices was equipped with a smoke generating device to mark the vortices in the atmosphere. A tank containing titanium tetrachloride , which was pressurized with dry nitrogen was located in each wing. The resulting smoke was released at the wing

tips. The instrumentation airplane was equipped with pressure vanes at the nose. Both flow visualization and velocity measurements were made, and the results suggested that the strength of the tip vortices did not decrease even up to 35 seconds after the vortices had been trailed. Their strength then gradually reduced until 60 seconds was reached, but a large amount of circulation remained even then. This suggests the relatively long time scales associated with vortex diffusion.

Boatwright [80] performed measurements in the wake of a 2-bladed OH-23B full-scale rotor in hover using a 3-D hot film anemometer. The initial core radius was found to be 2–3 % of the effective blade chord. The peak swirl velocity was found to be 20% to 50% of the tip speed. Sarpkaya [6] made measurements on a variety of airplanes such as the DC-10, B-757, DC-10-30, etc. The effect of molecular diffusion alone on the downwash and the demise of trailing vortices were reported to be inconsistent with the high Reynolds number flow field data. The tangential velocity profile had a change in slope near the center of the vortex, suggesting the vortex core was not a benign solid body in rotation. A similar result was suggested later by McAlister [7] from a sub-scale rotor experiment. An intermittent exchange of mass, momentum and vorticity across the vortex core boundary was found. Many mechanisms have since been suggested to diffuse the tip vortices faster by increasing this exchange, which can be achieved by mutual straining, rotational damping and restructuring of turbulence, atmospheric turbulence, stratification effects, wind shear and ground effects [6].

One common observation made in all of these measurements was that the peak swirl velocity decreased and the core radius increased with time, clearly indicating diffusion effects. The effect of vortex filament strain would be negligible in all the afore mentioned cases because the measurements were either made on a hover stand or using a fixed-wing. In both cases the stretching of tip vortex filaments is considerably

smaller than would be found in general.

Sub-Scale Measurements

Making measurements on a sub-scale model is not a situation of convenience, but of necessity. The cost involved in making full scale measurements, and the need for accurate, high fidelity measurements has led to the use of sub-scale models for making measurements, despite the scaling issues associated with using these data for developing models of tip vortices.

Fixed-Wing Measurements

Chigier et al. [82, 83] conducted a test in a wind tunnel on a Convair 990 airplane model. An increase in core size associated with a decrease in the peak swirl velocity for increasing downstream distance was noticed. Cliffone & Orloff [9] and Corsiglia et al. [55] made measurements in a large-scale 40 $\times$ 80 ft wind tunnel on a B-747 model. Underwater towing tank measurements were also made. It was concluded from both the wind tunnel and the water tow facility flow visualization studies that there were two distinct downstream regions in the development of tip vortices. The first region was associated with little, if any, change in the peak swirl velocity. The second region was where the peak swirl velocity reduced at a rate nominally proportional to inverse of one half power of time. This is exactly similar to the results predicted by Iversen [59] in his measurements, calling the first region a "plateau" region and the second one "downstream decay" region.

Devenport et al. [81] made an extensive series of measurements on a fixed wing trailing vortices using a NACA 0012 half-wing and hot-wire probes. Preliminary studies showed the vortex to be insensitive to the introduction of hot wire probes and

subject to only small wandering motions. Detailed analysis of the effects of wandering was performed to properly reveal the flow structure in the core region. A theory was developed to correct the mean velocity profiles for the effects of wandering. Velocity profiles measured through the vortex center showed little change in the vortex core parameters as the flow developed. The shapes of the velocity profiles were found to be different, and the core growth was found to be inconsistent with laminar diffusion. Some velocity profiles, especially those measured at upstream locations, showed evidence of two layered structure. This consisted of an outer core that is a remnant of a secondary vortex formed during the roll up process, and an inner core that grows within it with increasing downstream distance.

Dosanjh et al. [11] made vortex measurements from a rectangular, symmetrical, half wing (NACA 0009) in a low speed wind tunnel at a chord Reynolds number of 10,000. The total pressure and flow directions were measured with a five-hole pressure probe at one to eight chord lengths behind the trailing edge of the wing. Radial, axial and tangential velocities were derived from these measurements. The viscous vortex model derived by Newman [84] was found to correlate well with the experimental measurements. The viscous core radius was found to increase, along with a reduction in peak swirl velocity with increasing time. The core was found to grow at a rate that was 8 to 10 times faster than predicted by the analysis when using a value of kinematic viscosity, such as used in the Lamb–Oseen model. The total vortex circulation was found to be 58% of the bound circulation.

Lezius [85] observed that the vortices grow at a rate much faster than the constant viscosity vortex models, and suggest the vortex decay is at the rate of the inverse of one-half power of time (i.e., as $r_c \sim t^{-1/2}$). An underwater towing tank experiment was constructed with a rectangular wing with an aspect ratio of 5.3 at two an-

gles of attack. The chord Reynolds numbers were 220,000 and 750,000 respectively. Tangential velocity measurements were made between 100 and 1000 chord lengths downstream. The results indicated that the core growth varied with $-7/8$ of time, i.e., $r_c \sim t^{-7/8}$. An imbalance between the initial turbulence levels and those that can be maintained by the vortex motion causes the vortex to decay in non-equilibrium conditions. This non-equilibrium decay is suggested as the reason for the differences in the decay rates of the tip vortices.

Other notable experiments that have been performed to understand the characteristics of tip vortices include Hoffman & Joubert [64], Iversen & Corsiglia [29], Landgrebe [28], Baker et al. [56] and Govindraju & Saffman [12]. Hoffman & Joubert performed an experiment on a fixed-wing vortex using a hot wire anemometer, and developed a tip vortex model based on an analogy with boundary layer theory. The measurements indicated a multi-region vortex: 1. An inner region called "eye" of the vortex which was laminar, where the tangential inertia is very high as a result of the steep tangential velocity gradient than the Reynolds stresses, 2. A region where the circulation varies logarithmically with the non dimensional radial distance, and 3. A region that is turbulent in nature. Another notable result reported was the independence of viscosity under certain conditions in the growth rate of the trailing vortices.

Rotating-Wing Measurements

Flow measurements were made by Caradonna & Tung [86] on a 2-bladed rotor operating in hover. Tip vortex measurements were made simultaneously along with blade load and performance measurements. The results showed a self-similar, multi-region tip vortex structure. The peak swirl velocity ranged between 40% and 60% of the

blade tip speed, and decreased with increasing time. The initial core radius was measured to be 4% of the blade chord. A multi-region vortex model was proposed from the measurements based on an analogy with boundary layer theory. A similar observation was made by Hoffman & Joubert [64], where measurements were made on fixed-wings.

Tangler et al. [87–90] made measurements on a sub-scale rotor model operating in hover using hot wire anemometry, strobed schlieren technique for flow visualization, and microphone measurements for rotor noise levels. Again, the results showed that the peak swirl velocity in the tip vortices were of the order of 20% to 50% of the blade tip speed, and these were found to decrease with time. Also, the peak swirl velocity was found to increase with an increase in collective pitch of the blades indicating an increase in tip vortex strength for an increase in rotor thrust.

McAlister et al. [20] performed an experiment to understand the characteristics of tip vortices and to alleviate the adverse effects by forcefully diffusing the trailing vorticity with the help of a turbulence generator. The measurements were made using stereoscopic particle image velocimetry (PIV) technique on a hovering one-seventh scale model rotor. One of the interesting results was the idea of multiple centers for the tip vortex. McAlister suggested that the center of vorticity, the center of seed void, the center of tangential velocity profile and the center of peak to peak swirl velocity are all different. The peak value of vorticity generally occurred close to the center of swirl. The presence of turbulence generator, even though increased the rotor power required by about 15%, reduced the peak swirl velocity by 57% and the core size increased to about double its initial size after one revolution. The overall behavior of the tip vortex suggest a reduction in peak swirl velocity and an increase in the core radius for increasing wake age.

1.7 Objectives of the Dissertation

It is apparent from the foregoing discussion that even though there have been numerous experiments performed in the past to determine various characteristics of the tip vortices, no attempt has been made to quantify the effects of vortex filament stretching on the evolution of the tip vortices. Vortex strain induced by stretching may have substantial effects on the vortex core properties in many rotor flight conditions. All the vortex models that exist today have been developed assuming pure diffusion, and neglecting the effects of vortex filament strain. Also, the effects of flow rotation and the effects of vortex Reynolds number were not taken into account when developing a tip vortex model for rotor analysis, despite the substantial role of Reynolds number in determining the structure and, therefore, the evolution of the tip vortices.

The objective of the present study is two fold. First, to perform an idealized experiment in an attempt to measure any interdependence of straining and viscous/turbulent diffusion on the development of helicopter rotor tip vortices. The measurements were primarily made using a three-component LDV, which was complemented by detailed flow visualization of the rotor wake structure and the vortex cores. A single bladed rotor configuration was chosen to keep the operating configuration and the flow field relatively simple, which helps to dissect the problem in some detail while still preserving the essential physics of the problem. Vortex properties were compared to the results for the case when the rotor wake was advected toward a solid boundary. The presence of this solid boundary forced the tip vortices to stretch in a known (estimated) strain field, allowing the effects of strain to be measured and isolated. The results of this experiment will help in validating a proposed combined viscous diffusion/strain model of a tip vortex for numerical applications that, in turn, will help in improved prediction of rotor airloads, vibration and noise.

The second objective of the present work was to consider the effects of flow rotation on the structure of the tip vortex and, thereby, to develop a generalized mathematical model for rotor tip vortices that is consistent with both flow visualization and flow measurements. The first approach towards developing such a model for fully turbulent flow (using an analogy with boundary layer theory) was made by Hoffman & Joubert [64]. Iversen [59] later developed a mathematical model for turbulent tip vortices that were a function of vortex Reynolds number. The present work combines and extends both these concepts to the modeling of more general transitional vortices and provides more generalized model to predict the vortex flow at any vortex Reynolds number. The new analytical model was developed using an eddy viscosity intermittency function in such a way that this function smoothly and continuously models the eddy viscosity across the vortex from its inner rotational region to the outer potential flow region. This intermittency function is developed based on Richardson number concept, which brings in the effects of flow rotation on turbulence present inside the vortex boundaries. This function is incorporated into the N–S equations governing the development of an axisymmetric vortex flow.

The model is developed in such a way that the final solution is dependent on the vortex Reynolds number, thereby enabling rotor analysts to compare measurements that are made at different vortex Reynolds number using different scaled models. The final objective is to develop a more comprehensive vortex model, albeit still approximate, that includes vortex filament stretching effects, flow rotation effects, and vortex Reynolds number effects.

Chapter 2

Approach

2.1 Experimental Approach

As described in Chapter 1, blade tip vortices generally experience strain effects as they are convected in the velocity gradients produced inside the rotor wake. This means that filaments must undergo continuous changes in their vorticity field, even in the absence of ongoing viscous and turbulent diffusion [93]. Ananthan et al. [37] showed that filament stretching may have significant effects on the local velocity field induced by the tip vortices, which in turn, will have an effect on the development of the overall wake as adjacent vortex filaments move relative to each other. This can be a particular modeling issue in many rotor flight conditions, such as in forward flight, where individual vortices tend to bundle and roll up together from the lateral edges of the rotor disk. In general, straining effects can make the measured vortex properties different to those that might be obtained with equivalent rectilinear vortices that develop in a uniform flow. Therefore, isolating any contributing effects is essential for the development of better vortex models for helicopter rotor applications.

One of the primary objectives of the present research was to quantify the effects of

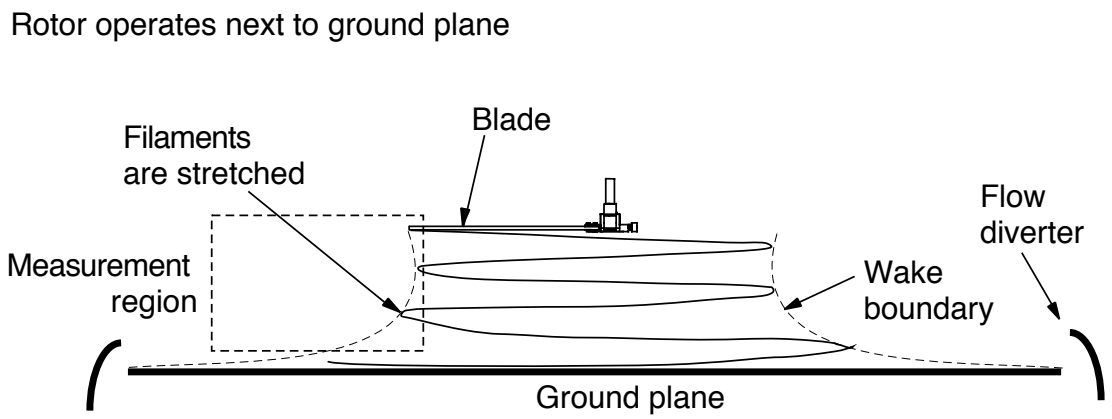

Figure 2.1: Schematic showing the experimental setup to stretch the tip vortex filaments using ground plane.

vortex filament strain on the evolution of tip vortices. To this end, an experiment was performed to make vortex induced flow measurements in a known strain field. The schematic of the experimental set up is shown in Fig. 2.1. The properties of the blade tip vortices were measured in the wake of a hovering rotor, and were compared to the results for the case when the wake was convected near to a solid boundary. The presence of the boundary forced the tip vortices to "stretch" in a known (measured) strain field, allowing the effects of this process on the tip vortex development to be measured and, to some extent, isolated. This allowed an examination of interdependent effects of straining and diffusion on tip vortex development.

2.1.1 Rotor Facility

A single bladed rotor operated in the hovering state was used for the measurements. The advantages of using a single bladed rotor have been addressed before [74, 94].

This includes the ability to create and study a helicoidal vortex filament without interference from other vortices generated by other blades [94]. Also, a single helicoidal vortex is much more spatially and temporally stable than multiple interdigitated vortices [74], thereby allowing the vortex structure to be studied to much older wake ages and relatively free of the high aperiodicity issues that are common with multi-bladed rotor experiments.

The blade was of rectangular planform, untwisted, with a radius of 406 mm (16 inches) and chord of 44.5 mm (1.752 inches), and was balanced with a counterweight. The blade was constructed from balsa wood and spruce wood cores covered with a thin layer of epoxy. The blade airfoil section was the NACA 2415 throughout. The rotor tip speed in the test was 89.28 m/s (292.91 ft/s), giving a tip Mach number and chord Reynolds number of 0.26 and 272,000, respectively. The zero-lift angle of the NACA 2415 airfoil is approximately -2° at this tip Reynolds number. All the tests were made at an effective blade loading of $C_T/\sigma \approx 0.064$ using a collective pitch of 4.5° (measured from the chord line). During these tests, the rotor rotational frequency was set to 35 Hz ($\Omega = 70\pi$ rad/s).

The rotor was tested in the hovering state in a specially designed flow conditioned test cell. The volume of the test cell was approximately 362 m^3 (12,800 ft^3) and was surrounded by honeycomb flow conditioning screens. This cell was located inside a large 14,000 m^3 (500,000 ft^3) high-bay laboratory. In the baseline case, the wake was allowed to exhaust approximately 18 rotor radii before encountering flow diverters.

2.1.2 Ground Plane

To examine the effects of superimposed velocity gradients on the tip vortex developments, an artificial means of doing this was developed using a solid boundary or

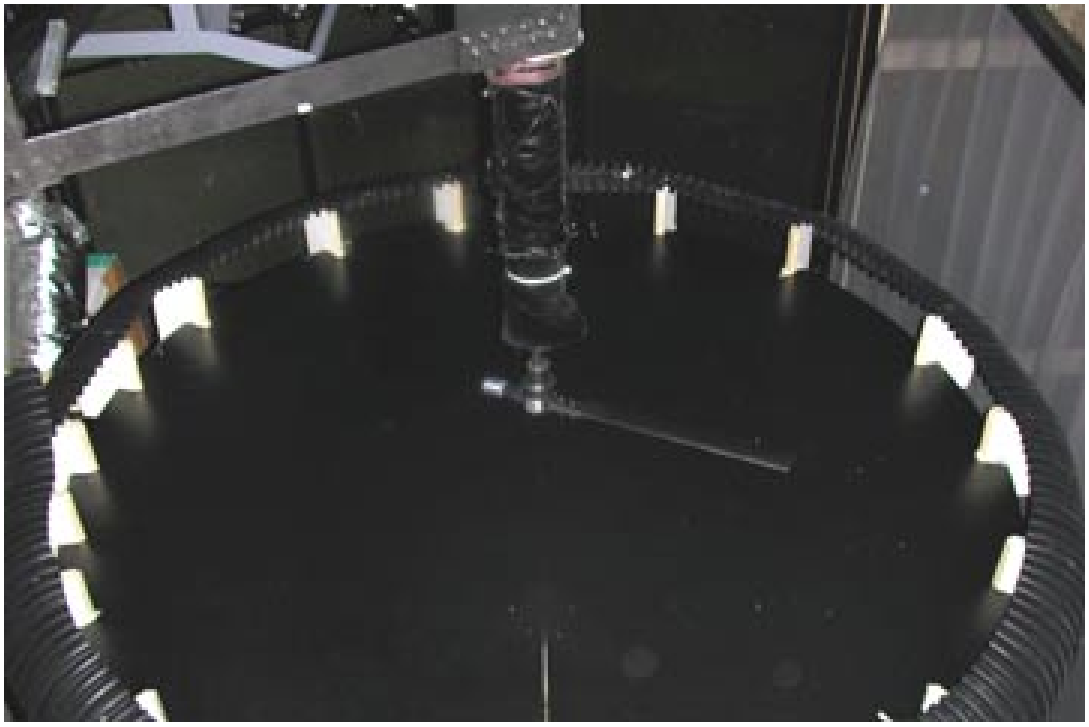

Figure 2.2: Photograph of the ground plane used for stretching the tip vortex filaments.

"ground" plane. Based on the ground effect experiments of Light & Norman [95], calculations showed that significant strain rates could be expected well before the vortex filaments reached the ground. A sketch of the ground plane is shown in Fig. 2.2, which was twice the diameter of the rotor diameter. The ground plane could be adjusted to give different distances between the rotor plane, although for the present tests it was set to $0.5R$. As the rotor wake approached this ground plane, the vortex filaments were strained rapidly in the radial direction.

The possibilities of aperiodicity and recirculation of the rotor wake was reduced by the use of a flow diverter placed along the circumference of the ground plane. This directed the incident flow away from and behind the ground plane. A further

series of flow diverters behind the ground plane was used to control the flow quality (reducing flow circulation and aperiodicity), which was verified using flow visualization. The inherent difficulties in measuring vortex velocities close to surfaces, and also in measuring the velocity profiles of tip vortices at older wake ages, however, imposed restrictions on how close the ground plane could actually be placed to the rotor. Measurements were made at up to $0.05R$ from the ground plane.

2.1.3 Flow Visualization

Flow visualization images were acquired by seeding the flow using a mineral oil fog illuminated by a laser light source. A light sheet was produced by a dual Nd:YAG laser, which generated a light pulse on the order of nanoseconds in duration at a frequency of up to 15 Hz. The light sheet was located in the flow using an optical arm. At the end of the light-arm, a cylindrical lens formed the light-sheet, and a spherical lens focused the light sheet into a thin line measuring less than 1 mm at its waist. Because the maximum frequency at which the laser could strobe was 15 Hz while the rotor was rotating at 35 Hz, the laser and the camera were synchronized using customized electronics, which converted the rotor one-per-rev frequency into a TTL signal that pulsed every third rotor revolution. A phase delay was also introduced so that the laser could be fired at any rotor blade phase angle. Strobing was necessary because the light sheet was located in the non–rotating hub frame of reference. The experimental set up for flow visualization is shown in Fig. 2.3

Judicious flow seeding was essential for producing a good flow visualization of the tip vortex. The seed was produced by vaporizing oil into a dense fog of which 95% of the particles were between 0.2 μm and 0.22 μm in diameter. This average seed particle size was small enough to minimize particle tracking errors for the vortex

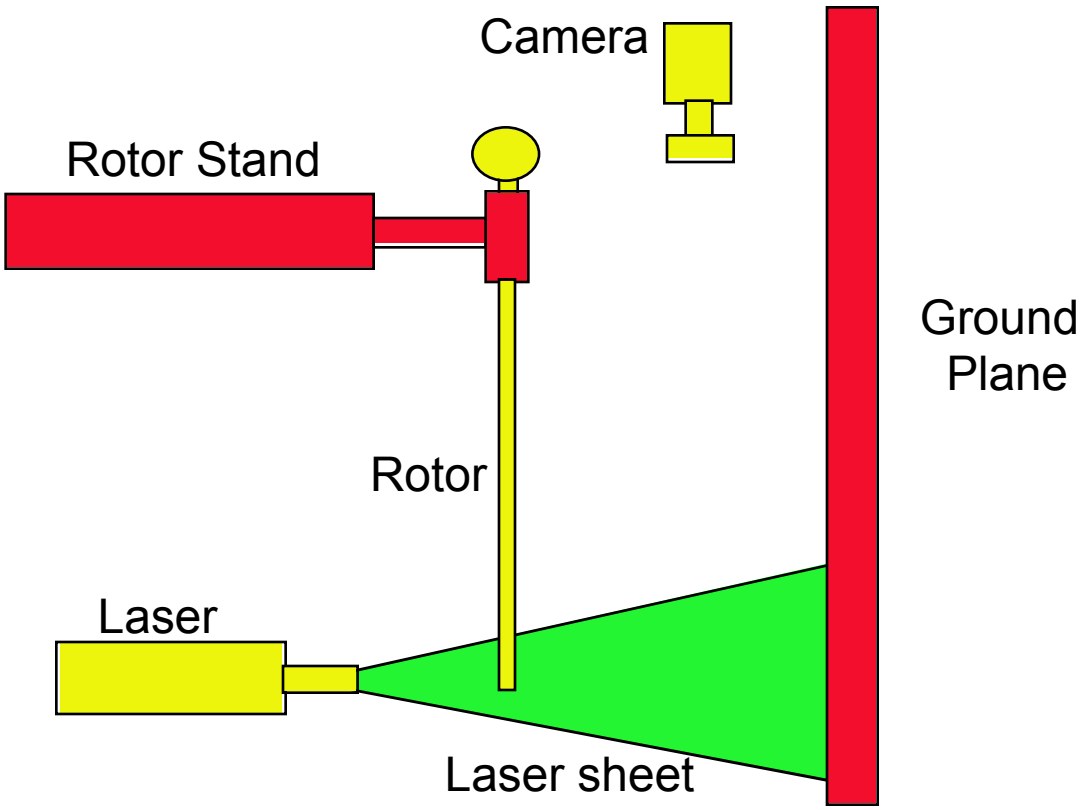

Figure 2.3: Schematic of experimental setup for flow visualization.

strengths found in these experiments [96]. The fog/air mixture was passed through a series of ducts and introduced into the rotor flow field at various strategic locations. Care was taken to prevent any addition of wake turbulence from seeding by directing the fog/air mixture away from the flow field.

The combination of low density particles associated with uniform seeding and the forward light scattering associated with the Mie pattern resulted in low levels of light at perpendicular angles to the light sheet. To capture sufficient scattered light, the camera was set at its maximum aperture size and placed at a large angle to the illuminated plane. A low wavelength band-pass optic filter (which allows light of a particular wavelength to pass through) was used to block light from other sources, which improved the quality of the picture. Images were also acquired using a CCD camera (which can produce good quality images from a low light source), and were later digitized using a calibration grid. This enabled the reconstruction of the three-dimensional spatial and temporal locations of the tip vortices in rotor wake.

2.1.4 LDV System

A fiber-optic based LDV system was used to make three-component velocity measurements. A beam splitter separated a single 6 Watt multi-line argon-ion laser beam into three pairs of beams (green, blue and violet), each of which measured a single component of velocity. A Bragg cell, set to a frequency shift of 40 MHz, produced the second shifted beam of each beam pair. The laser beams were passed to the transmitting optics by a set of fiber-optic couplers with single mode polarization preserving fiber optic cables. The transmitting optics were located adjacent to the rotor (see Fig. 2.4) and consisted of a pair of fiber optic probes with integral receiving optics, one probe for the green and blue pairs, and the other probe for the violet pair. Beam

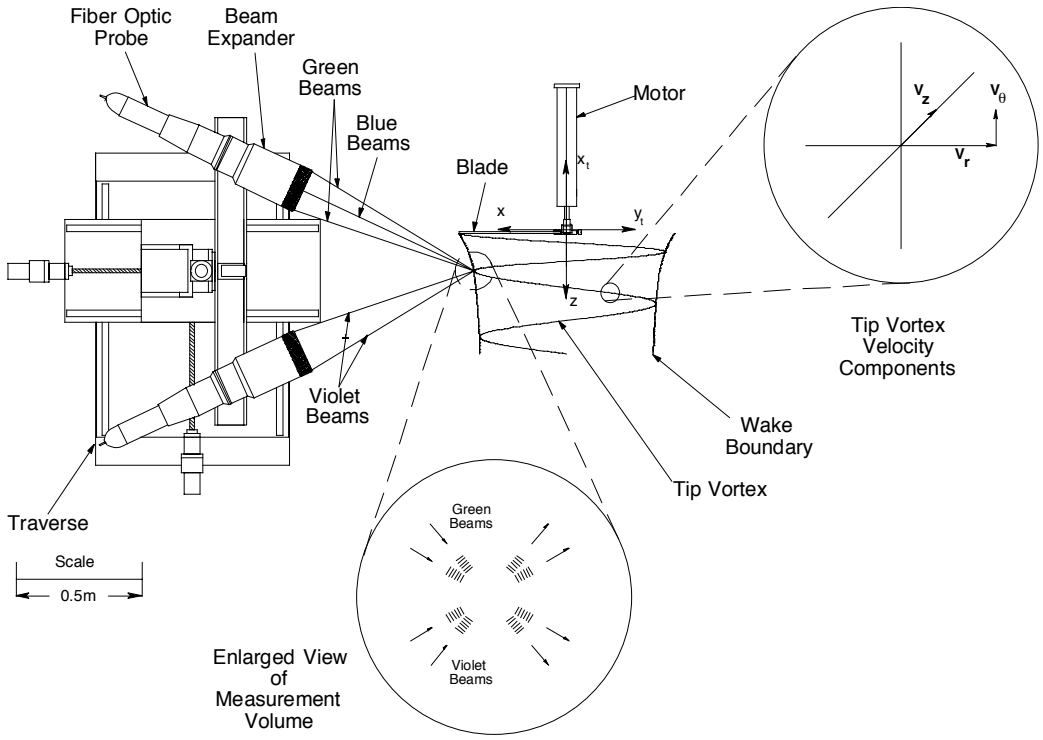

Figure 2.4: Setup of three-component LDV system.

expanders with focusing lenses of 750 mm were used to increase the beam crossing angles, and so to decrease the effective measurement volume.

To further reduce the effective size of the probe volume visible to the receiving optics, the off-axis backscatter technique was used, as described in Martin et al. [68] and Barrett & Swales [97]. This technique spatially filters the effective length of the LDV probe volume on all three channels. Spatial coincidence of the three probe volumes (six beams) and two receiving fibers was ensured to within a 15 μm radius using an alignment technique that is explained later in Section 2.1.6. Alignment is critical for three-component LDV systems because it is geometric coincidence that

determines the spatial resolution of the LDV probe volume. In the present case, the resulting LDV probe volume was measured to be an ellipsoid of dimensions 80 μm by 150 μ. For reference, this was about 3% of the maximum blade thickness or 0.5% of the blade chord.

2.1.5 Alignment Technique

Laser beam alignment is one of the crucial steps that determines the spatial resolution of the measurements and indirectly affects the quality of the LDV measurements. The uncertainty in the LDV beam crossing angles while quantifying the spatial resolution can be reduced by precisely aligning the laser beams [94]. A laser beam profiler was used in the current set of measurements to align the planes of both the 6 transmitting beams (3 shifted and 3 unshifted) and the 2 receiving beams, (a total of 8 beams) within a circle of 15 μm radius. This also enabled three-dimensional geometry of all three pairs of intersecting transmitting beams to be measured. The field of view of the receiving beam was also measured by transmitting light from the receiving fiber to the probe volume. Other than beam profiler, a most common way of aligning the beams is to use a pin hole probe. This technique was used by Barrett & Swales [97], and was found to be workable but was more time consuming for routine use than using a laser beam profiler.

Two main components of the beam profiler are a scan head and a rotating drum. The scan head allows multiple beams to be targeted onto a rotating drum. On the opposite side of the rotating drum, two slits that are 1 μm wide are oriented at 45° with respect to the rotation of the drum. As a result, one slit traverses the incident beam in the horizontal axis, while the other traverses along the vertical axis. The spatial accuracy of the beam profile measurement was found to be 14 μm radius, and

a typical standard deviation for the laser position measurement was 0.25 μm radius (using 50 samples at 10Hz). A single laser beam can be profiled in both the axes within few seconds.

The procedure starts by locating the coinciding point of both the two green beams (shifted and unshifted), and the two blue beams (shifted and unshifted). Power requirements limit the beam profiler to make measurements only on two beams at a time. However, by switching on the individual beams one by one, the profile of all the beams can be determined within minutes. The same procedure is repeated for the violet beams. After determining the spatial location of the point of coincidence of all the three pairs of beams, the location of the beams were adjusted by using individual controls to move all the three points of coincidence within a very small circle (less than 15 μm radius), giving a net measurement volume of 80 μm. The spatial location of the aligned beams at three different locations (600 μm apart) were then determined using the beam profiler, as shown in Fig. 2.5. This was used to determine the crossing angles. The crossing angles are required to convert the measured LDV data from non-orthogonal measurements to an orthogonal coordinate system.

Coordinate Transformation

In the current measurement, the coordinate axes corresponding to the LDV system are non-orthogonal. These system coordinates are converted to the tip vortex coordinates using a set of transformation equations. Figure 2.6 shows the schematic of both the coordinate systems (LDV and the tip vortex). In the two-probe, three component measurement that is used in the current experiments, two components of velocity were measured using a non-orthogonal system and the third component (axial velocity) was measured directly. It is apparent from Fig. 2.6 that the two green beams that

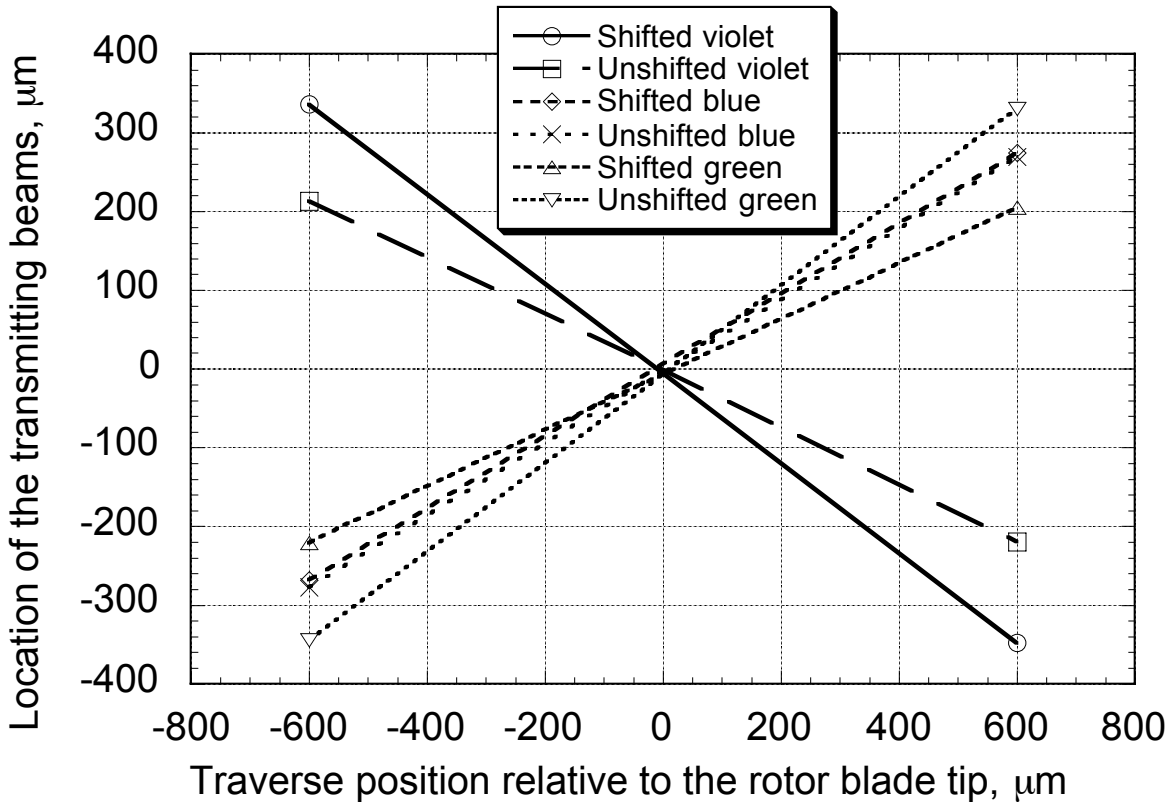

Figure 2.5: Location of the transmitting beams relative to the rotor blade tip measured using beam profiler.

measure the velocity V_g and the two violet beams that measure V_v are in the plane of the paper. The third component V_b, which is perpendicular to the plane of the paper was measured directly by the two blue beams. Based on the simple schematic that is shown in Fig. 2.6, the following coordinate transformation equations were obtained.

$$\begin{aligned} V_\theta &= a_1 V_g + b_1 V_v \\ V_r &= c_1 V_g + d_1 V_v \\ V_{ax} &= V_b \end{aligned} \tag{2.1}$$

where

$$\begin{aligned} a_1 &= \frac{\sin\theta_v}{\sin(\theta_g+\theta_v)} \qquad b_1 = \frac{\sin\theta_g}{\sin(\theta_g+\theta_v)} \\ c_1 &= \frac{\cos\theta_v}{\sin(\theta_g+\theta_v)} \qquad d_1 = \frac{-\cos\theta_g}{\sin(\theta_g+\theta_v)} \end{aligned} \tag{2.2}$$

Using these equations, the two components of velocity measured in the plane were resolved to get the tangential and radial velocities in the axis of the tip vortex.

2.1.6 Data Acquisition

The high capacity of the seeder allowed the entire test cell to be uniformly seeded in approximately 30 seconds. Signal bursts from seed particles passing through the measurement volume were received by the optics, and transmitted to a set of photo multiplier tubes where they were converted to analog signals. This analog signal was low band pass filtered to remove the signal pedestal and any high frequency noise. The large range of the low band pass filter was required to allow measurement of the flow reversal associated with the convection of a vortex core across the measurement grids. The analog signal was digitized and sampled using a digital burst correlator.

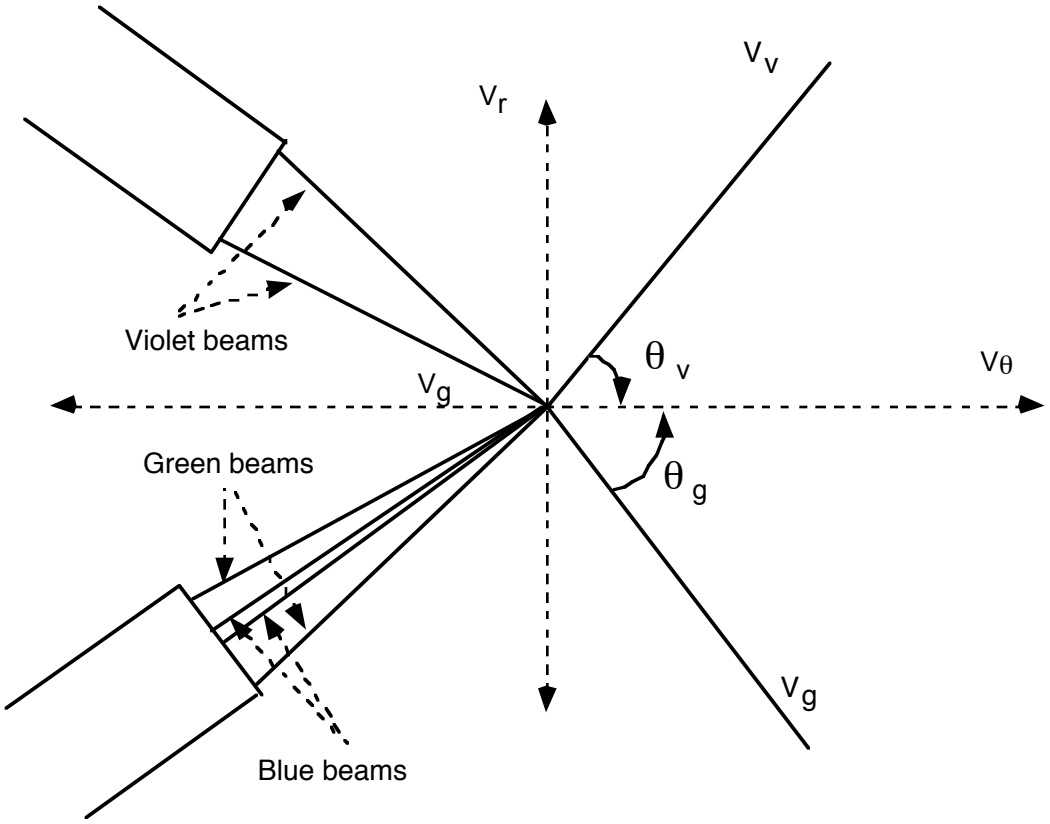

Figure 2.6: Schematic showing the LDV and vortex coordinate systems for performing coordinate transformation.

The flow velocities were then converted into three orthogonal components based on the measurements of the beam crossing angles.

Each measurement was phase-resolved with respect to the rotating blade by using a rotary encoder. This tagged each data point with a time stamp. The temporal phase-resolution of the encoder was 0.1°, but the measurements were averaged into one-degree bins. The uncertainty in this process has been discussed by Martin et al. [8].

2.1.7 Aperiodicity Correction

Aperiodicity is the inherent random movement of the phase resolved spatial locations of the vortex cores. Measurements of aperiodicity were made using laser light sheet illumination of the seeded flow. As previously described, a laser pulse duration on the order of nanoseconds was achieved using an Nd:YAG laser. The laser was synchronized to the rotor so that the aperiodicity of the core position could be measured at the same wake age. The images were digitized to quantify the vortex position with respect to a calibration grid. A total of 300 such images were taken for each wake age, which is essential in determining the aperiodicity statistics of the rotor wake. Determining the spatial location of the tip vortex accurately directly translates into an accurate estimation of strain exerted on the vortex filaments.

The standard deviations of the core position in the radial and axial direction are given in Fig. 2.7. It can be seen that the standard deviation is small at earlier wake ages and then gradually increases to higher values at older wake ages. Moreover, the standard deviation is isotropic ($\sigma_z = \sigma_r$) at earlier wake ages. At older wake ages, anisotropic levels of aperiodicity were found. The measured correlation coefficient of the standard deviation for different wake ages is shown in Fig. 2.8.

In general, the effects of aperiodicity appear as a reduction in peak swirl velocity

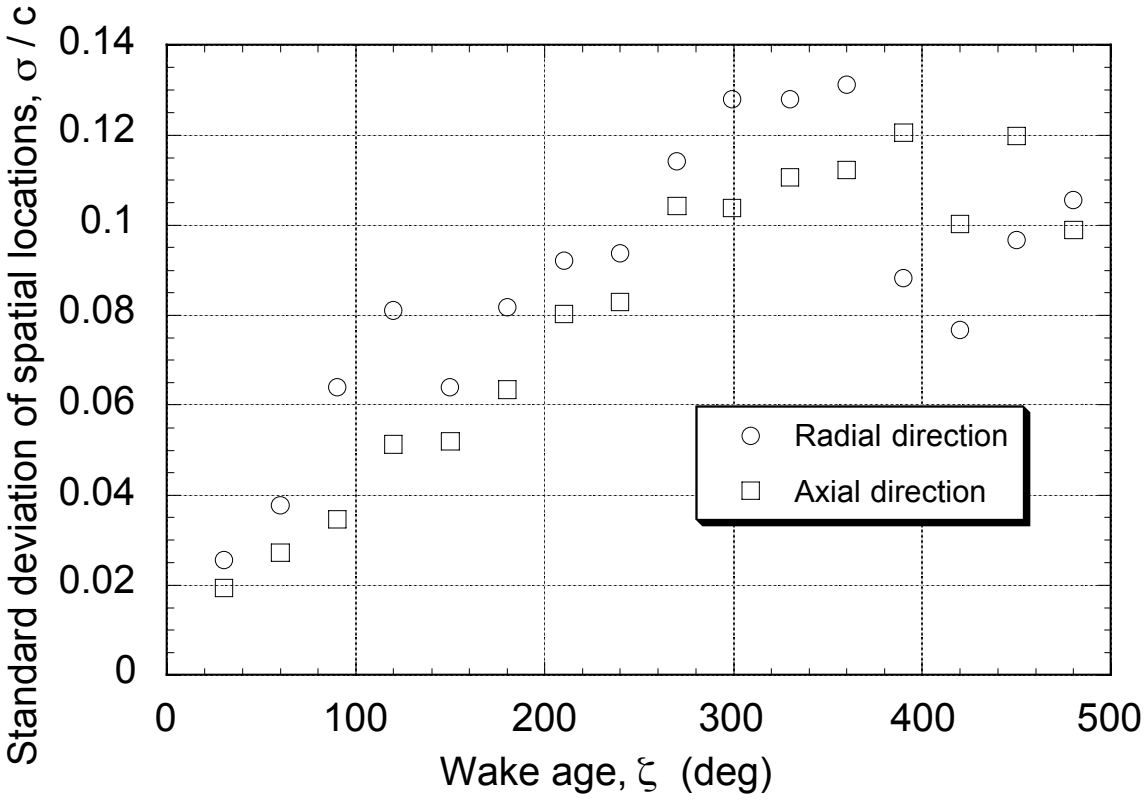

Figure 2.7: Standard deviation of radial and axial locations of rotor tip vortices at different wake ages.

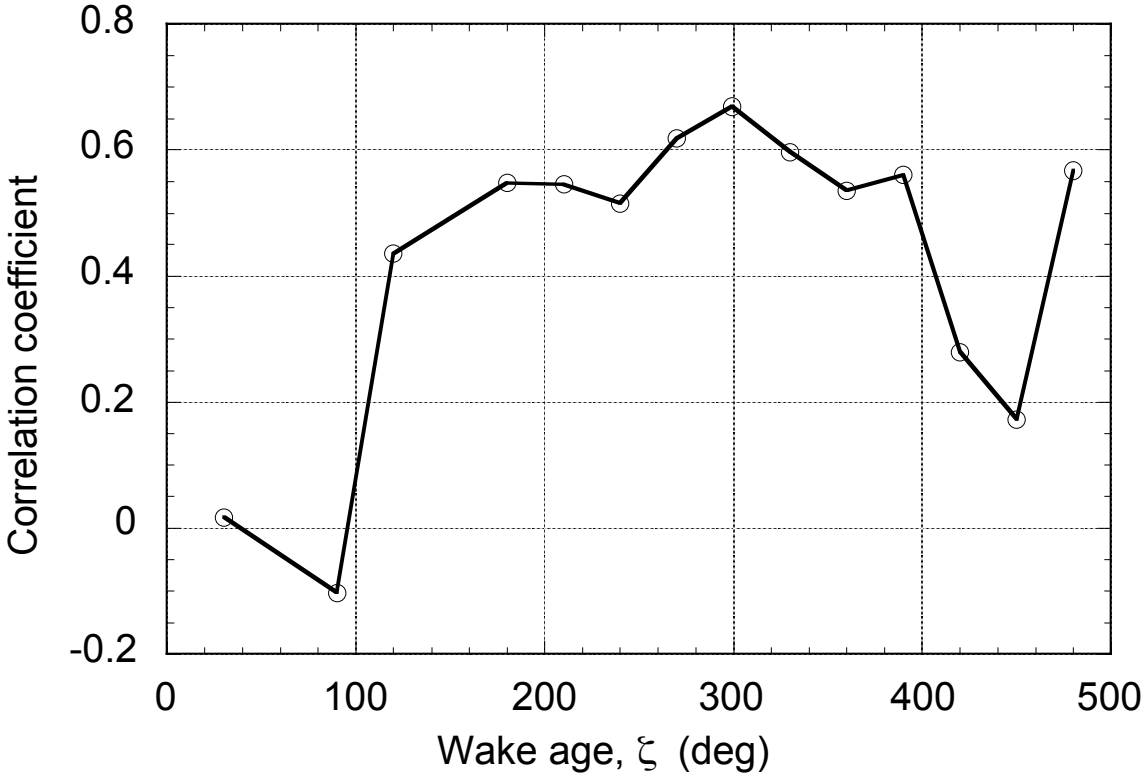

Figure 2.8: Correlation of the standard deviation between radial and axial spatial locations of the rotor tip vortices at different wake ages.

with an increased core size. Therefore, failing to correct for these levels of aperiodicity could result in misinterpretation of the measured results. Various theories have been put forth by different researchers to correct the measurements for these effects. Devenport et al. [81] developed a theory to correct the measurements of vortices generated by fixed-wings. A scheme to numerically correct the aperiodic flow effects of the tip vortices that occur in rotor flow field was developed by Leishman [98]. The difference between the two schemes is that Leishman's scheme requires direct measurement of aperiodicity whereas Devenport's scheme relies upon the mean flow for the estimate of aperiodicity.

Correcting the velocity profiles is not only a problem for LDV, but also for PIV measurements. Determining the exact center of the tip vortex images obtained using PIV is essential to perform the ensemble averaging, one of the important steps in obtaining a velocity profile from the images. Determining an incorrect center of circulation would artificially introduce errors and can result in very incorrect and misleading results.

Grid resolution is also one of the important parameters in determining the center of the vortex accurately. Heyes et al. [99] performed an experiment on a NACA 0012 airfoil and measured the wandering of the tip vortices using PIV. A correction procedure based on statistical analysis and Monte-Carlo simulation that resulted only in limited success in correcting for aperiodicity. Very few studies have been made to understand the source for the aperiodicity of tip vortices. Gurusul et al. [100] made measurements on a delta-wing, and suggested that the wandering of tip vortices should be a result of a Kelvin-Helmholtz instability of the shear layer that separated from the leading edge of the delta wing. In the current study, the measurements were corrected using Leishman's [69] scheme. The sequence of steps involved in making

the correction are given in Appendix A.

2.2 Theoretical Approach

2.2.1 Introduction

An improved modeling capability of the tip vortices will directly translate in to improved predictions of rotor performance and airloads. A complete description of a viscous trailing vortex requires a complete solution to the Navier–Stokes equations. Closed form, analytical solution to these non-linear set of equations is not possible atleast not without major simplifications and assumptions. Numerical solutions are limited by computational resources. Most existing models of today are developed either: (i) Analytically by making various assumptions and approximations to the N–S equation (e.g., Lamb–Oseen [58], or Squire models [13]), or (ii) Entirely empirical, and without explaining any flow physics (e.g., Cook model [16]), or (iii) Semi-empirically by obtaining empirical constants from the measurements to develop a model (e.g., Hoffman & Joubert [64], Tung [43] and Iversen models [59]).

It should be kept in mind that the empirical constants are obtained using measurements that are more often than not performed using sub-scale rotors with resulting tip vortex Reynolds numbers that are much lower than the full-scale flight values. Therefore, predicting the vortex flow physics of the full-scale flight velocities with the help of a model that is developed using measurements from sub-scale rotor may not be appropriate. This is a subject discussed in the present work. A brief overview of three existing vortex models (Lamb–Oseen, Squire and Iversen models), which are used extensively in aerodynamics are now given so as their advantages and limitations can be appreciated, and what aspects are required to improve these models for rotating-wing

work.

Vortex Models

The incompressible momentum equation for a one-dimensional, axisymmetric vortex in polar coordinates are given by

$$\rho \frac{DV_\theta}{Dt} = \frac{\partial}{\partial r}\left[\mu_T \frac{\partial V_\theta}{\partial r} - \mu_T \frac{V_\theta}{r}\right] + \frac{2\mu_T}{r}\left[\frac{\partial V_\theta}{\partial r} - \frac{V_\theta}{r}\right] \tag{2.3}$$

Writing Eq. 2.3 in terms of local circulation, γ, and kinematic viscosity, ν_T, results in

$$\frac{\partial \gamma}{\partial t} = r\frac{\partial}{\partial r}\left[\nu_T r \frac{\partial}{\partial r}\left(\frac{\gamma}{r^2}\right)\right] + 2\nu_T\left[r\frac{\partial}{\partial r}\left(\frac{\gamma}{r^2}\right)\right] \tag{2.4}$$

Exact solutions to this equation can be obtained by assuming that the viscosity of the flow has the form

$$\nu_T = \nu + \nu_t \tag{2.5}$$

where ν is the kinematic viscosity (a property of the fluid) and ν_t is the "eddy" viscosity, which is a result of turbulent mixing and interchange of fluid.

Lamb–Oseen Model

The classic Lamb–Oseen vortex model [58] is an exact solution to Eq. 2.4 under the assumption that $\nu_t = 0$ (i.e., fully laminar flow). The swirl velocity, V_θ, surrounding an isolated vortex filament from this model is given by

$$V_\theta(r) = \frac{\Gamma}{2\pi r}\left[\, 1 - \exp(-\eta_L) \,\right] \tag{2.6}$$

where η_L is the similarity variable proposed by Lamb ($\eta_L = r^2/4\,\nu\,t$). For time $t > 0$ the distribution of swirl velocity versus the non-dimensional radial distance for the Lamb–Oseen model is shown in Fig. 2.9. It is apparent that the peak swirl velocity

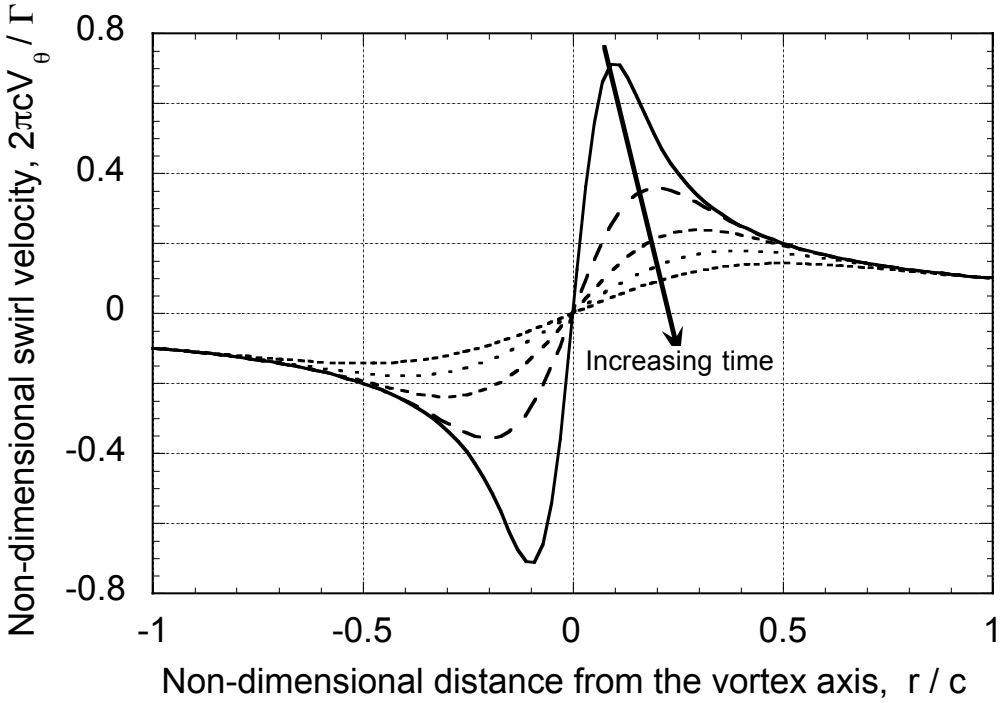

Figure 2.9: Swirl velocity distribution for an aging vortex as predicted by the laminar Lamb–Oseen model.

decreases and the core radius decreases with time, indicating diffusion of vorticity away from the vortex core. However, the Lamb–Oseen model approaches a singularity at time $t = 0$, which is not physically realistic. Moreover, because this model is developed by making a laminar flow assumption, molecular diffusion is the only source of momentum transport. In this case, the growth of the viscous core with time is given by

$$r_c(t) = \sqrt{4\alpha_{\mathrm{L}}\nu t} \tag{2.7}$$

where α_{L} is Lamb's constant ($\alpha_L = 1.25643$). This result, however, is found to be unrealistically slow in light of experimental evidence (e.g., Refs. 7, 8, 38), as also shown in Fig. 2.10. Equation 2.6 can also be written in terms of core radius, r_c, as

$$V_\theta(\bar{r}) = \frac{\Gamma_v}{2\pi r_c}\left[\frac{1 - e^{-\alpha_{\mathrm{L}}\bar{r}^2}}{\bar{r}}\right] \tag{2.8}$$

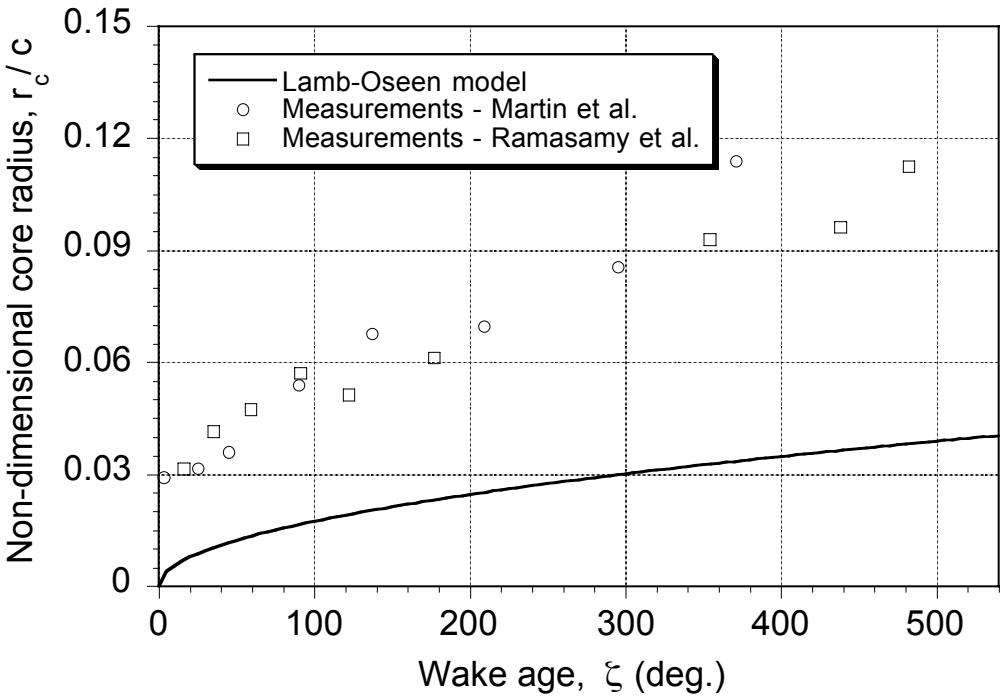

Figure 2.10: Core radius as a function of wake age for an aging vortex as predicted by the laminar Lamb–Oseen model.

where $\overline{r}$ is the non-dimensional radial distance (r/r_c).

Squire's Model

Squire [13] modified the vortex core growth obtained from the Lamb–Oseen model to include an average eddy viscosity component to account for the effects of turbulence. Because the principal permanent characteristic of a line vortex is its circulation at large distances from the core axis, Squire assumed that the eddy viscosity was proportional to the vortex circulation, Γ_v. The total viscosity was assumed to be of the form

$$\nu_T = \nu + a\left(\frac{\Gamma_v}{2\pi}\right) \tag{2.9}$$

where a is an empirical constant determined from experiments.

It should be noted that the "eddy" component of viscosity was assumed to be constant with radial distance, r, and so it represents an average eddy viscosity throughout the structure of the vortex, which may not represent the true physics. In this case, the modified growth rate of the vortex core is given by a simple modification to Eq. 2.7 as

$$r_c(\zeta) = \sqrt{4\alpha_L \delta\nu\left(\frac{\zeta}{\Omega}\right)} = \sqrt{\frac{4\alpha_L \delta\nu\zeta}{\Omega}} \tag{2.10}$$

where δ is defined as the ratio of the total to kinematic viscosity, i.e.,

$$\delta = \frac{\nu_T}{\nu} = 1 + \frac{a}{2\pi}\left(\frac{\Gamma_v}{\nu}\right) = 1 + a_1\left(\frac{\Gamma_v}{\nu}\right) \tag{2.11}$$

Notice that the Squire model reduces to the Lamb–Oseen model when $\delta = 1$. The value of $a/2\pi$ in Eq. 2.9 (which is normally represented by the coefficient a_1) was estimated by Bhagwat & Leishman [101] to lie between the values of 0.00005 and 0.0002 based on nearly all of the available experiments on tip vortices conducted over a wide range of Reynolds number – see Fig. 2.11. Squire [13] also proposed an effective or virtual origin offset to eliminate the singular nature of the Lamb–Oseen

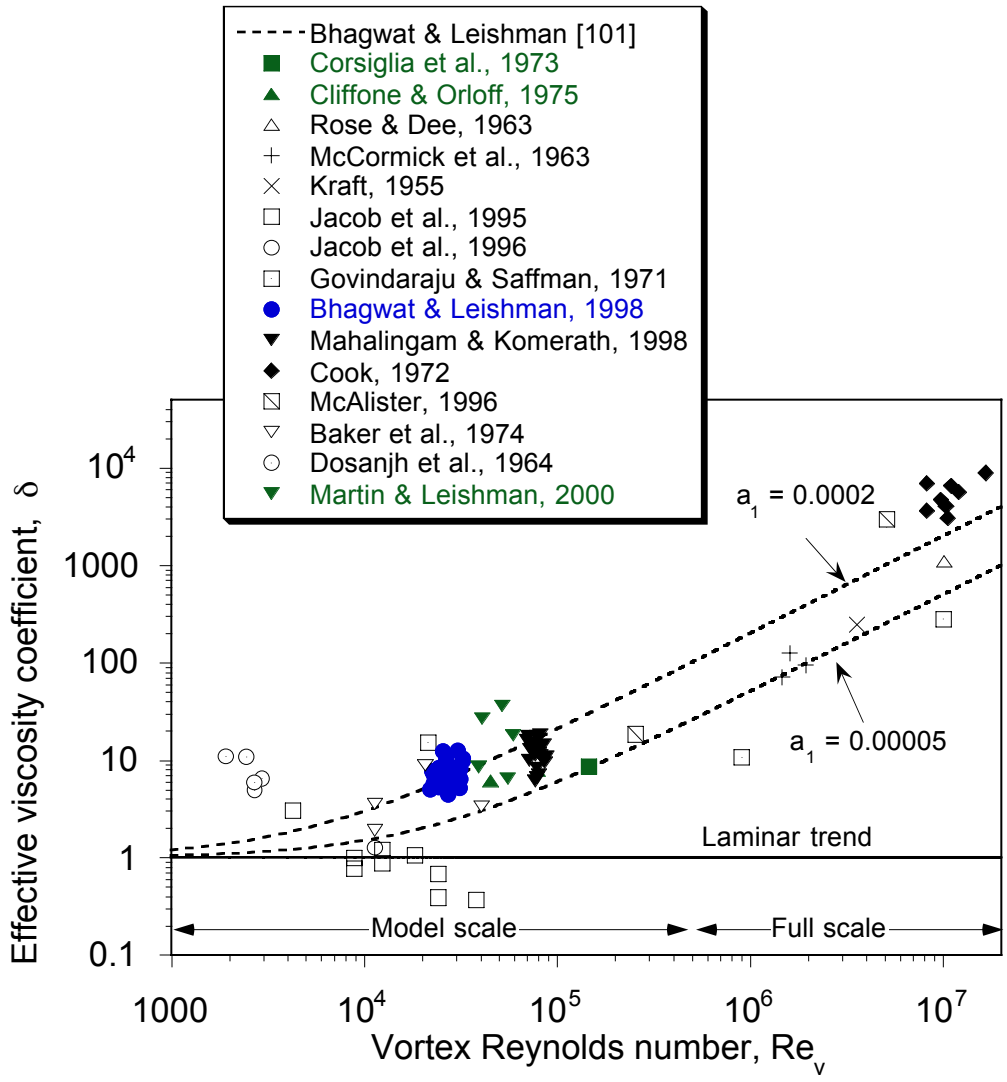

Figure 2.11: Determination of the value of apparent to actual viscosity ratio, δ from various experiments [101].

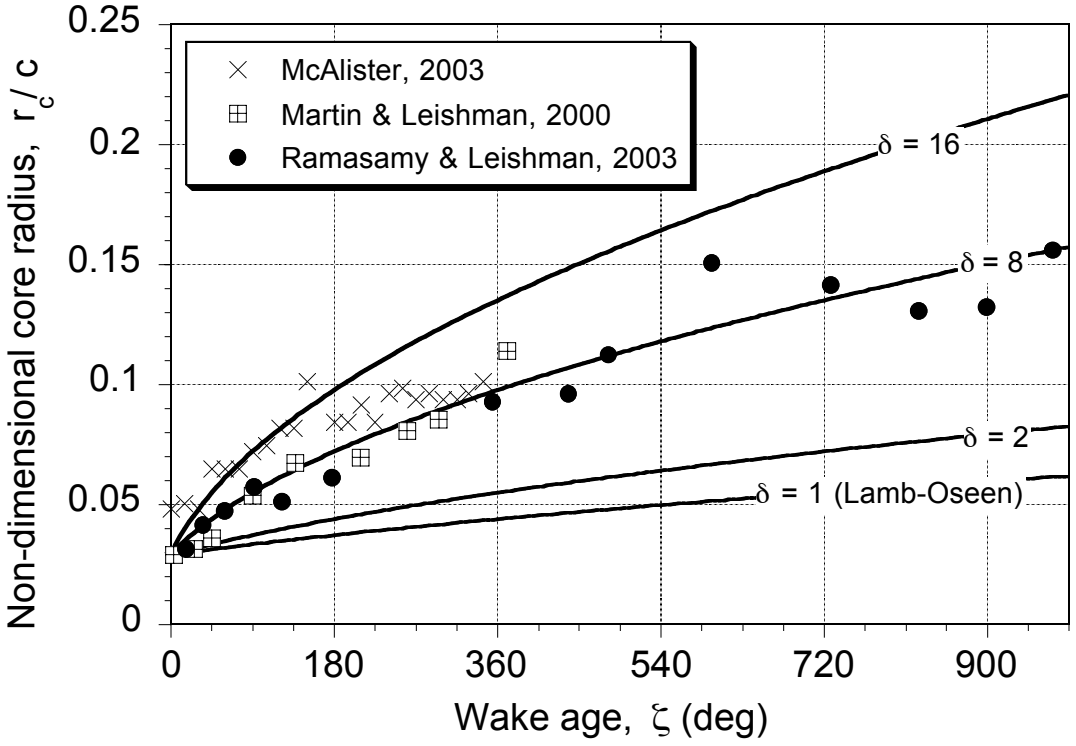

Figure 2.12: Vortex core growth predicted by Squire's model, ($\zeta_0 = 30\,\text{deg}$) in comparison with experimental data.

vortex. As a result, Eq. 3.4 can be written in the form for helicopter rotor applications as

$$r_c(\zeta,\delta) = \sqrt{4\alpha_L \delta\nu\left(\frac{\zeta-\zeta_0}{\Omega}\right)} \equiv \sqrt{r_0^2 + \frac{4\alpha_L\delta\nu\zeta}{\Omega}} \tag{2.12}$$

where r_0 is the core radius of the tip vortex at time $t = 0$.

Figure 2.12 shows the increase in size of the vortex core with wake age for various assumed values of δ. Clearly, increased values of δ lead to an increased core growth rate. These two modifications (turbulent diffusion and core growth offset) have been shown to result in a more physically realistic representation of the vortex growth rate that correlates better with experimental measurements (e.g., Ref. 7, 8, 38), as also

shown in Fig. 2.12.

Iversen Model

Iversen [59] proposed a turbulent vortex model using a variation of Prandtl mixing length theory. In this model, the eddy viscosity was assumed to vary across the radial dimension of the vortex. The mixing length proposed by Iversen increased linearly with the radial distance; this linear dependency was modeled empirically based on various vortex measurements. The total viscosity variation across the vortex was assumed to vary as

$$\nu_T = \nu + l^2 \left| r \frac{\partial}{\partial r} \left(\frac{\gamma}{r^2} \right) \right| \tag{2.13}$$

where $l = \alpha_I r$ represents the mixing length. The value of α_I (Iversen's constant) was determined by analyzing results from a specific set of experiments [52–54] to be 0.01854. Using dimensional analysis, Iversen determined a similarity variable $\eta = r^2/4\gamma_v\, t$, which is $2\pi\eta_L/Re_\nu$, where η_L is the similarity variable used by Lamb [58].

By performing a similarity transformation on Eq. 2.4, the circulation distribution of an isolated line vortex (based on the form of the eddy viscosity variation given in Eq. 2.13) is given by

$$\frac{\partial \overline{\gamma}}{\partial \overline{\eta}} = -\left[\frac{\nu}{\gamma_v\, \alpha_I^2} + 4|\overline{\eta} \frac{\partial \overline{\gamma}}{\partial \overline{\eta}} - \overline{\gamma}| \right] \tag{2.14}$$

where $\overline{\eta} = \eta/\alpha_I^2$. Iversen obtained a similarity solution to the above equation as a function of vortex Reynolds number (i.e., as a function of Γ_v/ν). This similarity solution helped Iversen derive a correlation function in terms of vortex Reynolds number that can be used to compare measurements performed at various vortex Reynolds numbers, as shown in Fig. 2.13. Swirl velocity profiles at different vortex Reynolds numbers can then be obtained using the similarity solution, which are shown in Fig. 2.14.

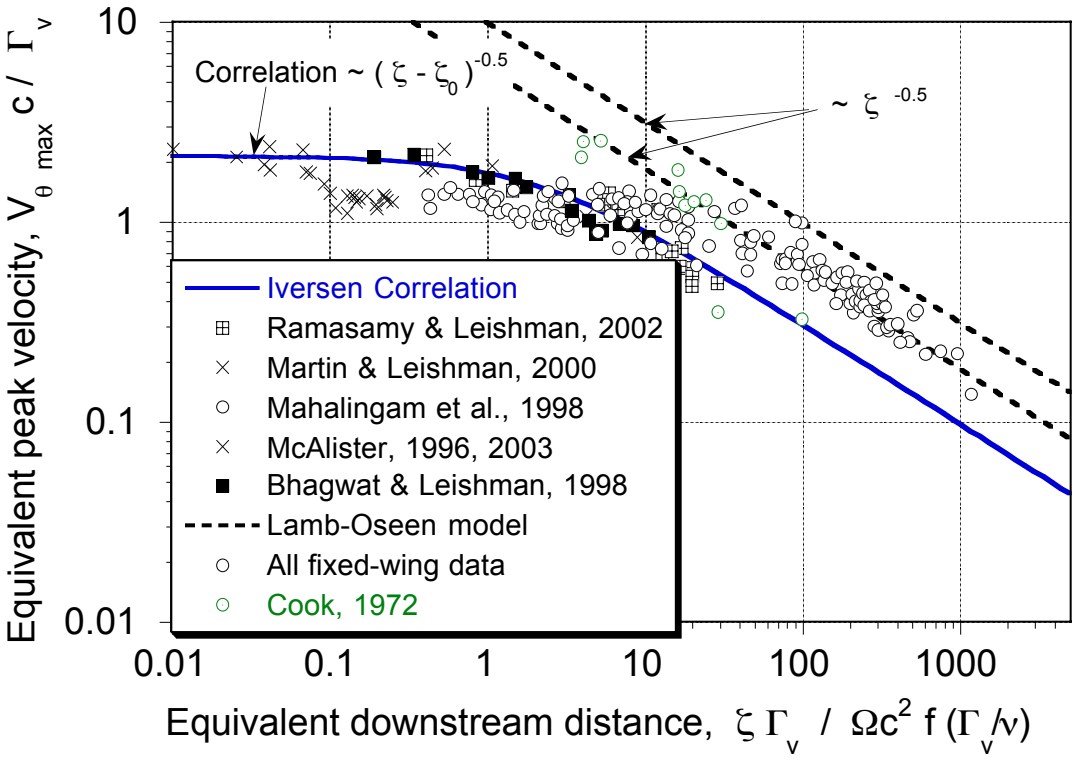

Figure 2.13: Iversen–type correlation of peak swirl velocity with equivalent downstream distance for fixed-wing and rotor tip vortex measurements.

It can be seen that Iversen's model properly reduces to the laminar Lamb–Oseen model at very low vortex Reynolds numbers, as it should.

Based on the variable eddy viscosity model given in Eq. 2.13, Iversen predicted a core growth of a tip vortex that is dependent on the vortex Reynolds number, the result which is shown in Fig. 2.15.

At very low Reynolds numbers, $\delta = 1$ (fully laminar flow). As the Reynolds number increases above 10^3, the value of δ increases until it changes linearly with vortex Reynolds number. Because Squire's model predicts a linear increase of δ at higher Reynolds numbers, it can be concluded that Squire's model is really valid only at high Reynolds numbers (i.e., for $Re_v > 10^5$). Even though the core growth predicted by Iversen is more physically realistic compared to measurements, it should

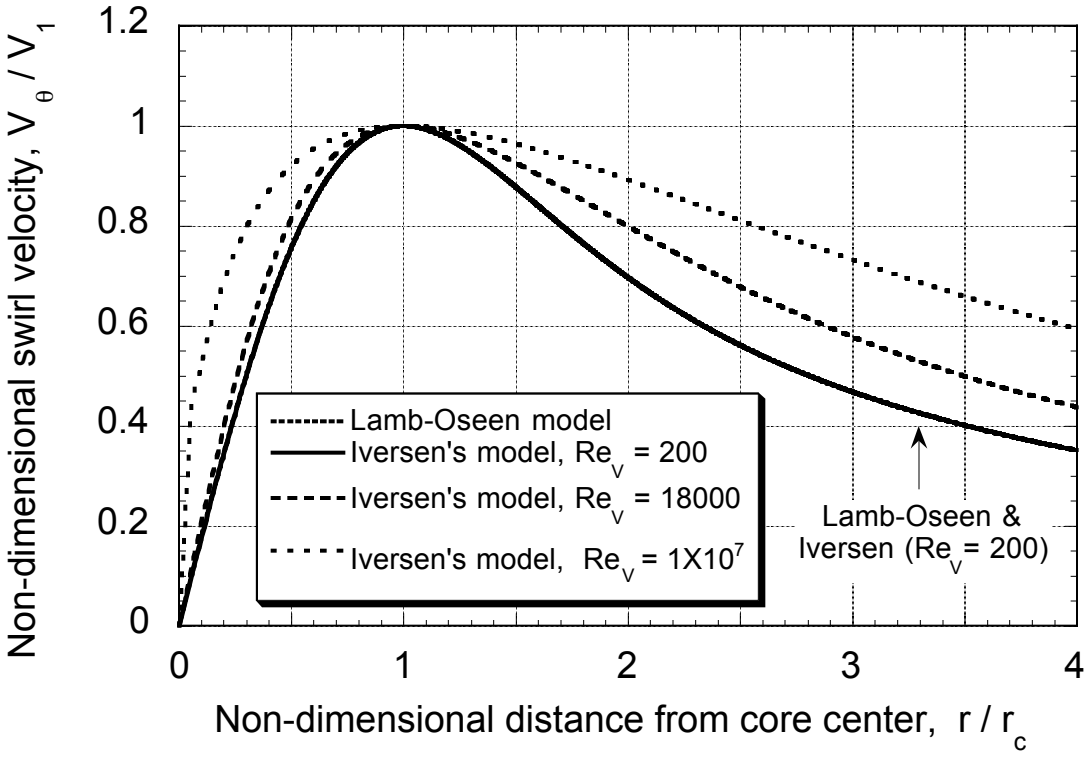

Figure 2.14: Swirl velocity distribution predicted by Iversen model at various vortex Reynolds numbers.

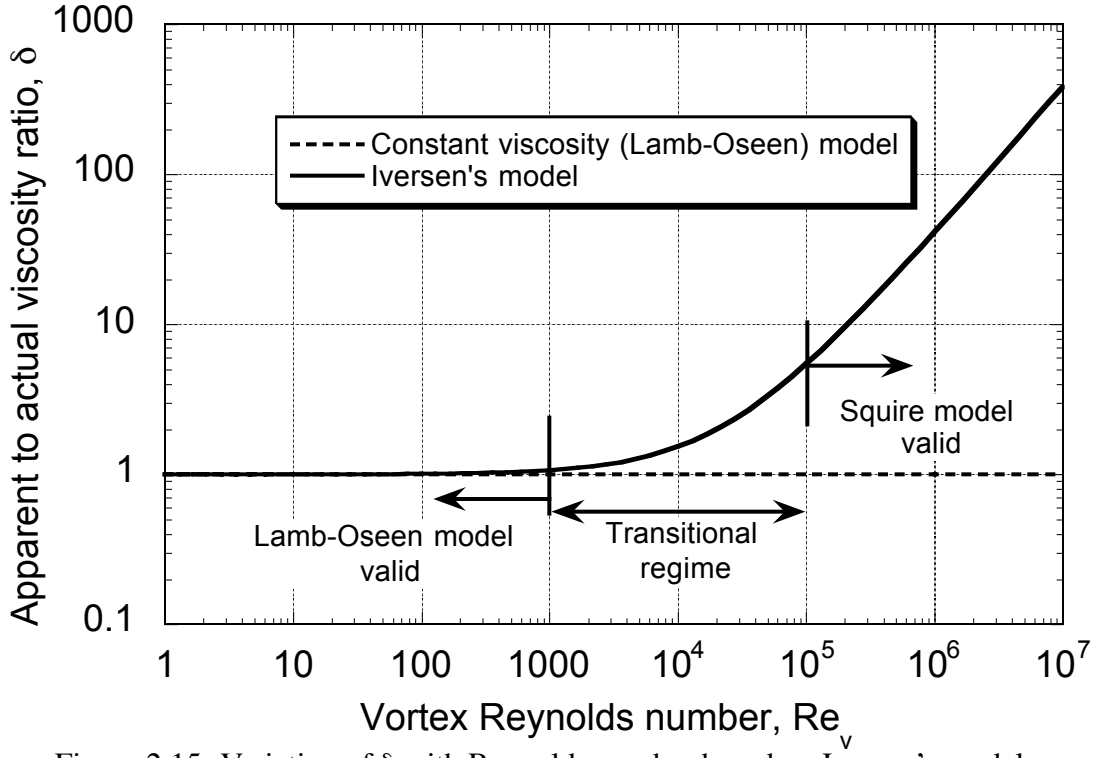

Figure 2.15: Variation of δ with Reynolds number based on Iversen's model.

be kept in mind that the measurements used in developing this model are subject to several uncertainty issues. these uncertainties include vortex core wandering effects, and so the value of α_I may be unreliable if not corrected for these effects (e.g., see also Refs. 98, 102).

2.2.2 Structure of the Tip Vortex

Because flow field instrumentation has improved since the 1970s, more accurate flow measurement techniques have been developed with the spatial resolution necessary for making better measurements of vortex flows. This has resulted in more reliable and higher fidelity measurements [7, 8, 38]. New techniques have also been developed to measure and correct for the effects of core wandering [98, 102]. These measure-

ments, which have been performed only over the past few years, have consistently suggested a multi–region vortex structure. For example, flow visualization performed on a tip vortex emanating from a rotating blade that was shown in Fig. 1.8 suggests a multi-region vortex structure. This multi-region vortex structure concept differs from the above mentioned models in a way that it is neither completely laminar like Lamb–Oseen model nor completely turbulent like Squire's or Iversen's model. Recent velocity measurements made using LDV [38, 103] also support the idea of a multi-region or transitional structure of the tip vortex. As shown in Fig. 2.16, the measurements match the Lamb–Oseen results near the core and match the turbulent (Iversen) model well away from the core.

2.2.3 Effects of Flow Rotation on Tip Vortex Development

Rayleigh's Instability Theory

The effects of flow rotation on the development of turbulence present inside the vortex has been hypothesized to play an important role in determining the overall structure and development of a vortex (e.g., Refs. 64,65,104). Rayleigh's centrifugal instability theory [60], which uses a buoyancy force concept, suggests that the vortex will never develop turbulence provided that the product of velocity and radial distance increases with the increase in radial coordinate. Only a few vortex models (e.g., Refs. 10, 63) have been developed that recognize this concept, but have achieved limited success in application [10, 62]. The various properties of the vortex flow predicted using these models, such as its core growth and the distribution of velocity with radial distance, did not correlate well with experimental results [53].

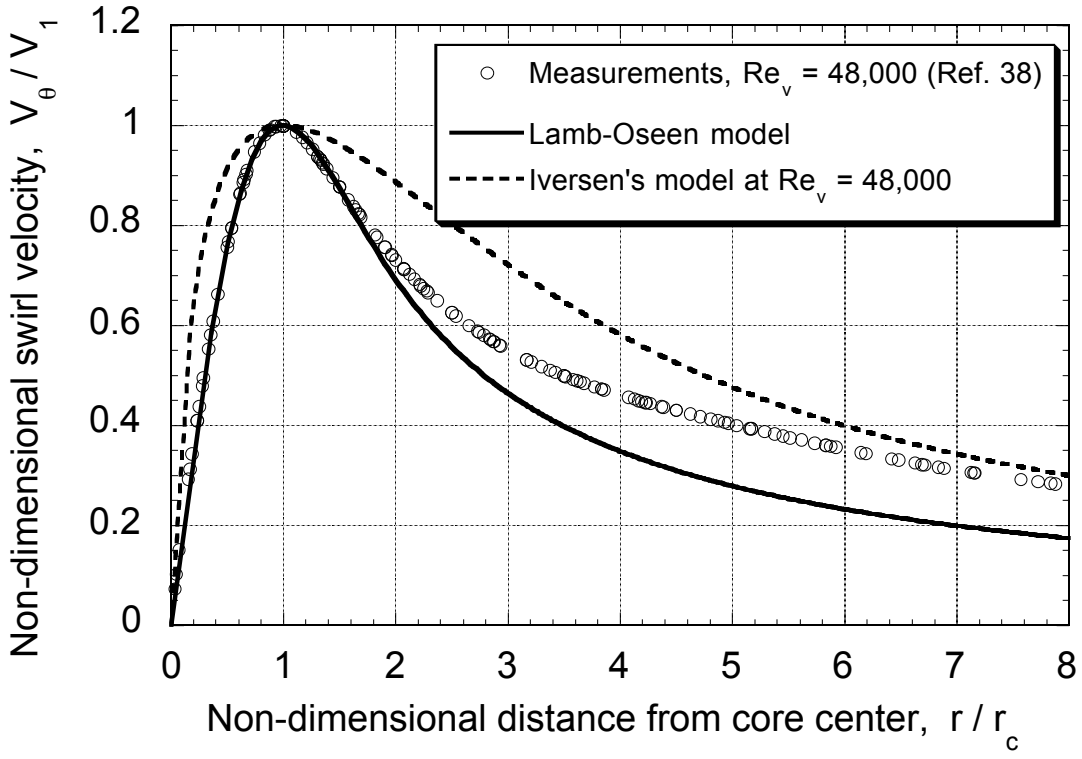

Figure 2.16: Swirl velocity distribution of a tip vortex using Lamb–Oseen and Iversen models compared to measurements.

2.2.4 Analogy of Rotating and Stratified Flows

Bradshaw [61] developed an analogy between rotating flows and stratified fluids. This approach is based on the theory that the flow rotation causes the higher speed fluid to prefer the outside of the vortex while conserving angular momentum, even if the density is assumed constant throughout the vortex. Using energy principles, an expression was developed for the local strength of the analogous stratification, expressed as an equivalent gradient Richardson number. This number comes directly from the turbulent kinetic energy (TKE) budget equation (e.g., Refs. 61, 104) and is basically a ratio of the turbulence produced or consumed inside the vortex as a result of buoyancy (centrifugal effects) to the turbulence produced by shearing in the flow. It can also be thought of as the ratio of potential to kinetic energy in a stratified flow.

In a swirling flow, Bradshaw's "Richardson number" is given by

$$Ri = \left(\frac{2V_\theta}{r^2}\frac{\partial(V_\theta r)}{\partial r}\right) \Big/ \left(\frac{\partial V_\theta}{\partial r}\right)^2 \tag{2.15}$$

which involves the swirl velocity gradients, $\partial V_\theta/\partial r$, in the vortex flow. Bradshaw derived the numerator and denominator of the above expression in two different frames of reference. This is misleading because this results in a maximum stability at the core radius of the vortex [65]. Holzapfel [104] corrected the definition of Richardson number by taking both the denominator and numerator in the same inertial frame of reference. The corrected Richardson number proposed by Holzapfel is given by

$$Ri = \left(\frac{2V_\theta}{r^2}\frac{\partial(V_\theta r)}{\partial r}\right) \Big/ \left(r\frac{\partial\,(V_\theta/r)}{\partial r}\right)^2 \tag{2.16}$$

It should be noted that this form of the Richardson number has strain rate in the denominator instead of plane shear.

2.2.5 Richardson Number Effects

Cotel & Breidenthal [65] and Cotel [66] used the foregoing stratification concept and has determined a threshold value for the Richardson number that is a function of vortex Reynolds number. Their analysis is based on a non-dimensional parameter called a "Persistence Parameter," which is defined as the ratio of rotational to translational speed of the vortex. If the persistence parameter is high, which is the case for most wing generated tip vortices (including rotorcraft), the threshold value of the Richardson number was found to be $Re_{\mathrm{v}}{}^{1/4}$ based on an idealized experiment [105]. This means that the vortex will be laminar up to a radial distance from the vortex axis where the local gradient Richardson number remains below this threshold value. Any turbulence present inside this boundary will be either relaminarized or suppressed.

The local gradient Richardson number calculated using measurements (from Ramasamy et al. [38]) are shown in Fig. 2.17, along with the Lamb–Oseen and Iversen vortex models. The Richardson number variation for both the vortex models (and the measurements) is seen to approach infinity at the center of the vortex. As the radial distance from the center of the vortex increases, the Richardson number quickly reduces in value and goes below the assumed stratification threshold (i.e., for values of Ri above the stratification threshold only laminar flow is possible). In this region, diffusion at a molecular level will be the only means to transport momentum in fluid flow. This concept helps explain the persistence of tip vortices, in general, to relatively old wake ages (3, 4, or even 5 rotor revolutions). Below the stratification threshold, turbulence can develop. This argument serves to augment the hypothesis of a multi-region vortex that is nearly always laminar inside the core region, which then progressively transitions to turbulence outside the vortex core. This mechanism, therefore, affects the induced velocity field.

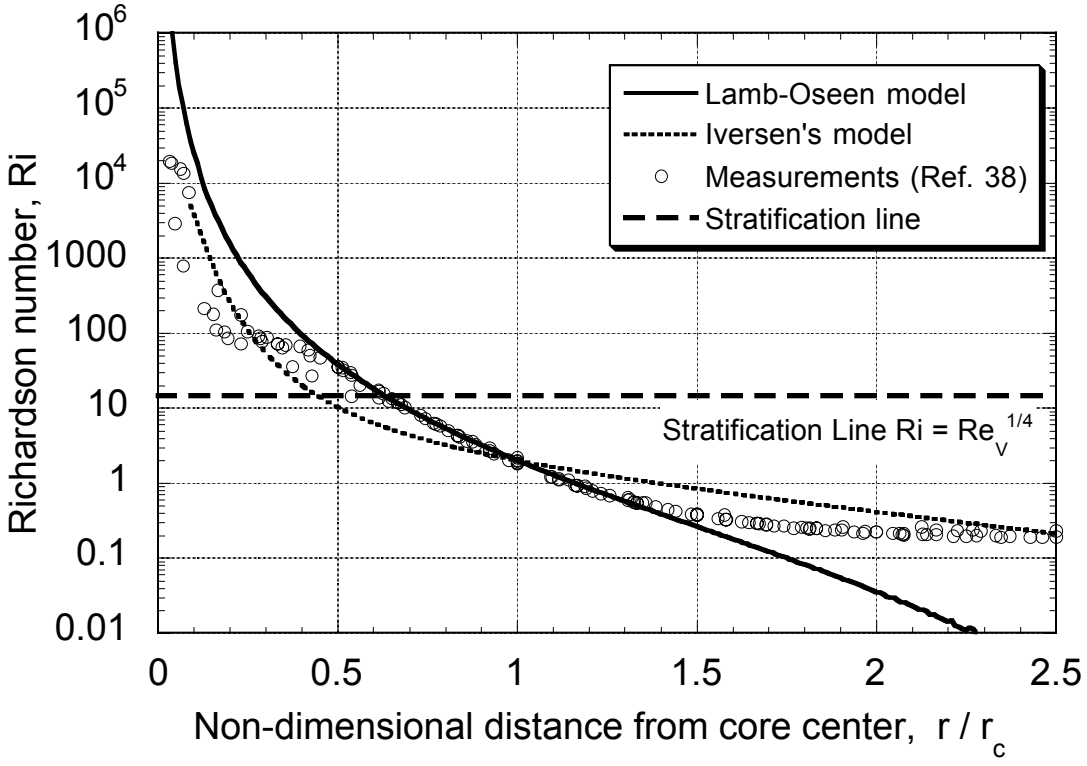

Figure 2.17: Representative plot of Richardson number with radial coordinate for a vortex flow.

2.2.6 New Vortex Model

The new vortex model developed in the present work recognizes the foregoing described effects of flow rotation on the turbulence developments within the vortex core. The incompressible momentum equation for a one-dimensional, axisymmetric vortex in cylindrical coordinates is given by

$$\frac{DV_\theta}{Dt} = \frac{\partial}{\partial r}\left[\nu_T \frac{\partial V_\theta}{\partial r} - \nu_T \frac{V_\theta}{r}\right] + \frac{2\nu_T}{r}\left[\frac{\partial V_\theta}{\partial r} - \frac{V_\theta}{r}\right] \tag{2.17}$$

An assumption of one dimensional, axisymmetric vortex results in the axial and the radial velocities of the vortex along with any variation in the axial and radial direction to be zero, i.e.,

$$V_z = V_r = 0$$

and

$$\frac{\partial}{\partial \theta} = \frac{\partial}{\partial z} = 0$$

This implies that $DV_\theta/Dt = \partial V_\theta/\partial t$ and, therefore, Eq. 2.17 becomes

$$\frac{\partial}{\partial t}\left(\frac{\gamma}{r}\right) = \frac{\partial}{\partial r}\left[\nu_T \frac{\partial}{\partial r}\left(\frac{\gamma}{r}\right) - \nu_T \frac{\gamma}{r^2}\right] + \frac{2\nu_T}{r}\left[\frac{\partial}{\partial r}\left(\frac{\gamma}{r}\right) - \frac{\gamma}{r^2}\right] \tag{2.18}$$

where γ is given by the product $V_\theta\, r$. But,

$$r\frac{\partial}{\partial r}\left(\frac{\gamma}{r^2}\right) = r\left[\frac{1}{r^2}\frac{\partial \gamma}{\partial r} - \frac{2\gamma}{r^3}\right] = \frac{1}{r}\left[\frac{\partial \gamma}{\partial r} - \frac{2\gamma}{r}\right] \tag{2.19}$$

and also

$$\frac{\partial}{\partial r}\left(\frac{\gamma}{r}\right) - \frac{\gamma}{r^2} = \frac{1}{r^2}\left[\frac{\partial \gamma}{\partial r} - \frac{2\gamma}{r^2}\right] \tag{2.20}$$

Upon substituting these latter two equations into Eq. 2.18, the distribution of circulation for a tip vortex with a variable effective viscosity is given by

$$\frac{\partial \gamma}{\partial t} = r\frac{\partial}{\partial r}\left[\nu_T r \frac{\partial}{\partial r}\left(\frac{\gamma}{r^2}\right)\right] + 2\nu_T\left[r\frac{\partial}{\partial r}\left(\frac{\gamma}{r^2}\right)\right] \tag{2.21}$$

This equation is made using an assumption that the flow inside the vortex is analogous to the time dependent flow of an infinite line vortex.

A classical way [106] of writing the total viscosity ν_T is

$$\nu_T = \nu + \nu_t = \nu + l^2|\sigma| \tag{2.22}$$

where $l = \kappa r$ is the mixing length and $|\sigma|$ is the time-average of the shear stress inside the flow of the tip vortex. Assuming a value of $\kappa = 0$ would result in constant viscosity model. A non-zero constant value for κ (i.e., using Iversen's value of $\kappa = \alpha_I = 0.01854$) will result in a completely turbulent flow model. In the new model, κ is considered as a function of r and is varied in a manner analogous to the intermittency function used in boundary layer theory (e.g., Refs. 107, 108). Assuming the flow in the vortex to be self-similar, a similarity variable η is obtained from a dimensional analysis that is given by

$$\eta = \frac{r^2}{4\gamma_v t} \tag{2.23}$$

which is in agreement with Iversen's model.

The next step is to get Eq. 2.21 in terms of the similarity variable η. Let Eq. 2.21 be written as

$$\frac{\partial \gamma}{\partial t} = \underbrace{r\frac{\partial}{\partial r}\left[\nu_T r \frac{\partial}{\partial r}\left(\frac{\gamma}{r^2}\right)\right] + 2\nu_T\left[r\frac{\partial}{\partial r}\left(\frac{\gamma}{r^2}\right)\right]}_{\text{RHS}} \tag{2.24}$$

Transforming the above expression in terms of the similarity variable η is carried out in four steps as shown below:

Step - 1

Obtaining $\partial\gamma/\partial t$ in terms of η starts with

$$\frac{\partial \gamma}{\partial t} = \frac{\partial \gamma}{\partial \eta}\,\frac{\partial \eta}{\partial t} \tag{2.25}$$

Upon differentiating Eq. 2.23 with respect to t results in

$$\frac{\partial \eta}{\partial t} = \frac{r^2}{4\gamma_v}\left(\frac{-1}{t^2}\right) = -\frac{\eta}{t} \tag{2.26}$$

Substituting Eq. 2.26 into Eq. 2.25 gives

$$\frac{\partial \gamma}{\partial t} = \frac{\partial \gamma}{\partial \eta}\left(\frac{-\eta}{t}\right) \tag{2.27}$$

Step - 2

Substitute $\nu_T = \nu$ into the right hand side(RHS) of Eq. 2.24 to get

$$\text{RHS} = r\frac{\partial}{\partial r}\left[\nu r\frac{\partial}{\partial r}\left(\frac{\gamma}{r^2}\right)\right] + 2\nu\left[r\frac{\partial}{\partial r}\left(\frac{\gamma}{r^2}\right)\right] \tag{2.28}$$

The above equation can be written as

$$\text{RHS} = r\frac{\partial}{\partial r}\left(\frac{\nu}{r}\left[\frac{\partial \gamma}{\partial r} - \frac{2\gamma}{r}\right]\right) + \frac{2\nu}{r}\left[\frac{\partial \gamma}{\partial r} - \frac{2\gamma}{r}\right]$$

using the relation from Eq. 2.19. Further simplification results in

$$\text{RHS} = \nu\left[\frac{\partial^2 \gamma}{\partial r^2} - \frac{1}{r}\frac{\partial \gamma}{\partial r}\right] \tag{2.29}$$

To write Eq. 2.29 in terms of η, both $\partial\gamma/\partial r$ and $\partial^2\gamma/\partial r^2$ are required. The first derivative of γ can be obtained using

$$\frac{\partial \gamma}{\partial r} = \frac{\partial \gamma}{\partial \eta}\frac{\partial \eta}{\partial r} \tag{2.30}$$

Differentiating again results in

$$\frac{\partial^2 \gamma}{\partial r^2} = \left(\frac{\partial \eta}{\partial r}\right)^2 \frac{\partial^2 \gamma}{\partial \eta^2} + \left(\frac{\partial^2 \eta}{\partial r^2}\right)\frac{\partial \gamma}{\partial \eta} \tag{2.31}$$

The first and second derivatives of η with respect to r can be obtained by differentiating Eq. 2.23 with respect to r, i.e.,

$$\frac{\partial \eta}{\partial r} = \frac{2r}{4\gamma_v t} = \frac{2\eta}{r} \tag{2.32}$$

and

$$\frac{\partial^2 \eta}{\partial r^2} = \frac{\partial}{\partial r}\left(\frac{2\eta}{r}\right) = \frac{2\eta}{r^2} \tag{2.33}$$

Upon substituting the derivatives of η into Eqs. 2.30 and 2.31, the resulting first and second derivatives of γ are in turn applied in Eq. 2.29 to get

$$\text{RHS} = \nu\left[\frac{\eta}{\gamma_\nu t}\ \frac{\partial^2 \gamma}{\partial \eta^2}\right] \tag{2.34}$$

Step - 3

Let $\nu_T = \kappa^2 r^2 |\sigma|$ based on the assumed value of eddy viscosity. Consequently the RHS of Eq. 2.24 becomes

$$\text{RHS} = r\frac{\partial}{\partial r}\left[\left(\kappa^2 r^2|\sigma|\right) r\frac{\partial}{\partial r}\left(\frac{\gamma}{r^2}\right)\right] + 2\left(\kappa^2 r^2|\sigma|\right)\left[r\frac{\partial}{\partial r}\left(\frac{\gamma}{r^2}\right)\right] \tag{2.35}$$

Because the shear stress inside a one dimensional axisymmetric vortex is given by

$$\sigma = \left(\frac{\partial V_\theta}{\partial r} - \frac{V_\theta}{r}\right) = r\frac{\partial}{\partial r}\left(\frac{\gamma}{r^2}\right) \tag{2.36}$$

then Eq. 2.35 can be rewritten in terms of shear stress as

$$\text{RHS} = r^2\left(|\sigma|\sigma r\frac{\partial}{\partial r}\kappa^2 + \kappa^2 r\frac{\partial}{\partial r}|\sigma|\sigma + 4\kappa^2|\sigma|\sigma\right) \tag{2.37}$$

A similarity transformation of the above expression requires the transformation of σ and its first derivative. Simplifying Eq. 2.36 results in

$$\sigma = \frac{1}{r}\frac{\partial \gamma}{\partial r} - \frac{2\gamma}{r^2} = \frac{2}{r^2}X \tag{2.38}$$

where $X = \eta\partial\gamma/\partial\eta - \gamma$. Substituting Eq. 2.38 into Eq. 2.37 gives

$$\text{RHS} = \frac{4}{r^2}X|X|r\frac{\partial}{\partial r}\kappa^2 + \kappa^2 r^3\frac{\partial}{\partial r}\left(\frac{4}{r^4}|X|X\right) + 4\kappa^2\ \frac{4}{r^2}|X|X \tag{2.39}$$

Expanding the middle term in the right hand side of the above expression and cancelling like terms results in

$$\text{RHS} = \underbrace{\frac{4}{r^2}|X|Xr\frac{\partial}{\partial r}\kappa^2}_{\text{Part1}} + \underbrace{\frac{4\kappa^2}{r}\frac{\partial}{\partial r}|X|X}_{\text{Part2}} \tag{2.40}$$

Notice that the above expression has two parts. A constant value of κ will eliminate the first term and will result in a solution for an Iversen type of eddy viscosity variation. This would mean that the first term in the above expression is the additional term in the new model as a result of having κ as the variable rather than a constant (as assumed by Iversen). Equation 2.40 can be written in terms of similarity variable η as

$$\text{RHS} = \frac{2|X|X}{\gamma_v t}\frac{\partial}{\partial \eta}\kappa^2 + \frac{4\kappa^2}{\gamma_v}\frac{\eta}{t}|X|\frac{\partial^2\gamma}{\partial\eta^2} \tag{2.41}$$

Step - 4

The next step is to combine all the previous three steps to get the circulation distribution in terms of the similarity variable η. This is done by combining Eqs. 2.27, 2.34 and 2.41, which results in

$$\frac{\partial\gamma}{\partial\eta}\left(\frac{-\eta}{t}\right) = \nu\left[\frac{\eta}{\gamma_v t}\frac{\partial^2\gamma}{\partial\eta^2}\right] + \frac{4\kappa^2}{\gamma_v}\frac{\eta}{t}|X|\frac{\partial^2\gamma}{\partial\eta^2} + \frac{2|X|X\eta}{\gamma_v t}\frac{1}{\eta}\frac{\partial}{\partial\eta}\kappa^2 \tag{2.42}$$

Letting $\gamma = \overline{\gamma}\,\gamma_v$ and cancelling like terms, the above expression becomes

$$-\frac{\partial\overline{\gamma}}{\partial\eta} = \left(\frac{\nu}{\gamma_v} + 4\,\kappa^2|\overline{X}|\right)\frac{\partial^2\overline{\gamma}}{\partial\eta^2} + \frac{2|\overline{X}|\overline{X}}{\eta}\frac{\partial}{\partial\eta}\kappa^2 \tag{2.43}$$

where $\overline{X} = X/\gamma_v$. Let $\eta = \overline{\eta}\alpha_I^2$, where the value of α_I is deduced from experimental measurements, then the above equation takes the form

$$-\left(\frac{1}{\alpha_I^2}\right)\frac{\partial\overline{\gamma}}{\partial\overline{\eta}} = \left(\frac{1}{\alpha_I^4}\right)\left[\frac{\nu}{\gamma_v} + 4\kappa^2|\overline{X}|\right]\frac{\partial^2\overline{\gamma}}{\partial\overline{\eta}^2} + \left(\frac{1}{\alpha_I^4}\right)\frac{2|\overline{X}|\overline{X}}{\overline{\eta}}\frac{\partial}{\partial\overline{\eta}}\kappa^2 \tag{2.44}$$

Here, it should be noted that $\overline{X}$ is given by $\left(\overline{\eta}\frac{\partial\overline{\gamma}}{\partial\overline{\eta}} - \overline{\gamma}\right)$. Further simplification results in

$$\underbrace{-\frac{\partial\overline{\gamma}}{\partial\overline{\eta}}}_{\text{Part1}} = \left[\underbrace{\frac{\nu}{\gamma_v}\frac{1}{\alpha_I^2}}_{\text{Part2}} + \underbrace{\frac{4\kappa^2|\overline{X}|}{\alpha_I^2}}_{\text{Part3}}\right]\frac{\partial^2\overline{\gamma}}{\partial\overline{\eta}^2} + \underbrace{\frac{1}{\alpha_I^2}\frac{2|\overline{X}|\overline{X}}{\overline{\eta}}\frac{\partial\kappa^2}{\partial\overline{\eta}}}_{\text{Part4}} \tag{2.45}$$

Here, $\overline{\gamma} = \gamma/\gamma_v$ and $\overline{\eta} = \eta/{\alpha_I}^2$. From Eq. 2.45 it can be noted that the result reduces to a constant viscosity model when the value of κ approaches zero and reduces to Iversen's model when the value of κ approaches α_I. Notice that Eq. 2.45 has four sub-parts:

Part 1: The variation of circulation, $\overline{\gamma}$, with respect to the similarity variable $\overline{\eta}$.

Part 2: The variation in circulation that results from the assumption of constant viscosity.

Part 3: The circulation variation as a result of the assumption of variable eddy viscosity.

Part 4: A result of the "transitional" eddy viscosity variation that is yet to be modeled.

The new model would be complete by defining a function for κ. This is now done by developing a mathematical function that represents the eddy viscosity variation across the vortex from the vortex axis to the outer potential region. This is also based on Richardson number analysis to include the effects of flow rotation on the turbulent structure of the tip vortex.

2.2.7 Modeling of Eddy Viscosity

As explained in the previous sections, the tip vortex can be assumed to be made of three regions moving outward from the core: an inner laminar region, a transitional region, followed by an outer turbulent region. Therefore, the variation of κ should represent the variation of the eddy viscosity over all of these three regions. It can be observed from Fig. 2.17 that in the laminar region (i.e., until a particular distance from the vortex core where the Richardson's number falls below the threshold value) the vortex cannot develop or sustain any turbulence. This will result in essentially zero eddy viscosity. The developed function for κ should also be zero until that radial distance is reached in this region. As the radial distance increases, the vortex flow becomes transitional, and finally the flow becomes completely turbulent at large distances. This would mean that the proposed function of κ should also start increasing and reach a value equivalent to that of a completely turbulent vortex at large radial distances.

Intermittency Function

To satisfy all the above mentioned conditions, a new value of κ is defined here as

$$\kappa = \alpha_I \sqrt{\text{VIF}} \tag{2.46}$$

where α_I is Iversen's constant and VIF is called a "vortex intermittency function" as given by

$$\text{VIF} = \frac{1}{2}\left[1 + \text{erf}\left(b\left[\sqrt{\frac{\overline{\eta}}{\overline{\eta}_1}} - \overline{\eta_a}\right]\right)\right] \tag{2.47}$$

where $\overline{\eta}_1$ represents the value of the similarity variable at the point where the peak swirl velocity is maximum, and b and $\overline{\eta}_a$ are empirical constants. The coefficient b

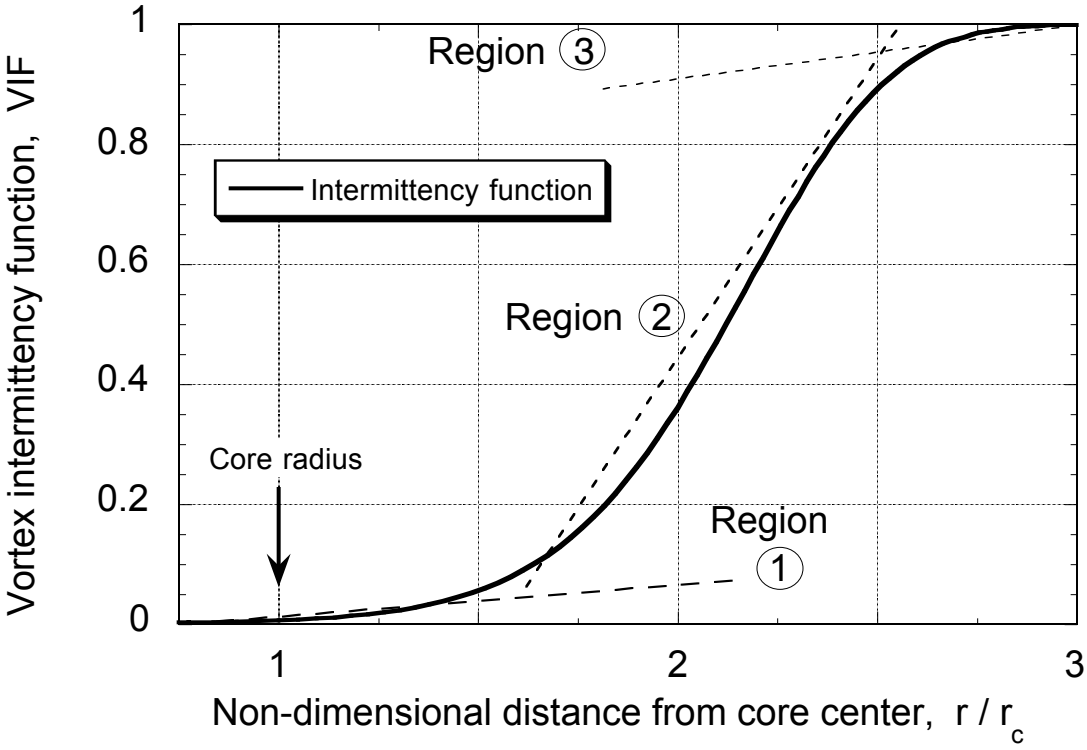

Figure 2.18: Eddy viscosity intermittency function across the vortex: (1) Laminar region, (2) Transitional region, (3) Turbulent region.

represents the rate at which the transition from laminar to turbulent flow occurs, and $\overline{\eta}_a$ represents the value at which the value of VIF is 0.5.

A representative variation of the VIF with respect to non-dimensional radial distance r/r_c and η/η_1 is shown in Figs. 2.18 and 2.19, respectively. A value of VIF $= 0$ corresponds to $\kappa = 0$ and VIF $= 1$ corresponds to $\kappa = \alpha_I$, i.e., values of κ that would result in a completely laminar and turbulent values for eddy viscosity, respectively.

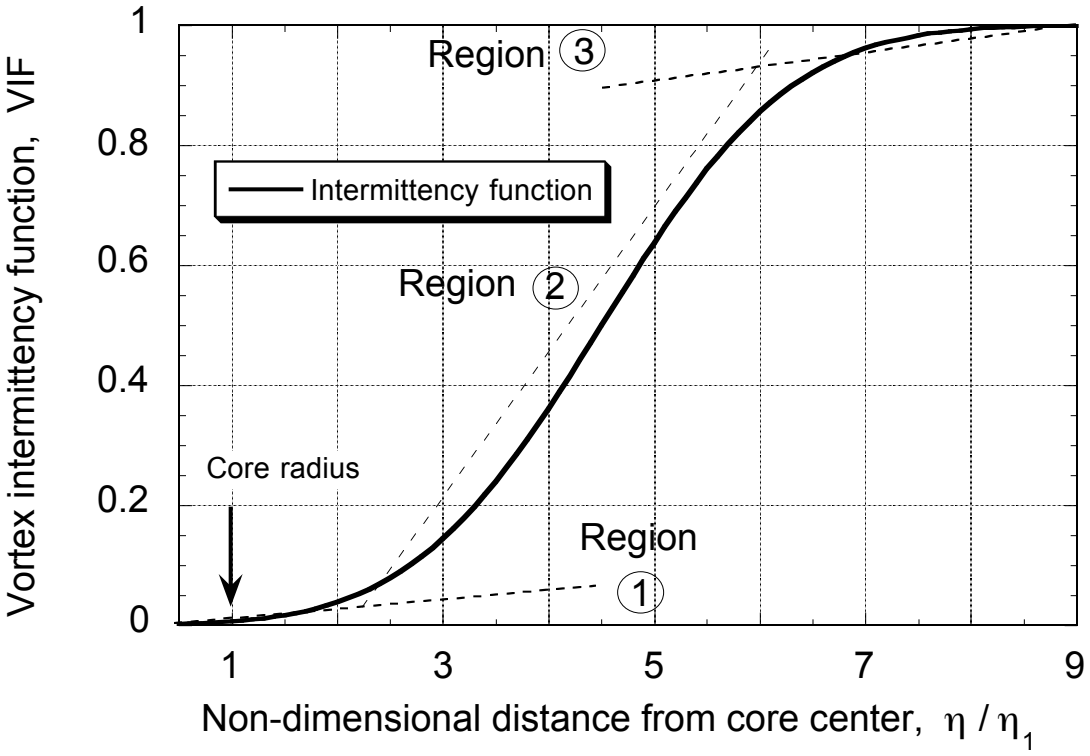

Figure 2.19: Eddy viscosity intermittency function across the vortex in terms of similarity variable: (1) Laminar region, (2) Transitional region, (3) Turbulent region.

Analogy with Boundary Layer Theory

The new expression for the VIF has been derived in a manner analogous to the intermittency function used in boundary layer theory (e.g., Refs. 107, 108). Near the wall in a boundary layer (viscous sub-layer) the turbulent fluctuations are damped by the presence of a solid surface. Here, the mean velocity is known to vary linearly with the normal distance. Also, the stress is usually assumed constant and is equal to the value of stress at its surface. Similarly, in a vortex flow the turbulent fluctuations are suppressed by flow rotation effects (stratification) and, therefore, the eddy viscosity that results from turbulence is negligible. Also, the tangential inertia of this "eye" or "equivalent viscous sub-layer" of the vortex (represented by Region 1 in Fig. 2.18 where the VIF ≈ 0) is very high when compared with the Reynolds stress because of the high tangential velocity gradients. Therefore, the hypothesis made by Hoffman et al. [64] that the circulation distribution varies logarithmically with radial distance is not valid inside this region.

In the new model, the VIF forces the eddy viscosity to be zero in Region 1, resulting in laminar flow near the vortex core axis, a result consistent with experiments. Furthermore, it should be noticed that the mean swirl velocity increases linearly with distance (solid body rotation), similar to that of the boundary layer. By writing the expression for total viscosity as

$$\nu_T = \nu + \kappa^2 \left(r^2 \left| \frac{\partial}{\partial r} \left(\frac{\Gamma}{r^2} \right) \right| \right) = \nu + \text{VIF}\ {\alpha_{\text{new}}}^2 \left(r^2 \left| \frac{\partial}{\partial r} \left(\frac{\Gamma}{r^2} \right) \right| \right) \tag{2.48}$$

it is apparent from Fig. 2.18 that the VIF (and hence the eddy viscosity) is zero near the center of the vortex. Here, α_{new} is a new empirical constant, as yet to be determined. For a value of $\alpha_{\text{new}} = \alpha_I$ and $\text{V}IF = 1$, the expression for total viscosity reduces to an Iversen-type eddy viscosity model. However, the constant α_I used by Iversen for

his predictions was determined from measurements that were not corrected for many experimental issues, such as the problem of wandering which has been alluded to previously. The procedure to determine the value of α_{new} is explained in the next section.

Region 2 represents a transition region where the flow transitions from a laminar to a turbulent flow. Here, the tangential inertia is much smaller than the Reynolds stress because of the low velocity gradient. The Richardson number in this region falls below the threshold value ($Ri = {Re_{\text{v}}}^{1/4}$) and any turbulence present cannot be suppressed by stratification – see Fig. 2.17. As a result both types of shear: viscous (molecular) shear and turbulent (eddy) shear are equally important here. Region 3 represents the potential flow regime (analogous to the outer region of the boundary layer), where the circulation remains constant. Here, the eddy viscosity plays a significant role and is more dominant than the effects of molecular viscosity. The variation of the eddy viscosity in all the aforementioned three regions is modeled in a continuous manner using the vortex intermittency function: an inner laminar region when the value of VIF is approximately zero, a transition region when $0 < \text{VIF} < 1$, and then turbulent region when VIF approaches unity.

Substituting the expression for the VIF from Eq. 2.47 into Eq. 2.45 (after replacing α_I by α_{new}) results in

$$-\frac{\partial\overline{\gamma}}{\partial\overline{\eta}} = \left[\frac{\nu}{\gamma_\nu}\frac{1}{{\alpha_{\text{new}}}^2} + 4\text{VIF}^2\ |\overline{\text{X}}|\right]\frac{\partial^2\overline{\gamma}}{\partial\overline{\eta}^2} + \frac{2|\overline{X}|\overline{X}}{\overline{\eta}}\frac{\partial}{\partial\overline{\eta}}\text{VIF} \tag{2.49}$$

Equation 2.49 requires the first derivative of the VIF with respect to $\overline{\eta}$, i.e.,

$$\begin{aligned}\frac{\partial(\text{VIF})}{\partial\overline{\eta}} &= \frac{1}{2}\frac{\partial}{\partial\overline{\eta}}\left[1+\text{erf}\left(\text{b}\left[\sqrt{\frac{\overline{\eta}}{\overline{\eta}_1}}-\overline{\eta_{\text{a}}}\right]\right)\right] \\ &= \frac{1}{\sqrt{\pi}}\exp\left(-b^2\left[\sqrt{\frac{\overline{\eta}}{\overline{\eta}_1}}-\overline{\eta_a}\right]^2\right)\frac{b}{2}\frac{1}{\sqrt{\overline{\eta}\overline{\eta}_1}}\end{aligned}$$

Substituting the above expression into Eq. 2.49 gives

$$-\frac{\partial\overline{\gamma}}{\partial\overline{\eta}} = \left[\frac{\nu}{\gamma_v}\frac{1}{{\alpha_{\text{new}}}^2} + 4\ \text{VIF}^2|\overline{\text{X}}|\right]\frac{\partial^2\overline{\gamma}}{\partial\overline{\eta}^2} + \left[\frac{b}{2\sqrt{\overline{\eta}\overline{\eta}_1}}\right]\left[\frac{1}{\sqrt{\pi}}\frac{2|\overline{X}|\overline{X}}{\overline{\eta}}\right]\exp\left(-b^2\left[\sqrt{\frac{\overline{\eta}}{\overline{\eta}_1}} - \overline{\eta_a}\right]^2\right] \tag{2.50}$$

Solving this expression numerically using a Runge-Kutta scheme (see next) provides the required distribution of circulation for a given vortex Reynolds number.

2.2.8 Solution Procedure

A third-order Runge-Kutta scheme was used to determine the solution of Eq. 2.50. Equation 2.49 can be written as

$$\begin{aligned}\frac{\partial\overline{\gamma}}{\partial\overline{\eta}} &= -\left[\frac{2\pi}{\text{Re}_\text{v}}\frac{1}{{\alpha_{\text{new}}}^2} + 4\text{VIF}^2\ |\overline{\text{X}}|\right]\frac{\partial^2\overline{\gamma}}{\partial\overline{\eta}^2} + \frac{2|\overline{X}|\overline{X}}{\overline{\eta}}\frac{\partial}{\partial\overline{\eta}}\text{VIF} \\ &= F\left(\eta,\gamma,\frac{\partial\gamma}{\partial\eta}\right)\end{aligned} \tag{2.51}$$

The integration was carried out by stepping out from the center with the step size h, and the solution is updated in space by using

$$\gamma(\eta+h) = \gamma(\eta) + \frac{a_1+4a_2+a3}{6} \tag{2.52}$$

$$\frac{\partial\gamma}{\partial\eta}(\eta+h) = \frac{\partial\gamma}{\partial\eta}(\eta) + \frac{b_1+4b_2+b_3}{6} \tag{2.53}$$

where

$$a_1 = h\frac{\partial\gamma}{\partial\eta},\ b1 = hF\left(\eta,\gamma,\frac{\partial\gamma}{\partial\eta}\right) \tag{2.54}$$

$$a_2 = h\left(\frac{\partial\gamma}{\partial\eta}+\frac{b1}{2}\right),\ b_2 = F\left(\eta+\frac{h}{2},\gamma+\frac{a_1}{2},\frac{\partial\gamma}{\partial\eta}+\frac{b_1}{2}\right) \tag{2.55}$$

$$a_3 = h\left(\frac{\partial\gamma}{\partial\eta}+2b_2-b_1\right),\ b_3 = F\left(\eta+h,\gamma+2a_2-a_1,\frac{\partial\gamma}{\partial\eta}+2b_2-b1\right) \tag{2.56}$$

A shooting technique was applied with the initial guess for the gradient $\frac{\partial \gamma}{\partial \eta}(0)$ that was later adjusted using

$$\frac{\partial \gamma}{\partial \eta}(0) = \frac{\partial \gamma}{\partial \eta}(0) + \frac{\mathrm{R}e_v}{10^7}\Big(1 - \gamma(\infty)\Big) \tag{2.57}$$

The boundary condition in the far field was assigned to be $\gamma(\infty) = 1$. The final solution is a vortex Reynolds number dependent circulation distribution (also including the flow rotation or Richardson number effects) as a function of normalized distance from the vortex core center, i.e.,

$$\frac{\Gamma}{\Gamma_{\mathrm{v}}}\Big(\frac{r}{r_c}\Big) = \gamma\Big(\frac{\eta}{\eta_c}, Re, Ri\Big) \tag{2.58}$$

where

$$\frac{\eta}{\eta_c} = \sqrt{\frac{r}{r_c}} \tag{2.59}$$

The effects of *Ri* appear in the expression for the VIF, which models the variation of eddy viscosity across the tip vortex.

2.2.9 Determination of Empirical Constants

It should be noted that Eq. 2.50 has three empirical constants, α_{new}, b, $\overline{\eta}_a$. Iversen determined the value of his α_I from various measurements that were at large equivalent downstream distances. The reason for doing this was to ensure a more uniform turbulent decay of the trailing vortices. Also, it should be kept in mind that the vortex measurements used by Iversen were performed with fixed-wings, including results at very high vortex Reynolds numbers. Even though this model predicted a higher core growth than the laminar Lamb–Oseen model, the distribution of swirl velocity, V_θ, predicted by the model did not correlate well with experimental measurements [e.g., Refs. 7, 8, 19, 38].

An approach similar to that of Iversen is taken using new measurements to determine a value for α_I. For the purposes of distinction, let the new value be called α_{new}. Following Iversen let

$$\frac{V_\theta c}{\gamma_v} = \left(\frac{c}{r}\right)\overline{\gamma}\left(\eta, \frac{\nu}{\gamma_v}\right) \tag{2.60}$$

At the core radius, $V_\theta = V_1$ and $r = r_c$. Therefore, Eq. 2.60 at the core radius is given by

$$\frac{V_1 c}{\gamma_v} = \left(\frac{c}{r_c}\right)\ \overline{\gamma}\left(\frac{r_c^2}{4\gamma_v t}, \frac{\nu}{\gamma_v}\right) \tag{2.61}$$

But

$$\frac{r_c^2}{4\gamma_v t} = \frac{r_c^2}{4\gamma_v}\ \frac{\Omega}{\psi} = \eta_1 = \text{constant}$$

This would result in

$$\frac{c}{r_c} = \left(\frac{c^2\Omega}{4\eta_1\gamma_v\psi}\right)^{1/2}$$

Upon substituting this in Eq. 2.61 gives

$$\frac{V_1 c}{\gamma_v} = \left[\left(\frac{c}{\psi}\right)\left(\frac{\Omega c}{\gamma_v}\right)\left(\frac{1}{4\eta_1}\right)\right]^{1/2}\overline{\gamma}\left(\eta_1, \frac{\nu}{\gamma_v}\right) \tag{2.62}$$

or

$$\underbrace{\frac{V_1 c}{\Gamma_v}}_{A}\left[\underbrace{\frac{\psi}{c}\left(\frac{\Gamma_v}{\Omega c}\right)}_{B}\right]^{1/2} = C_0\ g\left(\frac{\Gamma_v}{\nu}\right) \tag{2.63}$$

where Part A in Eq. 2.63 represents the vortex velocity scaling parameter, Part B represents the distance scaling parameter that is called an "equivalent downstream distance." The coefficient C_0 is a constant as yet to be determined, and the coefficient g is the core circulation function.

Table 2.1 shows the average values of the quantity on the left-hand side of Eq. 2.63 versus equivalent downstream distances for a set of rotor experiments. Much care was taken in choosing a suitable set of experiments for determining the empirical constant.

Experiments	Equivalent downstream distance $(\psi/c)(\Gamma_v/\Omega\, c)$	LHS of Eq. 2.63 $(V_1 c/\Gamma_v)\,[\psi/c\ \ (\Gamma_v/\Omega c)]^{1/2}$
Martin & Leishman, 2000 [8]	0.5–8.9	2.197
Bhagwat & Leishman, 1998 [76]	0.19–10	1.9362
Mahalingam et al., 1998 [18]	0.41–3.48	1.4386
McAlister, 1996 [19]	0.06–0.4	0.9957
McAlister, 2003 [7]	0.02–0.6	0.741
Ramasamy & Leishman, 2002 [38]	0.4–28.6	2.5264

Table 2.1: Values of equivalent peak swirl velocity from various rotorcraft experiments.

Upon looking at all the previous work, most of the measurements are too sparse and too incomplete. To develop a vortex model, or validate an existing vortex model for rotor analysis, there is a need for a measurement that satisfies all the following conditions:

1. Measurements should be from rotor (not fixed-wing) experiments.

2. Measurement should be available at older wake ages.

3. Measurements must be corrected for aperiodic flow effects.

4. Measurements must be strain free or corrected for strain effects.

5. Measurements must be made at high spatial and temporal resolution to provide high confidence in the final results.

6. Measurements should be as free as possible of interference effects from blades and vortices emanating from other blades.

The average value of all of the selected data (the product of Parts *A* and *B* from Eq. 2.63) was found to be 1.641. By re-writing Eq. 2.48 in terms of vortex Reynolds number as

$$\nu_T = \frac{\Gamma_v}{Re_v} + \text{VIF}\ {\alpha_{\text{new}}}^2 \left(r^2 \left| \frac{\partial}{\partial r} \left(\frac{\Gamma}{r^2} \right) \right| \right) \tag{2.64}$$

it is apparent that the total viscosity will remain constant at very high Reynolds number. This will result in the core circulation function g (which is a function of vortex Reynolds number) and hence, the peak swirl velocity ($\overline{\gamma}/\overline{\eta}^{1/2}$) will asymptote to a constant value at higher vortex Reynolds numbers. This implies that the value of C_0 is 1.641 if the asymptotic value of g is assumed to approach unity at large vortex Reynolds numbers.

The value of α_{new} was determined, however, by using the asymptotic value of $\overline{\gamma}/\overline{\eta}^{1/2}$ ($= 0.539$) obtained from Iversen's model (as shown in Fig. 2.20) so that the new model will approach Iversen's model when the VIF approaches the value of unity. By writing Eq. 2.63 as

$$\frac{Vc}{\Gamma_v} \left[\left(\frac{\Psi}{c} \right) \left(\frac{\Gamma_v}{\Omega c} \right) \right]^{1/2} = \left(\frac{\overline{\gamma}}{\overline{\eta}^{1/2}} \right) \frac{1}{2\alpha_{\text{new}} (2\pi)^{1/2}} \tag{2.65}$$

then α_{new} can be written as

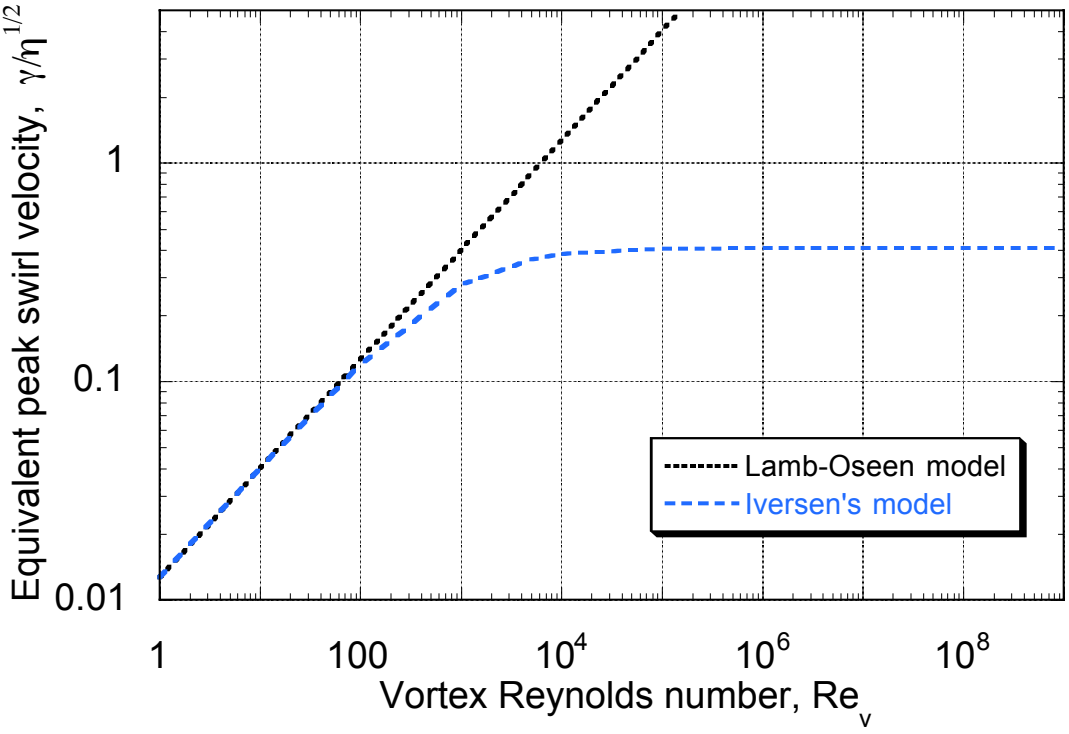

Figure 2.20: Variation of peak swirl velocity versus Reynolds number for Lamb–Oseen and Iversen models.

$$\alpha_{new} = \left(\frac{\overline{\gamma}}{\overline{\eta}^{1/2}} \right)_{\text{Iversen}} \frac{\sqrt{2}}{4\sqrt{\pi}(1.641)} = 0.0655 \tag{2.66}$$

Because this value is determined by averaging various measurements that were performed over a wide range of vortex Reynolds numbers, the velocity profile corresponding to the solution of Eq. 2.50 for any vortex Reynolds number can now be predicted.

Chapter 3

Results and Discussion

In Chapter 2, an experimental methodology for undertaking vortex flow measurements in a known strain field was described. This chapter also included a description of a theoretical approach towards developing a new tip vortex model. This new model takes into account the effects of flow rotation on turbulence as well as the effects of vortex Reynolds number on tip vortex evolution. In the present chapter, the experimental results from the vortex measurements are presented. Because the presence of a solid boundary stretches the vortex filaments, the results help understand the effects of a strain field on the otherwise diffusion dominated tip vortex flow. These measurements were then used to help develop an engineering model for the effects of vortex stretching on the evolution of tip vortices. The second part of this chapter shows the circulation, peak swirl velocity, and core growth predicted by the new generalized vortex model that includes the effects of vortex Reynolds number. Experimental results from several sources were used to validate the predictions. Finally, a comprehensive core growth model for the tip vortices was developed by combining the strain model with a generalized model of vortex diffusion.

3.1 Experimental Results

In this section, the experimental results are presented starting with flow visualization. These results help in determining the spatial location of the tip vortices. The spatial locations were later used for estimating the strain exerted on the vortex filaments. This is followed by the results from the high resolution LDV measurements. These results were used to determine the swirl velocity profile, the viscous core radius and the peak swirl velocity at different wake ages.

3.1.1 Wake Displacements and Strains

Determining the spatial locations of the tip vortices accurately is necessary to understand the overall physics of the rotor flow field. This is especially true in the current experiment because the vortex strain rates were estimated based on the measured spatial locations of the tip vortices relative to the blade at various wake ages.

Determination of the wake geometry was possible in this experiment by acquiring flow visualization images of the tip vortices at several wake ages using the strobed laser sheet technique. Representative images that were taken at different wake ages are shown in Fig. 3.1. To make these images, the volume and distribution of seeding were judiciously adjusted so that the cores of the vortices appeared as distinct "voids" of seed. The center of the seed void was assumed to be the center of the vortex core. While not strictly correct, this definition if applied consistently allows the displacements to be obtained with good levels of confidence. At each wake age, a minimum of 300 separate images were taken, from which the spatial average locations of the vortex relative to the rotor were quantified by using a calibration grid. This is a robust, but a tedious procedure. However, the process enables the acquisition of the statistics

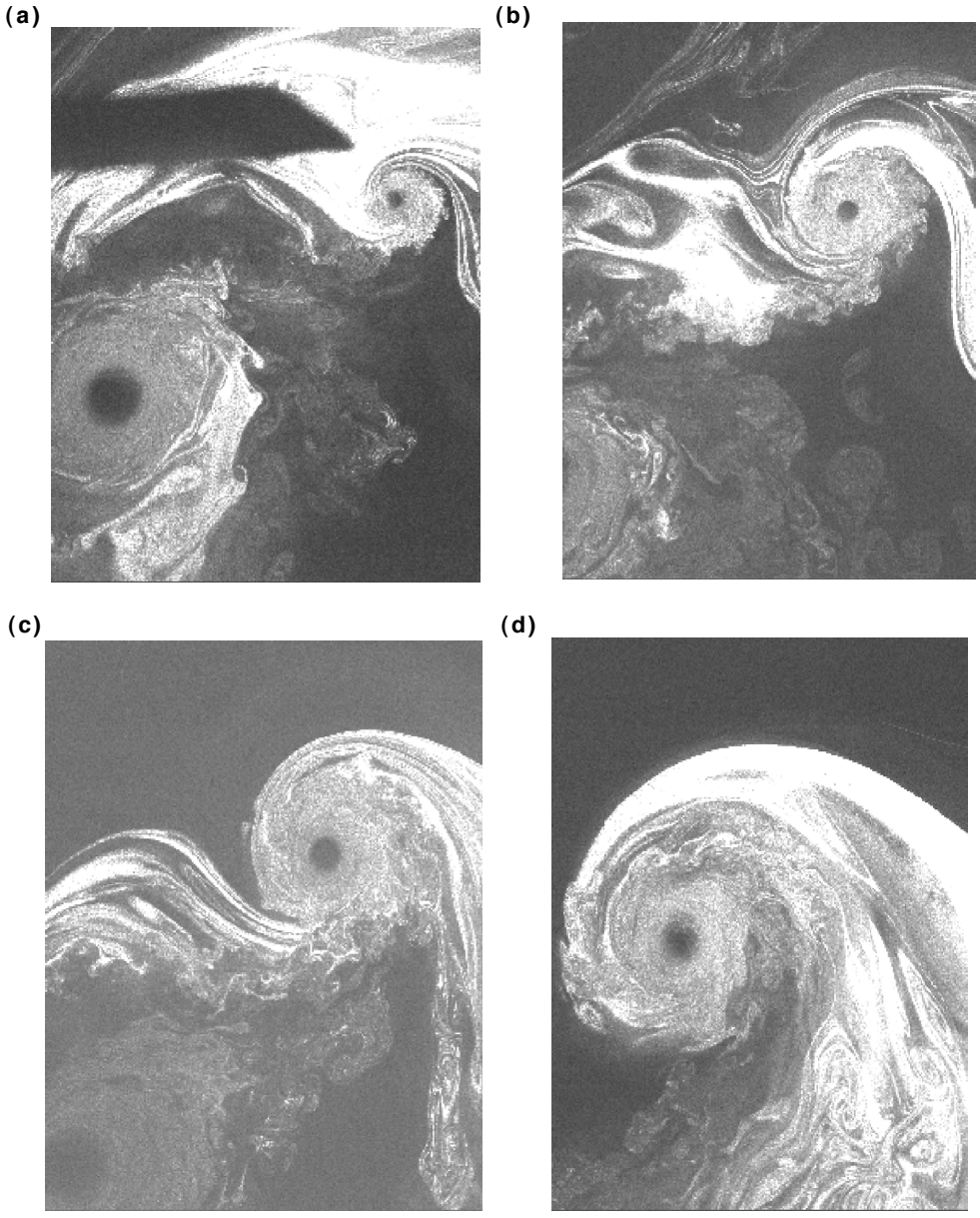

Figure 3.1: Flow visualization images of a rotor blade tip vortex at (a) $\zeta = 15^\circ$, (b) $\zeta = 60^\circ$, (c) $\zeta = 90^\circ$, (d) $\zeta = 270^\circ$.

of the small aperiodic deviations of the vortex positions from their mean locations. These statistics were used to correct the LDV velocity measurements for aperiodicity effects (see Appendix A).

Figures 3.2 and 3.3 show the axial and radial locations of the tip vortices, both in the presence of the solid boundary as well as in the baseline condition when the rotor wake developed under free conditions. Even though initially there was a small difference in the wake geometry between the two cases, it is apparent that the tip vortices move inboard radially from the blade tip and axially downward at the early wake ages in both the cases. When the tip vortices approached the ground plane, however, they moved radially outward and became almost parallel to the ground plane at older wake ages. It can be deduced from Fig. 3.4, which shows the convection velocities of the tip vortices at various wake ages, that the axial convection velocities are nominally constant until the first blade passage at $\zeta = 360^{\circ}$. However, they encounter much higher overall velocities when closer to the ground plane. Clearly, the axial (slipstream) velocity component of the tip vortices must asymptote to zero as the tip vortices approach the ground plane.

After the spatial locations of the tip vortices were measured, the average strain rates acting on the vortices was calculated. This was done by fitting a series of curves to the displacements. Landgrebe's prescribed wake model [28] was used for fitting the spatial locations in the base line case, whereas a polynomial was used for the ground plane case. This was followed by differentiating the curve numerically by means of finite differences. From the locations of the vortices at various wake ages, the length of the vortex filament was determined by its location in space defined by the position vectors of two adjacent locations at $\vec{r}_l$ and $\vec{r_{l-1}}$. If the filament is assumed to be a infinitesimal straight-line segment, the length of the filament is given by $|\vec{l}| =$

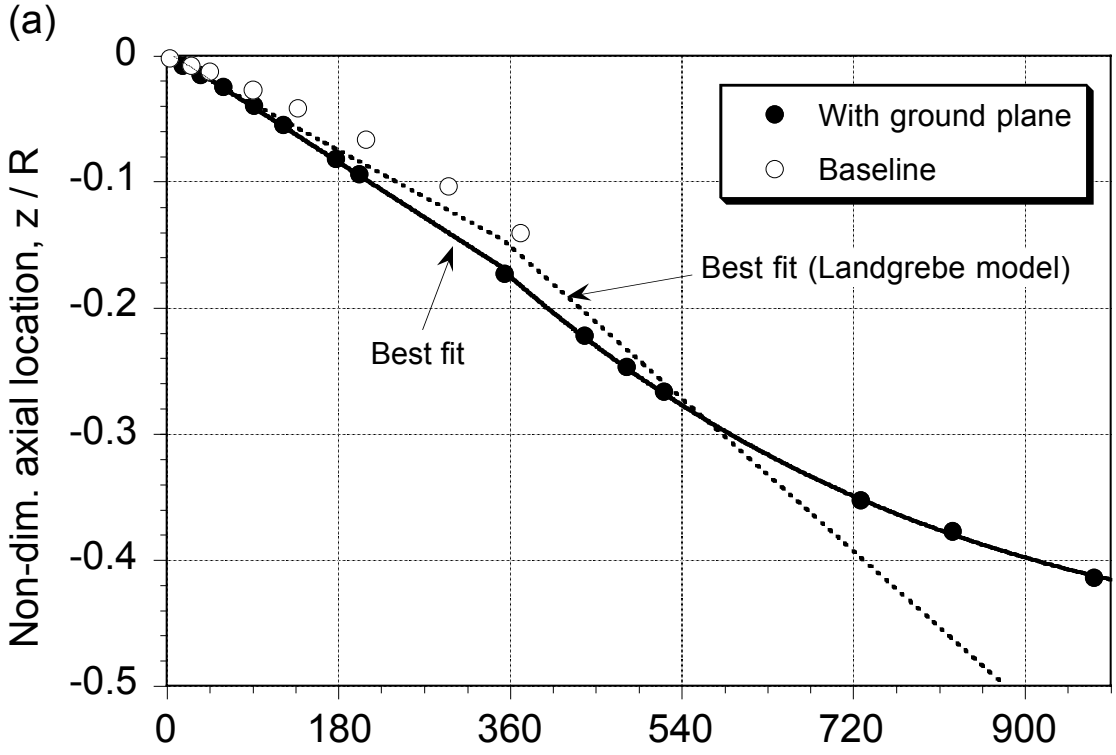

Figure 3.2: Results showing the axial locations of the tip vortices relative to the rotor tip-path-plane.

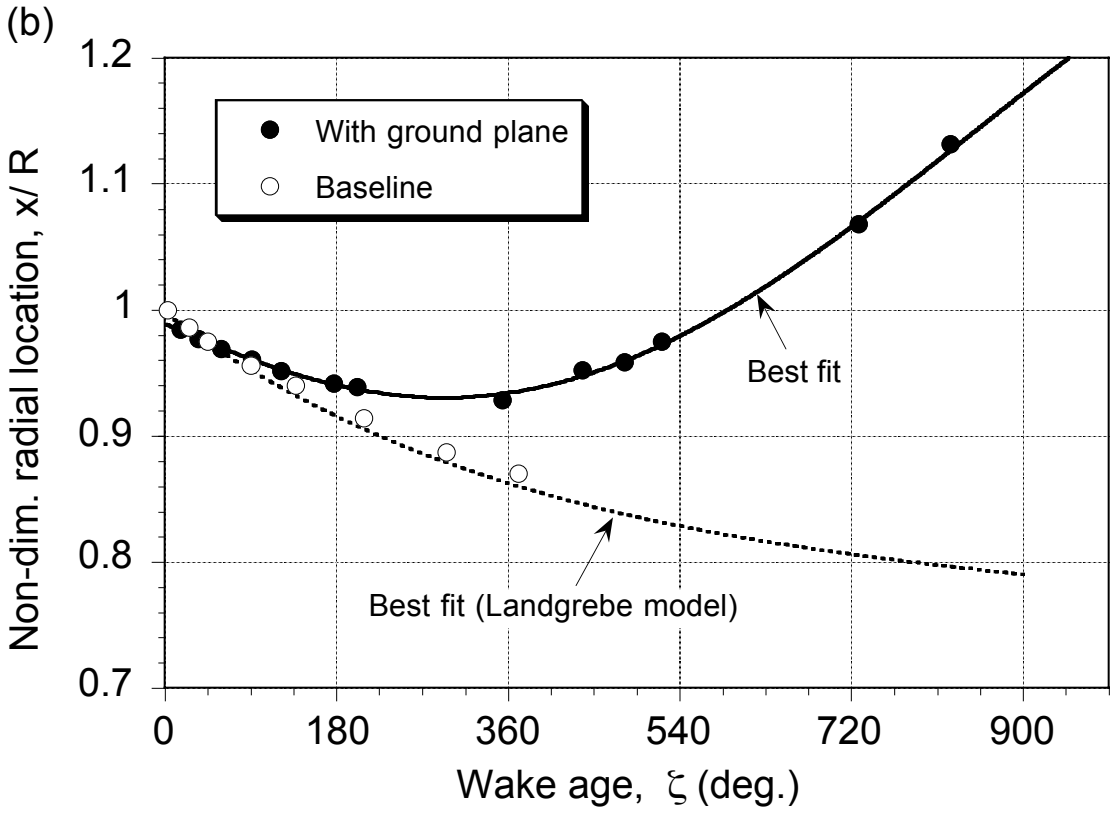

Figure 3.3: Results showing the radial locations of the tip vortices relative to the rotor tip-path-plane.

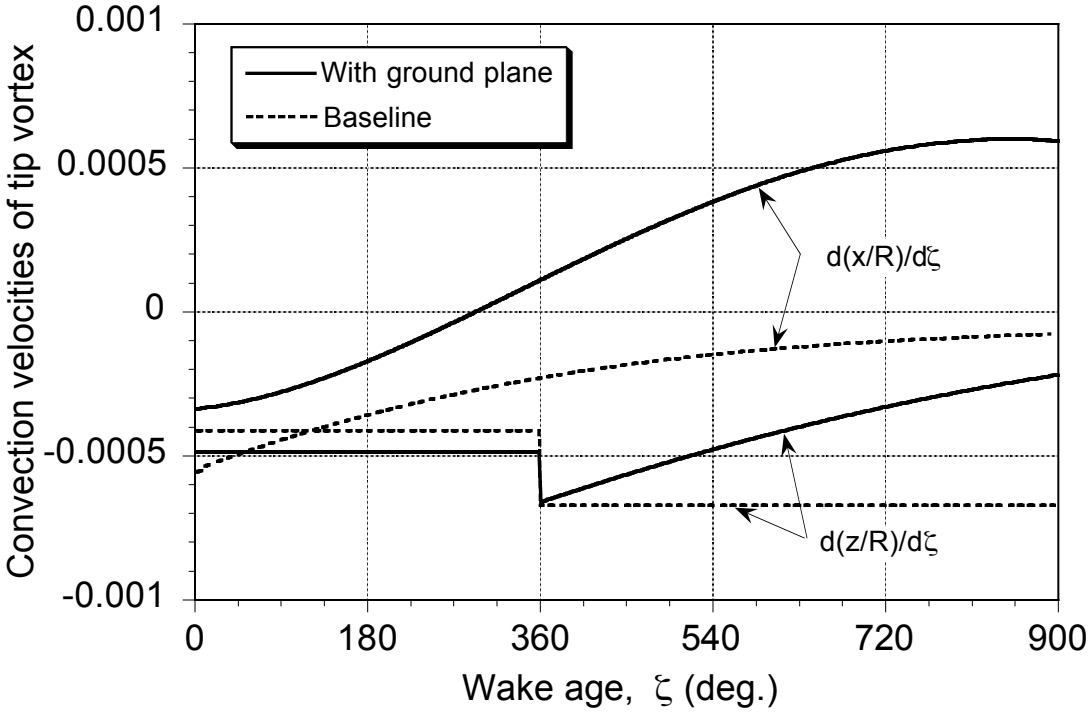

Figure 3.4: Estimated components of the tip vortex convection velocities compared to the baseline free-air condition.

$|\vec{r_l} - \vec{r_{l-1}}|$, as shown in Fig. 3.5. Therefore, the rate of change of the length of the filament as it convects through the velocity field is given by

$$\frac{d\vec{l}}{dt} = \frac{d(\mathbf{r}_l - \mathbf{r}_{l-1})}{dt} \tag{3.1}$$

or

$$\frac{d\varepsilon}{dt} = \frac{dl}{dt}\left(\frac{1}{l}\right) \tag{3.2}$$

This implies that the strain, ε, is

$$\varepsilon = \left(\frac{d\varepsilon}{dt}\right)\Delta t = \left(\frac{d\varepsilon}{d\zeta}\right)\Delta\zeta \tag{3.3}$$

where $\varepsilon = \Delta l/l$ is the strain imposed on the filament over the time interval, Δt.

Results documenting the estimated strains are shown in Fig. 3.6. Several observations can be made from this plot. In the baseline case it can be observed that the strain is negative at early wake ages. This is because the tip vortices move radially inward resulting in a contraction (negative strain) of the vortex filaments. However, the filament strain is seen to be negligible at older wake ages. This is expected, because the results in Fig. 3.4 have shown that the convection rates of the tip vortices in the baseline case begin to asymptote to a constant value and the radial velocities approach zero after the initial wake contraction.

The amount of strain or "stretching" produced on the tip vortex as it develops near the ground plane is much larger than that obtained in free air conditions. When the tip vortices approach the ground plane, the strain on the tip vortex is initially slightly negative at early wake ages (as a result of radial contraction) similar to that found in the baseline case. Thereafter, the strain becomes quickly positive as the vortex filaments stretch radially outward. These large values of strain are capable of producing substantial difference in the structure and evolution of the tip vortices.

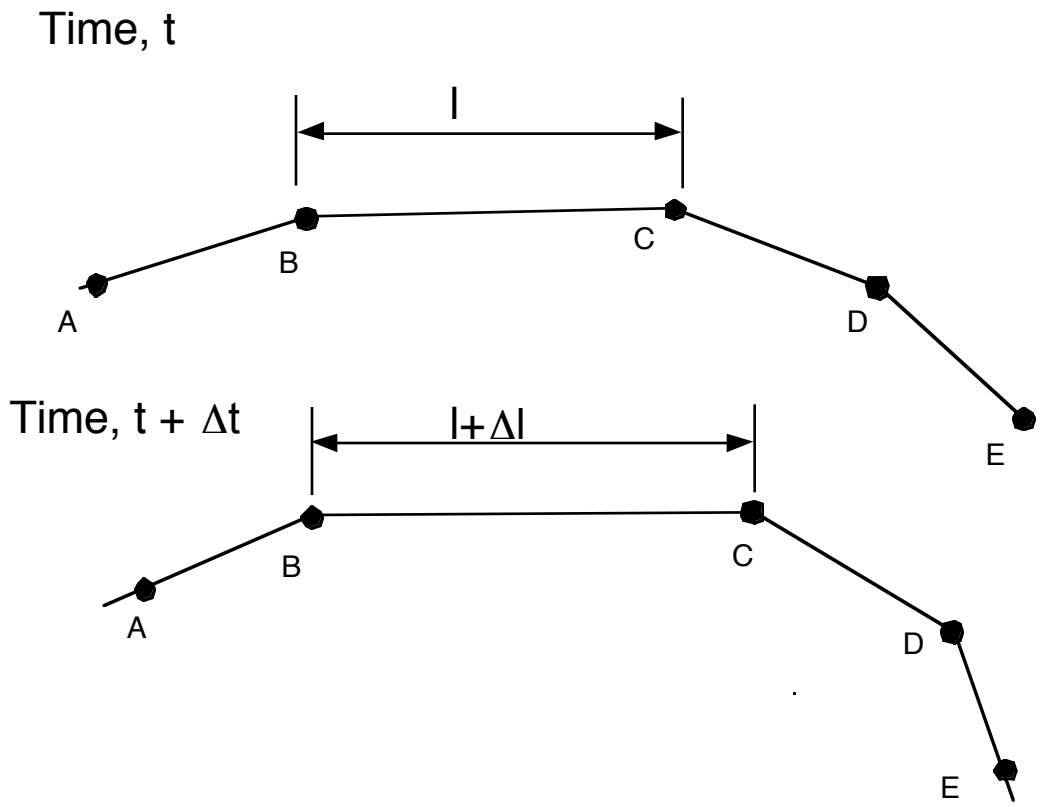

Figure 3.5: Schematic explaining the procedure to calculate strain calculation from the spatial location of the tip vortices.

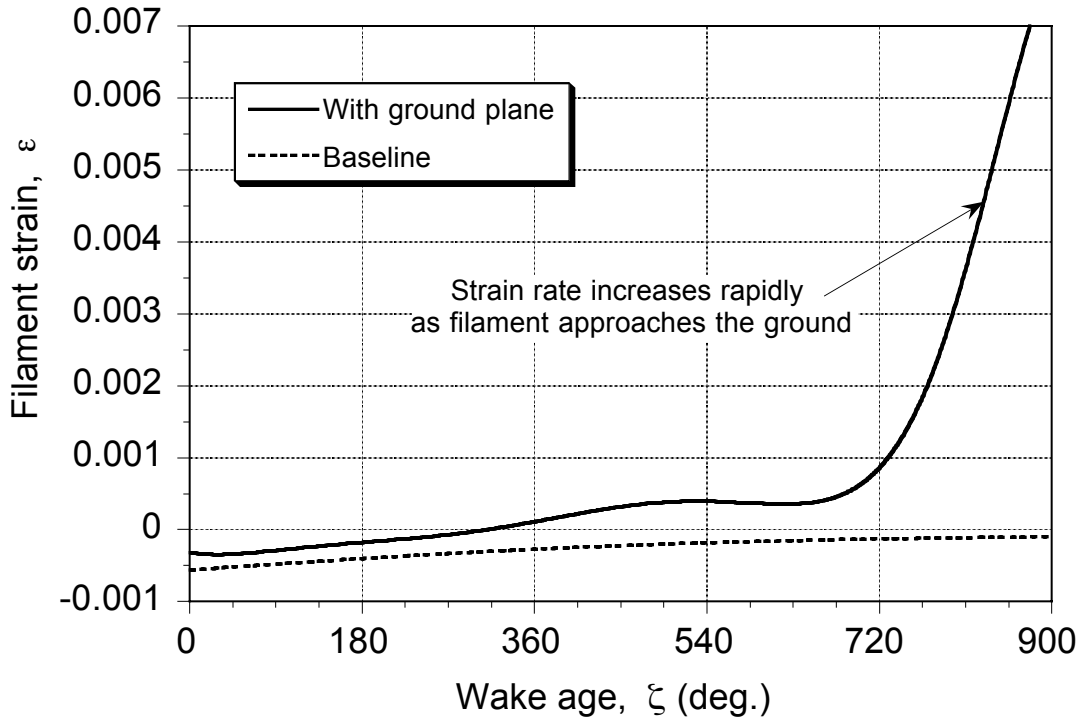

Figure 3.6: Estimated strain experienced by the vortex filaments as they approached the ground plane compared to the baseline free-air condition.

3.1.2 Velocity Field Measurements

Phase-resolved LDV measurements of the vortex properties were acquired using a 3-component LDV system. This was done by making a radial traverse across the vortex core at various planes in the wake between the rotor and the ground plane. Because the ground plane for this experiment was kept at 0.5R (8 inches) from the tip path plane, the measurements were made to $0.4R$ from the TPP. By estimating the blade azimuth at which the vortex core was centered on the grid, the instantaneous velocity field could be measured. The vortex properties could then be studied as a function of wake age. Wherever possible, the results measured with the ground plane were compared to the baseline measurements at the same wake age. The ability to measure results at older wake ages ($\zeta > 360^\circ$) was considered a unique feature of the preset work relative to what has been previously possible. This is, in part, because of the precise spatial alignment of the LDV system, which gives high quality data with good data rates. Also, the process of stretching the vortices intensified their vorticity, preserving their structure to older wake ages.

Swirl Velocities

Figures 3.7 through 3.10 shows a series of tangential (swirl) velocity profiles measured across each radial grid as the convecting vortices intersected the measurement grid in a cross flow plane (see Fig. 2.1). These profiles are presented in terms of the non-dimensional distance with respect to a coordinate system centered at the vortex axis, and the velocity is non-dimensionalized with respect to the rotor tip speed, ΩR. In other words, all the data is placed in a frame of reference moving along with the vortex. Also, all the data was corrected for the measured effects of aperiodicity (see Appendix A).

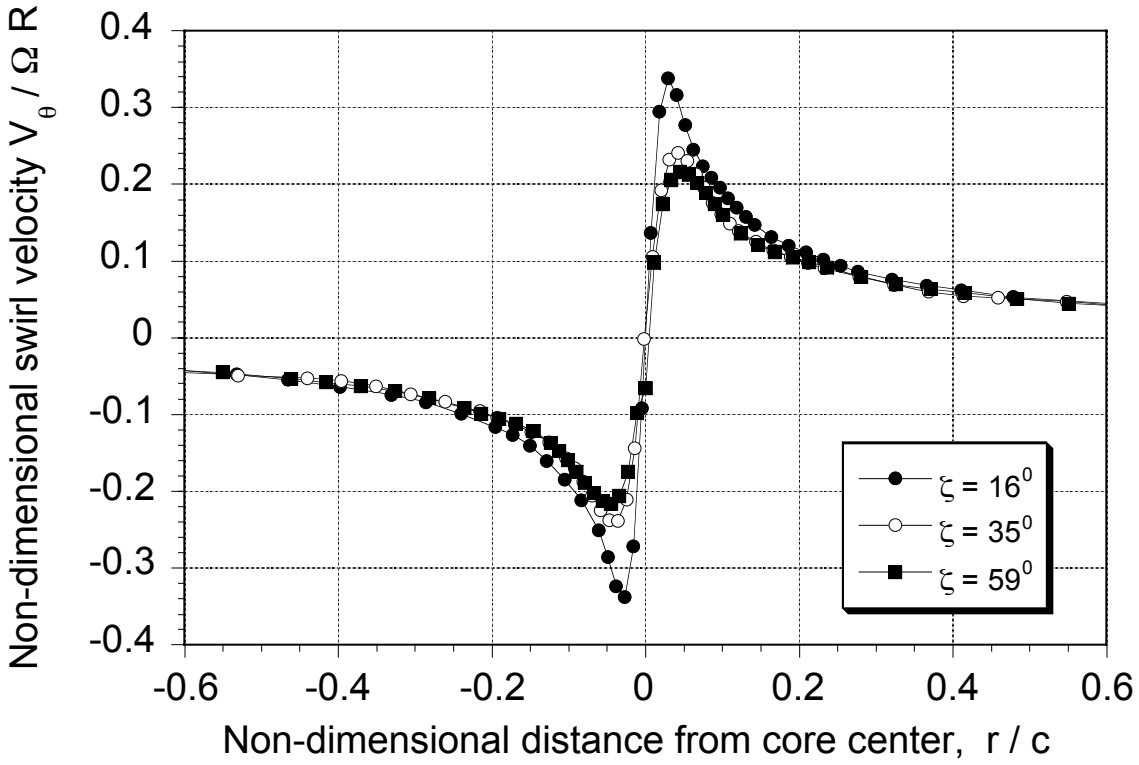

Figure 3.7: Swirl velocity profiles in the tip vortex at very early wake ages ($\zeta = 0^\circ$ to $\zeta = 60^\circ$).

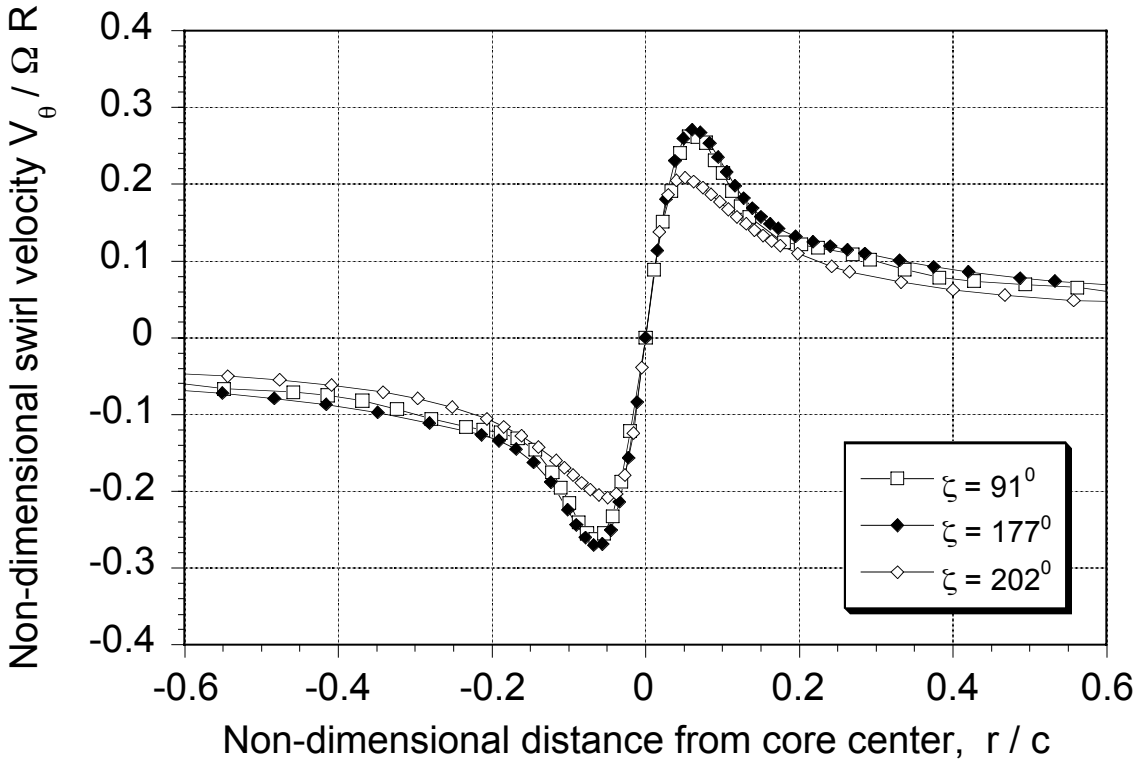

Figure 3.8: Swirl velocity profiles in the tip vortex within one rotor revolution ($\zeta < 360°$).

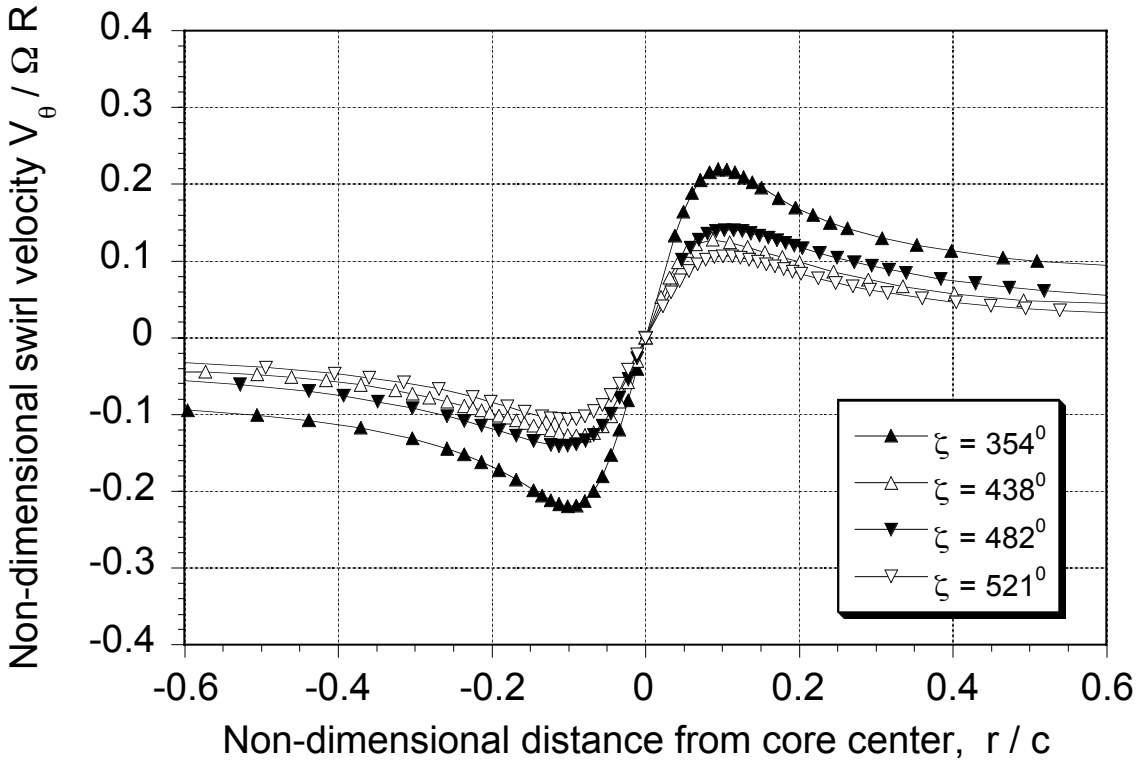

Figure 3.9: Swirl velocity profiles in the tip vortex at older wake ages (between $\zeta = 350°$ to $\zeta = 550°$), showing the vortex still diffuses under the action of viscosity.

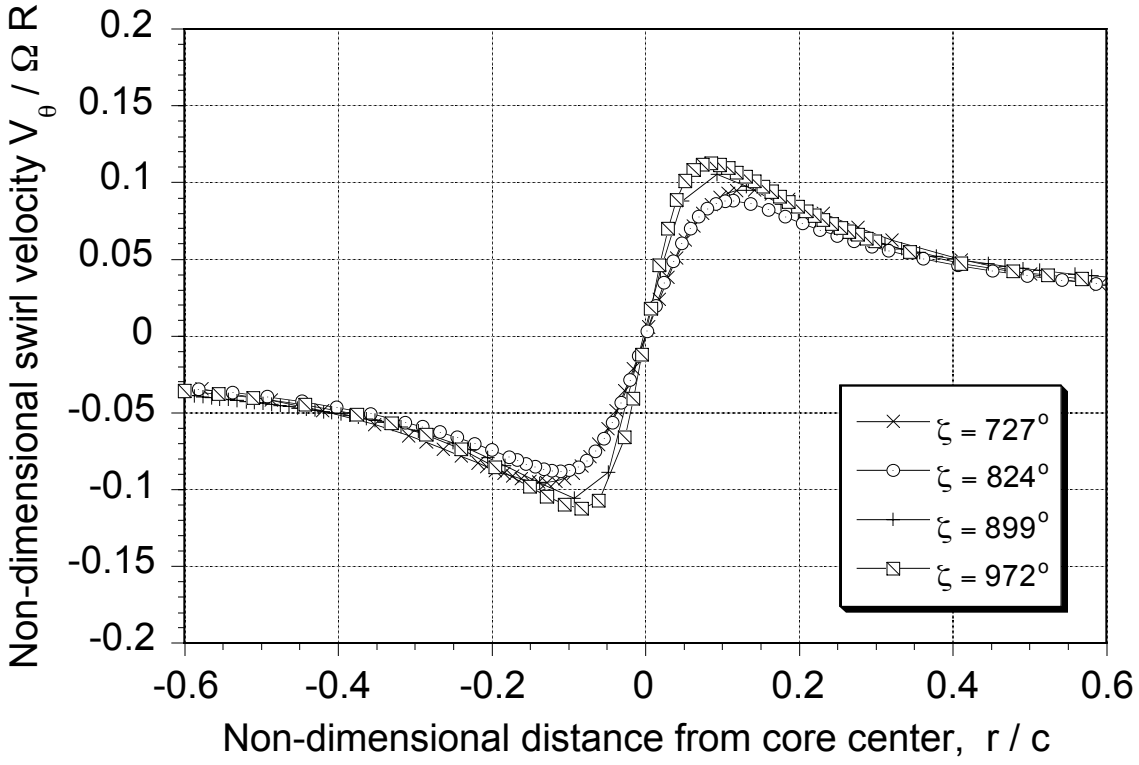

Figure 3.10: Swirl velocity profiles in the tip vortex near the solid boundary ($\zeta > 700°$), suggesting a strain dominated vortex flow.

Notice that the results from Figures 3.7 through 3.10 show that peak swirl velocity decreases as the vortex ages, which suggests a diffusion (viscous/turbulent) dominant flow. The distance between the peaks in each swirl velocity profile can be considered as indicative of (but not equal to) the viscous core diameter (see later). The peak swirl velocity at the earliest wake age ($\zeta = 16^\circ$) was about 35% of the tip speed, and this is typical of the values measured on helicopter rotors. The initial core radius was only 3.2% of blade chord (dimensionally this is only 1.4 mm), which gives some idea as the spatial resolution necessary to resolve the vortex core dimension in this case.

For the initial 600 degrees of wake age, the strain rates are small (as previously shown in Fig. 3.6) and vortex develops (diffuses) in a manner similar to the baseline case [8]. However, the last four measurements at $\zeta = 727^\circ, 824^\circ, 899^\circ$ and 972°, which are approximately around the same wake age where the estimated strain values starts to increase, show a notable decrease in the core size and an increase in the peak velocity with increasing wake age. This is a reversal in the earlier trends, which suggests that the imposed strain rates have now indeed affected the characteristics of the tip vortex. Measurements at even later wake ages was not possible because the vortex comes too close to the ground plane to be able to exclude the consideration of external viscous effects that are present there.

Core Dimension

The vortex core radius was determined from the LDV measurements based on a measurement of half the distance between two velocity peaks. To eliminate the otherwise subjective nature of this determination process, a spline curve fit to the measured velocity profiles was made, which was then used to find the distance between the two peaks. The deduced vortex core radius is plotted in Fig. 3.11 with respect to wake

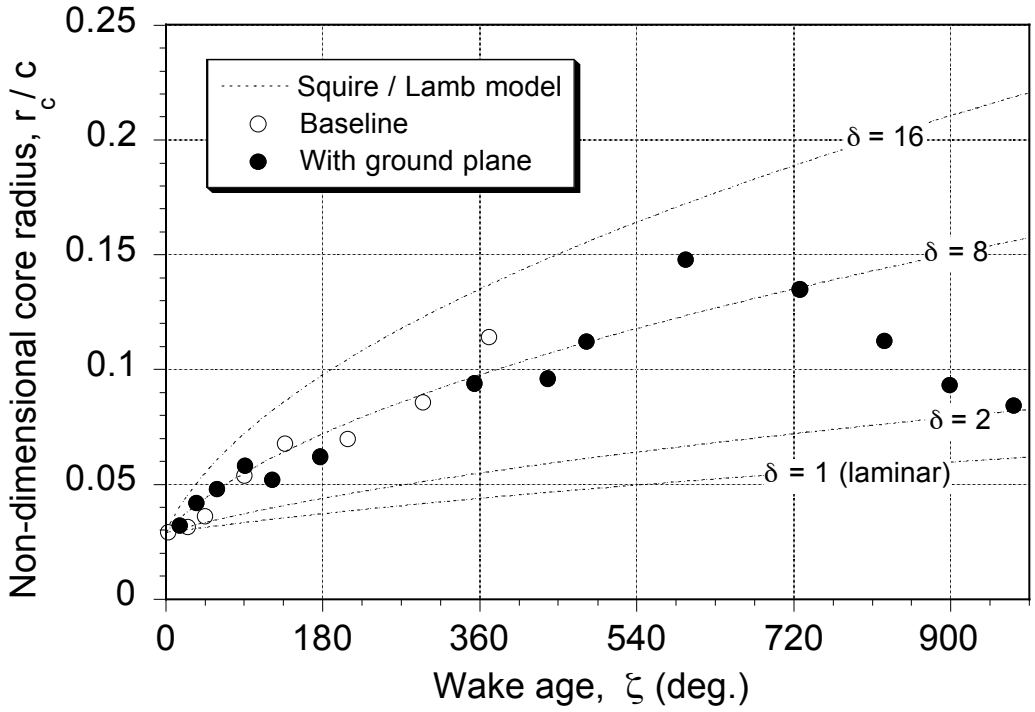

Figure 3.11: Measured growth of the vortex core radius as a function of wake age.

age. This plot, when compared along with Fig. 3.6, throws some light on the physics involved as the tip vortex is strained as it approaches the ground plane.

At early wake ages, the two sets of results (both baseline and in ground effect) in Fig. 3.11 seem to agree well, but there are some differences. This difference may be attributed to the differences in the wake geometry between the baseline case and the case with ground plane. With the presence of the ground plane, the core growth was found to be initially larger, although the differences were small. More importantly, however, at later wake ages, the growth trend was reversed as the strain rates became positive. These results suggest that the effects associated with straining of the vortex begins to balance diffusion. At the older wake ages (near the ground plane) the filament starts to stretch at a much faster rate (as shown in Fig. 3.6) and this distinctly arrests the core growth.

Results from the modified Squire/Lamb–Oseen core growth model [13, 58, 101, 109] are also shown in Fig. 3.11, which are taken as a reference to represent the effects of diffusion on the core growth (see next). It is apparent that at the earlier wake ages the measured results follow this model quite well.

Circulation

Estimated values of circulation contained in the tip vortices for the current measurements are shown in Fig. 3.12. These are obtained from the measured swirl velocity distributions by assuming flow axisymmetry in the reference system moving with the vortex core. The net circulation was determined at a distance of $0.25c$ from the vortex axis. The core circulation is that value contained within the dimension of the estimated core radius, i.e., $\Gamma_1 = \Gamma(r_c)$. Notice that the values of net circulation decrease only relatively slowly with wake age, and the core circulation stays essentially

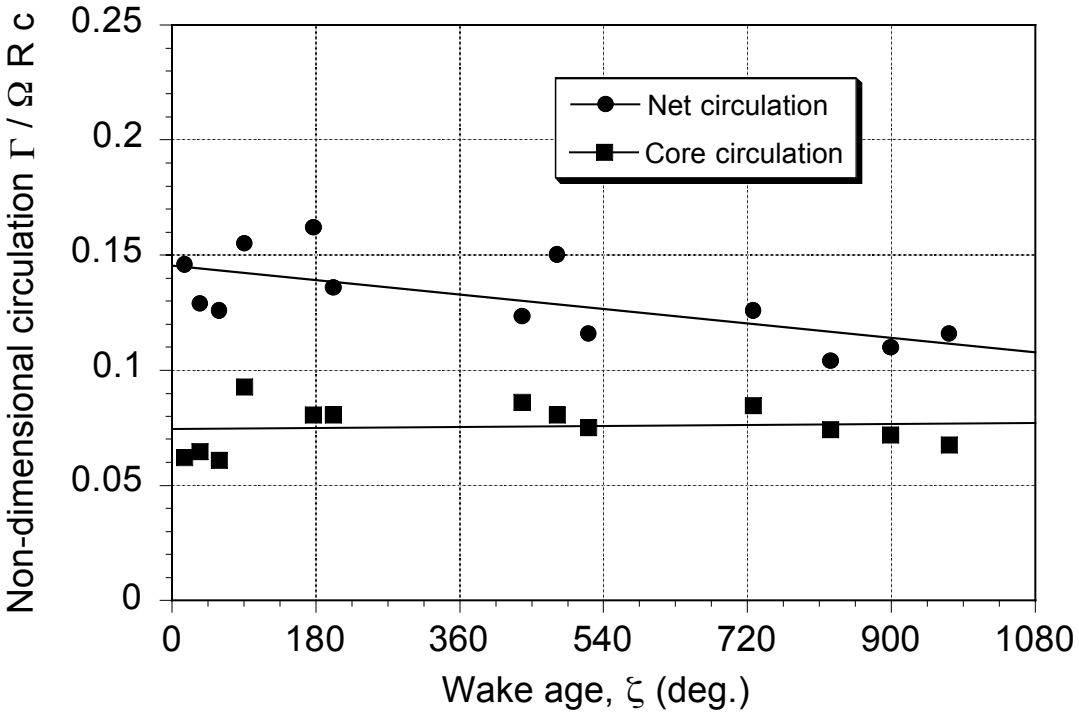

Figure 3.12: Measured circulation as a function of wake age.

constant. This confirms that dissipation of the vortex energy is small, and that the competing mechanisms in the dynamics of the tip vortex evolution are diffusion and stretching, respectively.

3.2 Analysis of the Measurements

3.2.1 Treatment of Diffusion

The swirl velocity field induced by the trailing vortex in a vortex centered coordinate system resembles that of a potential vortex at a large distance from the vortex center,

a near solid body like rotation in the viscous core of the vortex, and zero velocity at the center of the vortex – see results in Figs. 3.7 through 3.10. Numerous mathematical models are available to represent the diffusive nature of the tip vortex. A detailed explanation of a few popular models such as Lamb–Oseen model [58], Squire model [13], and Iversen model [59] have been discussed in Section 2.2.1. All the aforementioned models are pure diffusion based models and are used extensively in numerical applications for helicopter rotor analyses.

All these vortex models, even though they are derived from N–S equations, are not comprehensive enough to explain the tip vortex measurements made in a rotor flow field. For example, the classical Lamb–Oseen model [58] is singular at time $t = 0$, as well as under predicting the core growth of the tip vortices[1] – see Fig. 2.10. The modified Squire core growth model [13] correlated well with the measurements by taking into account the natural effects of turbulence in determining the growth rate of the tip vortices. An eddy viscosity parameter, δ, was included to account for the turbulent mixing on the net rate of viscous diffusion, effectively increasing the viscous core growth rates. By including an origin offset, as alluded to earlier in Section 2.2, Squire eliminated the singular nature of the tip vortex that resulted in a finite core radius and a measurable peak swirl velocity at time $t = 0$ (see Fig. 2.12). Notice that the growth of the vortex core is relatively quick at young wake ages, but grows less quickly at older wake ages. This behavior is generally consistent with experimental observations.

In light of the foregoing issues, Bhagwat & Leishman [67] suggest that the viscous core radius, r_c, of the tip vortices can be effectively modeled as a function of age, ζ,

[1]This is because of the laminar flow assumptions invoked in the model; that is, molecular diffusion only is allowed. Turbulence enhances diffusion of vorticity.

using the equation

$$r_c(\zeta) = \sqrt{4\alpha\delta\nu\left(\frac{\zeta-\zeta_0}{\Omega}\right)} \equiv \sqrt{r_0^2 + \frac{4\alpha\delta\nu\zeta}{\Omega}} \tag{3.4}$$

with $\alpha = 1.25643$. The ordinate-shift, ζ_0, is responsible for the non-zero effective core radius, r_0, at the tip vortex origin where $\zeta = 0^\circ$, to give a more physically correct (finite) induced velocity there compared to the Lamb–Oseen result. It is apparent from Eq. 3.4 that the proper determination of δ is clearly key to the success of the model. The selection of this parameter is considered in Section 3.2.5.

3.2.2 Treatment of Strain or "Stretching"

A simple example is given here to understand the interdependent consequences of strain effects acting on a viscous vortex filament as it diffuses in the rotor wake. A section of an axisymmetric vortex filament of arbitrary length, l, and with the vorticity concentrated over a cross-sectional area, S is assumed. In the absence of external viscous effects, Helmholtz's laws require conservation of circulation, Γ, of the filament, which can be mathematically stated as

$$\Gamma = \int_S \vec{\omega} \cdot \vec{dS} = \text{constant} \tag{3.5}$$

It has been shown previously in Fig. 3.12 that the measured circulation in the tip vortex decays only very slowly with wake age.

Under the influence of the local velocity field, the tip vortices convect from one point to another after time $t + \Delta t$, which results in vortex filament stretching, as shown in Fig. 1.4. Conservation of mass (constant density assumption) implies that the change in filament length must be accompanied by a corresponding change in the cross-sectional area over which the vorticity is distributed. Therefore, a change in

the filament length is accompanied by a proportional change in its vorticity. In cases where the strains are large, this can have a pronounced effect on the induced velocity field in the immediate vicinity of the vortex filament.

It can be assumed that the bulk of the vorticity is contained with the vortex core, although this depends on the assumption of a particular velocity profile. The change in the core radius resulting from the imposed strain is calculated using the conservation of mass principle [37], i.e.,

$$\begin{aligned} \pi {r_c}^2 l &= \pi (r_c - \Delta r_c)^2 (l + \Delta l) \\ \left(\frac{r_c - \Delta r_c}{r_c}\right)^2 &= \frac{l}{l + \Delta l} \\ \text{or} \qquad \Delta r_c &= r_c \left(1 - \left(\sqrt{1+\varepsilon}\right)^{-1}\right) \end{aligned} \tag{3.6}$$

where ε is defined as the strain of the vortex filament as given in Eq. 3.3.

Equation 3.6 is derived with the assumption that the flow is incompressible. As a result, the above expression is strictly valid only in constant density flow fields. In compressible flow, the stretching of the filament need not necessarily be accompanied by an increase in vorticity because the density of the fluid will also change with filament stretching. Even though the formation of rotor tip vortices clearly involve compressibility effects [72], it is reasonable to assume to a first level of approximation that the *changes* in flow density are considerably small. This suggests that an increase in vorticity can be considered to be the primary effect of filament stretching.

3.2.3 Correction for Strain Effects

It is understandable from the earlier discussions that the mechanisms of diffusion *and* the effects of strain fields are interdependent. Both play a substantial role in determining various properties of viscous core such as core radius and peak swirl velocity. In

Fig. 3.13, the core growth for the two cases are shown as a function of wake age. In this case, the results also include the development of the core radius, which has now been corrected to account for the effects of strain. This is done by following an inverse procedure, assuming the validity of Eq. 3.6, along with the measured values of strain as given in Fig. 3.6. The inverse procedure starts with determining a pseudo-time from the measured core radius, which includes the effects of strain. This pseudo-time is the actual time that the vortex would have taken to reach the measured core radius by simple diffusion alone, i.e.,

$$t_{\text{eff}}(\zeta) = \frac{r_c(\zeta)}{(4\alpha\nu\delta/\Omega)} \tag{3.7}$$

As the effect of strain on the characteristics of the tip vortices at a current time is cumulative, the pseudo-time for all the previous wake ages are calculated by including the corresponding strain that is obtained from the measurements. This step is continued until an effective initial time, $t_{\text{eff}}(0)$ is determined from this recurrence equation, i.e.,

$$\begin{aligned} t_{\text{eff}}(\zeta-1) &= t_{\text{eff}}(\zeta)\,(1+\varepsilon(\zeta)) \\ t_{\text{eff}}(\zeta-2) &= t_{\text{eff}}(\zeta-1)\,(1+\varepsilon(\zeta-1)) \qquad \text{until} \\ t_{\text{eff}}(0) &= t_{\text{eff}}(1)\,(1+\varepsilon(1)) \end{aligned} \tag{3.8}$$

With $t_{\text{eff}}(0)$ as the initial effective time, the value of vortex core size for a given wake age through diffusion alone can be estimated using Squire's core growth model.

It is apparent from Fig. 3.13 that while the correction only makes a difference at older wake ages where the strain rates are large, the results fall into much better agreement with the trends that might result only from pure diffusion (without the effects of strain). The results suggest that an average value of $\delta = 8$ gives good agreement with the experimental results measured here.

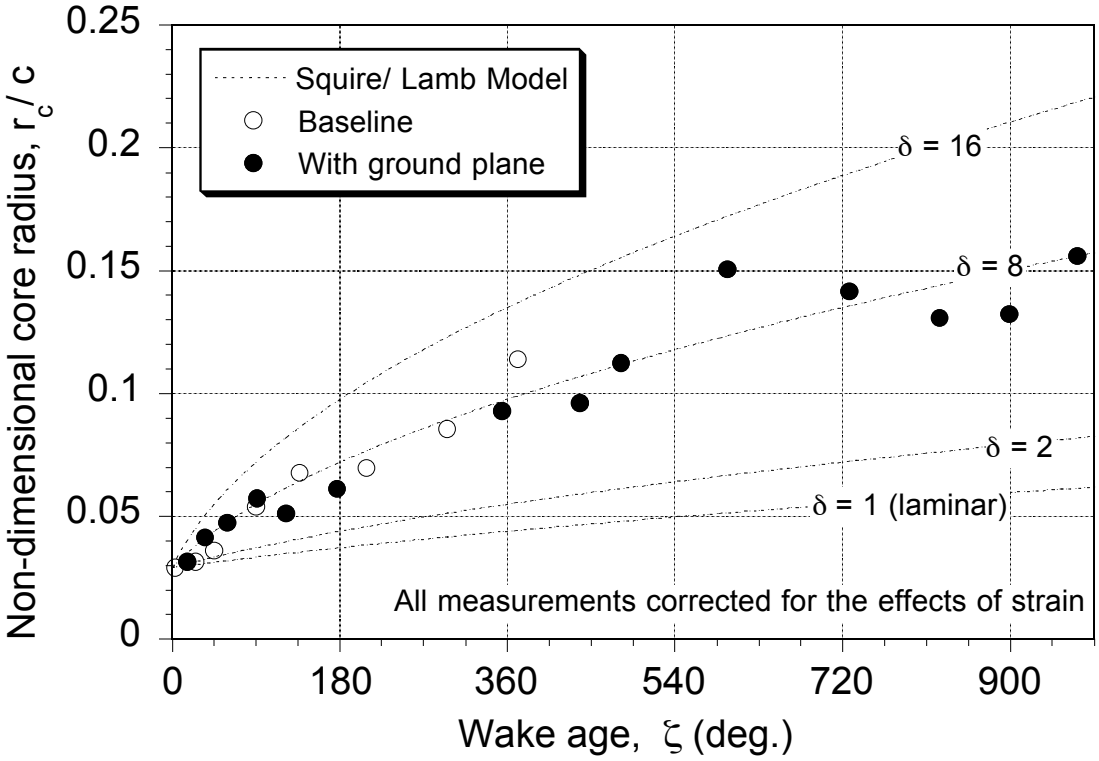

Figure 3.13: Trends in the core growth when correcting the measurements for the effects of filament strain.

3.2.4 Combined Growth Model

The ability to isolate and correct for the effects of vortex filament strain suggest that a vortex model can be developed that accounts for both the effects of diffusion and the effects of flow field strain. Ananthan et al. [37] derived an expression for the effective core radius of the tip vortex at a given time t that combines both diffusion and the vortex filament strain effects. By writing

$$r_{c_{\text{eff}}} = r_{c0}\left(\sqrt{1+\varepsilon}\right)^{-1} \tag{3.9}$$

the effective diffusion time for the filament was calculated based on Squire model Eq. 3.4 using

$$t_{\text{eff}} = \frac{(r_{c_{\text{eff}}})^2}{4\alpha\nu\delta} = \left(\frac{r_{c0}^2}{4\alpha\nu\delta}\right)\frac{1}{1+\varepsilon} = \frac{t}{1+\varepsilon} \tag{3.10}$$

It can be observed from the above equation that for a positive strain, the value of t_{eff} reduces suggesting that the time that would have taken for the vortex core to reach a particular core size based on simple diffusion alone will be smaller than the one undergoing strain. Because the core size is directly proportional to the time, t, a vortex filament that undergoes positive filament strain will result in a smaller core size than the one with pure diffusion alone at the same time. The core growth predicted by the new model that combines the effects of vortex filament strain and viscous diffusion is given by

$$r_c(t) = \sqrt{r_o^2 + 4\alpha\nu\delta t_{\text{eff}}} = \sqrt{r_o^2 + 4\alpha\nu\delta t(1+\varepsilon)^{-1}} \tag{3.11}$$

It should be kept in mind that the effect of strain on the vortex filament is cumulative, which means that the core size of the vortex filament undergoing strain depends on the magnitude of strain over all previous wake ages unlike viscous diffusion. Rewriting t as

$$t = \int_{t_0}^{t} dt \tag{3.12}$$

the time $t(1+\varepsilon)^{-1}$ in Eq. 3.11 can now be integrated to account for the cumulative effects of vortex filament strain. Upon substituting Eq. 3.12 in Eq. 3.11, the core growth predicted by the new model is given by

$$r_c(t,\varepsilon) = \sqrt{r_0^2 + \frac{4\alpha\delta\nu}{\Omega}\int_{t_0}^{t}(1+\varepsilon(t))^{-1}dt} \tag{3.13}$$

As $\zeta = t\Omega$, the above equation can be written in terms of wake age as

$$r_c(\zeta,\varepsilon) = \sqrt{r_0^2 + \frac{4\alpha\delta\nu}{\Omega}\int_{\zeta_0}^{\zeta}\Big[1+\varepsilon(\zeta)\Big]^{-1}d\zeta} \tag{3.14}$$

As previously discussed, the strain rate, ε, can be determined based on a knowledge of the velocity field in which the vortex develops. This would normally be calculated as part of the rotor wake model (e.g., in a free-vortex scheme [37]). Notice that there are two empirical parameters in this model that are used to describe the viscous development: the initial core radius, r_0 (or virtual time, ζ_0), and the average turbulent diffusion parameter, δ, which is known to depend on vortex Reynolds number (see later).

To illustrate the significance of stretching effects using Eq. 3.14, Ananthan et al. [37] subjected a viscous dominant rectilinear vortex filament to two different strain conditions: 1. A uniform strain rate of the form $V_\varepsilon(\zeta) = \text{constant}$, and 2. A linear strain rate given by

$$V_\varepsilon(\zeta) = A + \Big(\frac{dV_\varepsilon}{d\zeta}\Big)\zeta \tag{3.15}$$

where the strain rate, $V_\varepsilon(\zeta)$, is defined as $d\varepsilon/dt$. The results were compared with the baseline case where viscous diffusion alone (with $\delta > 1$) is allowed in a zero strain field. The results of applying different uniform strain rates and different linear strain rates on the viscous core growth of a rectilinear vortex filament as a function of time (wake age) are shown in Figs. 3.14 and 3.15 respectively.

It was shown from Fig. 3.14 that the effect of strain on the core development differs depending on whether the filament length increases (stretches) or decreases (contracts) with time. A negative strain or a reduction in the length of the vortex filament means an increase in the size of the vortex core to conserve circulation (also to conserve volume). Notice that, in this case, the effect of strain on the evolution of tip vortices complements the effect of diffusion as both tend to increase the core size with time. This will result in a higher growth rate of the tip vortex core when compared with the core growth predicted by simple diffusion based vortex models.

On the other hand, an increase in the vortex filament (positive strain) results in a decreased core size and more concentrated vorticity. Notice that an extreme case of infinite stretching of vortex filament will result in the classical Lamb vortex when $r_0 = 0$. An infinite amount of stretching would result in zero core radius with infinite vorticity at the center of the vortex. In this case, the effect of strain acts against the diffusion effects and the core radius becomes nominally constant for later values of time. Here, after an initial development, the increase in core radius resulting from viscous diffusion can be balanced by the decrease in the core radius as a result of filament stretching.

The computed core growth for different linearly imposed strain rates given by Eq. 3.15 (with the assumption of $A = -0.5$) is shown in Fig. 3.15. Even though A would take smaller value than this in practice in a rotor flow field, these conditions are representative of the strain rate conditions found in the wake of a rotor operating in hovering flight, where the wake initially contracts below the rotor (negative strain rate) and then becomes constant or slowly starts to expand radially outwards (positive strain rate) as the vortices get older and are convected into the downstream wake region (see Fig. 3.6). One interesting observation from Fig. 3.15 is that the vortex

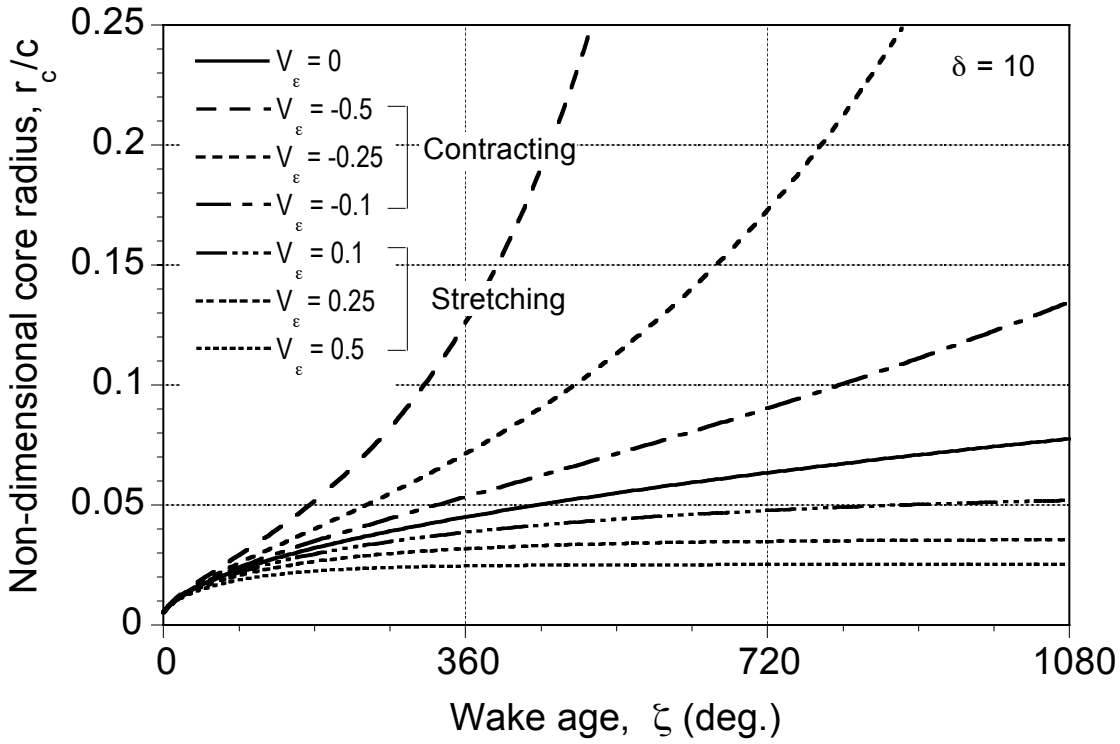

Figure 3.14: Representative growth of the viscous core radius of a rectilinear vortex filament as a function of time (wake age) for uniformly imposed strain rates [37].

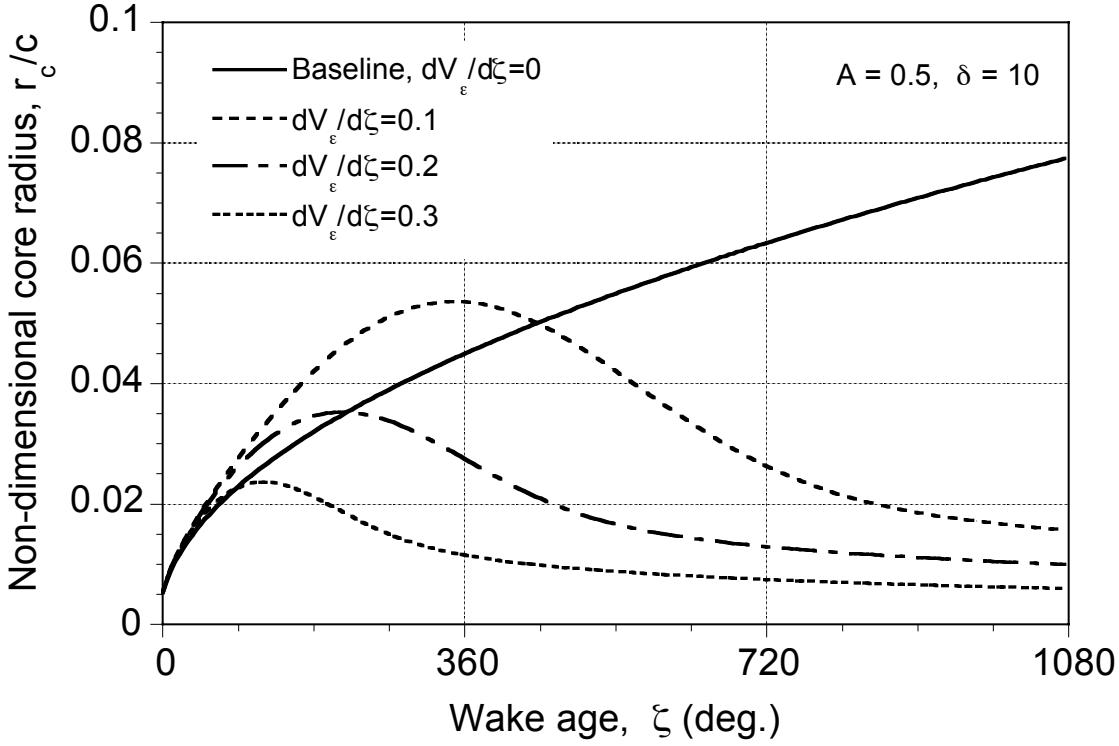

Figure 3.15: Representative growth of the viscous core radius of a rectilinear vortex filament as a function of time (wake age) for linearly imposed strain rates [37].

core of the baseline case (without strain rate effects) at older wake ages is much larger than that found with the applied strain rate. In other words, the strain exerted on the filaments is so large that the segments of the wake undergoing positive strain or stretching may have a much smaller core radius, even though they have existed in the flow for a longer time. This means that the peak induced velocity surrounding those segments is larger and the vorticity is more concentrated than that found at the earlier wake ages.

To further show the validity of the model given in Eq. 3.14, it has been used to predict the core growth with the assumption of $\delta = 8$ (see Fig. 3.13) and using the strain rates defined by the results plotted in Fig. 3.6. These core growth results are shown in Fig. 3.16, where it is apparent that the assumed model faithfully predicts the measured behavior. Such levels of correlation give considerable confidence in the ability of this type of relatively parsimonious model to predict the viscous core growth for a tip vortex encountering an arbitrarily imposed strain rate.

3.2.5 A Model for δ

As previously mentioned, the determination of the turbulent diffusion parameter δ is key to the success of the core growth model. A purely laminar flow (i.e., where viscous diffusion of vorticity takes place on the molecular level alone) then $\delta = 1$. In such a case, with $\varepsilon = 0$ and $r_0 = 0$, then Eq. 3.14 reduces to the classical Lamb–Oseen core growth model. In most practical cases of lift generated tip vortex flows, however, experimental measurements suggest that turbulent flow effects increase the average rate of diffusion of vorticity so that $\delta > 1$, therefore increasing the core growth rates. The details of this core growth process, however, are not fully understood or documented with helicopter rotors, and existing experimental results are not entirely

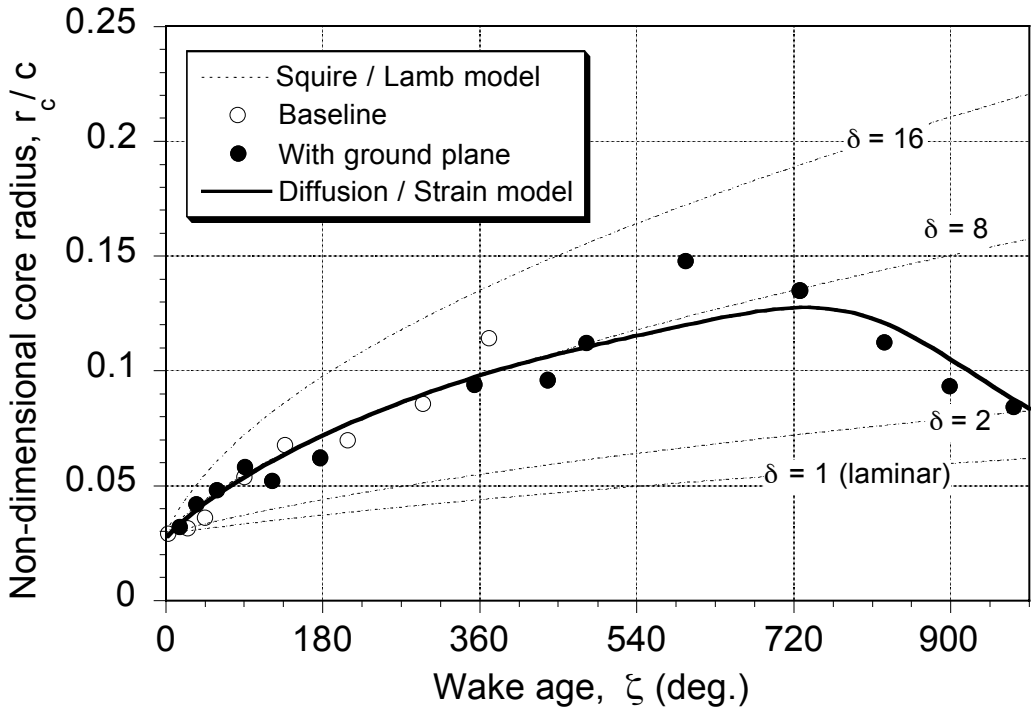

Figure 3.16: Predictions of core growth under the assumptions of viscous diffusion with $\delta = 8$ in a known strain field.

conclusive. There is evidence that the inner core growth is laminar and there is no turbulent mixing effects to enhance the diffusion of vorticity in this region [8, 65]. There is also evidence that turbulent flows surrounding the vortex core can be re-laminarized. Other measurements suggest that there is turbulence at the edges of the laminar core [79], which acts to enhance the net diffusive growth characteristics of the tip vortex.

While complete understanding the details of tip vortex flows still requires much further research, more readily derived vortex properties such as the peak swirl velocity and effective core size can be used to better understand the overall vortex modeling requirements. While the value of δ can be estimated from the present measurements (which suggests $\delta \approx 8$), in the general case δ will be a function of vortex Reynolds number $Re_v = \Gamma_v/\nu$. For the present measurements, Re_v is of the order of 10^5. For a full-scale rotor, however, the values of Re_v may be of the order of 10^7 or greater. Therefore, the difficulty in constructing a more general vortex model that has a wide range of applicability is to establish how δ will vary with Re_v.

Functional Representation for δ

Squire [13] hypothesized that δ should be proportional to the vortex circulation strength. The value of δ was then formulated in terms of the vortex Reynolds number as

$$\delta = 1 + a_1 Re_v \tag{3.16}$$

where a_1 is a parameter that must be determined empirically from tip vortex measurements.

Bhagwat & Leishman [67] have shown a correlation between the non-dimensional peak swirl velocity and the wake age, ζ, or equivalent downstream distance, d, of the

vortex by following an approach similar to that of Iversen [59]. This correlation takes the form

$$\overline{V}_{\theta_{\max}} \left(\overline{d} + \overline{d}_0\right)^{\frac{1}{2}} = k \tag{3.17}$$

where the constants $\overline{d}_0$ and k can be determined empirically. Bhagwat [101] modified the expression for the non-dimensional peak swirl velocity and the equivalent downstream distance in terms of rotational speed of the rotor and wake age (instead of the free stream velocity and time) as given by:

$$\overline{V}_{\theta_{\max}} = \left(\frac{V_{\theta_{\max}}}{\Omega R}\right)\left(\frac{\Omega R c}{\Gamma_{\mathrm{v}}}\right) \tag{3.18}$$

and

$$\overline{d} = \zeta\left(\frac{\Gamma_{\mathrm{v}}}{\Omega c^2}\right) \tag{3.19}$$

Examples of the "Iversen-like" correlation curves are shown for fixed-wing tip vortex measurements in Fig. 3.17, and for rotating-wings in Fig. 3.18. In the case of a fixed-wing, measurements have been taken from Refs. 12, 52, 53, 55, 57, 110, 111 and 54. For rotating-wings, measurements have been taken from Refs. 18, 19, 75 and 16. The measurements obtained in the present work were obtained at relatively old wake ages compared to those shown in other measurements, and so can be used to further augment the correlation curves. In both cases (see Figs. 3.17 and 3.18), the measurements show a definitive trend as given by Eq. 3.17. With the transformation that $t = z/V_\infty$ or $t = \zeta/\Omega$, the correlation given by Eq. 3.17 shows that

$$V_{\theta_{\max}} \propto \sqrt{\frac{\Gamma_{\mathrm{v}}}{t}} \tag{3.20}$$

Bhagwat [101] compared the above equation with the peak swirl velocity predicted

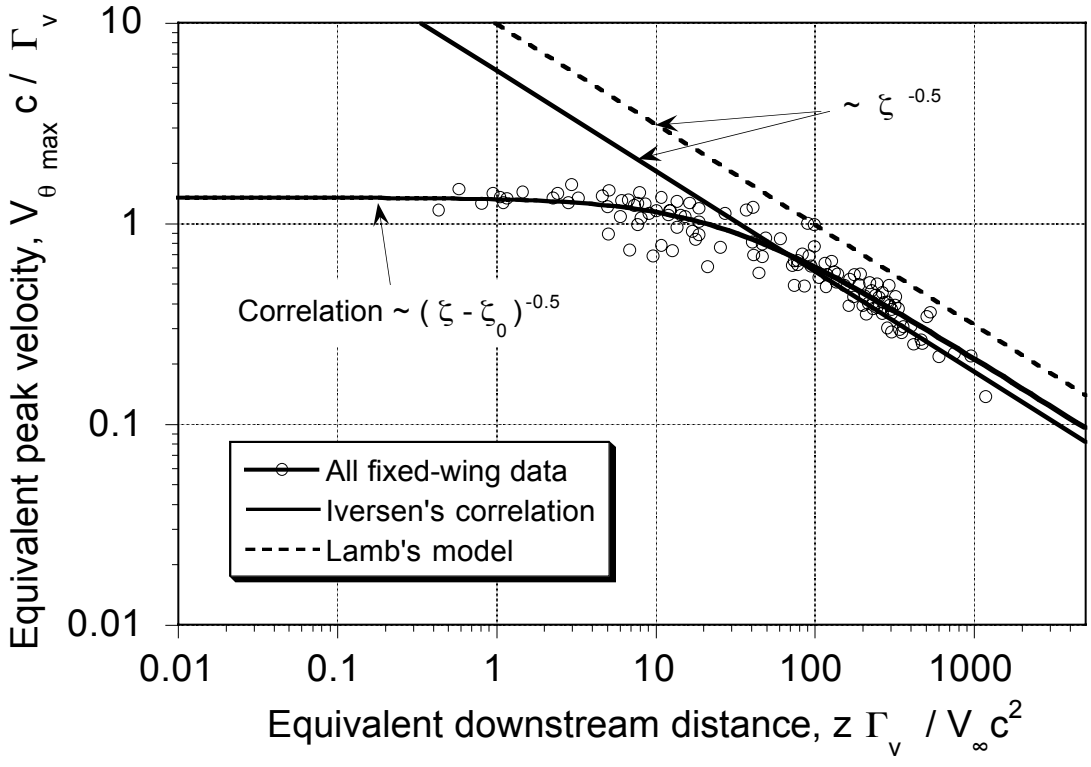

Figure 3.17: Correlation of peak swirl velocity with equivalent downstream distance for fixed-wing tip vortex measurements.

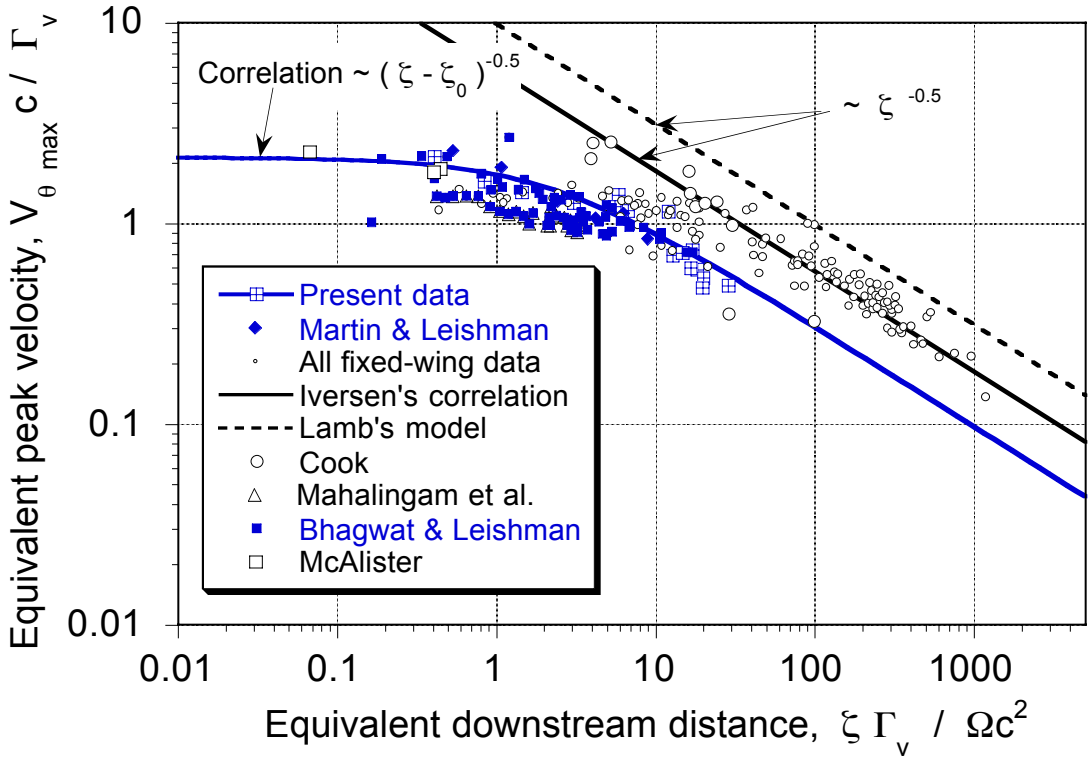

Figure 3.18: Correlation of peak swirl velocity with equivalent downstream distance for rotor tip vortex measurements.

by the Lamb–Oseen model that is given by

$$V_{\theta_{\max}} \propto \frac{\Gamma_v}{2\pi r_c} \propto \frac{\Gamma_v}{\sqrt{\delta \nu t}} \propto \sqrt{\frac{\Gamma_v}{t}} \sqrt{\frac{1}{\delta}\left(\frac{\Gamma_v}{\nu}\right)} \tag{3.21}$$

and suggested that

$$\frac{1}{\delta}\left(\frac{\Gamma_v}{\nu}\right) = \frac{Re_v}{\delta} = \text{constant} \tag{3.22}$$

which means that the average apparent viscosity coefficient, δ, is proportional to the vortex Reynolds number, Γ_v/ν. Therefore, this analysis supports the initial hypothesis made by Squire that

$$\delta = 1 + a_1 Re_v \tag{3.23}$$

Determination of δ and a_1

Figure 3.19 shows an assemblage of tip vortex measurements (from the many sources cited previously) as the estimated value of δ from the measured core growth results which is then plotted versus the corresponding vortex Reynolds number. The data include results from fixed-wing as well as rotating-wing trailing vortices. Lines are shown for the predominantly laminar trend, along with the trends obtained on the basis of Squire's hypothesis.

For low Reynolds numbers, the measurements show small and nominally constant values of δ, suggesting that the core is mostly laminar for these Reynolds numbers. However, it is apparent that δ increases with increasing Reynolds number, with an almost linearly increasing trend at higher Reynolds numbers. Notice that any experimental values of $\delta < 1$ are physically impossible, and the various challenges and uncertainties in experimental measurements may account for such inconsistencies. The overall experimental evidence, however, strongly suggests the validity of Squire's hy-

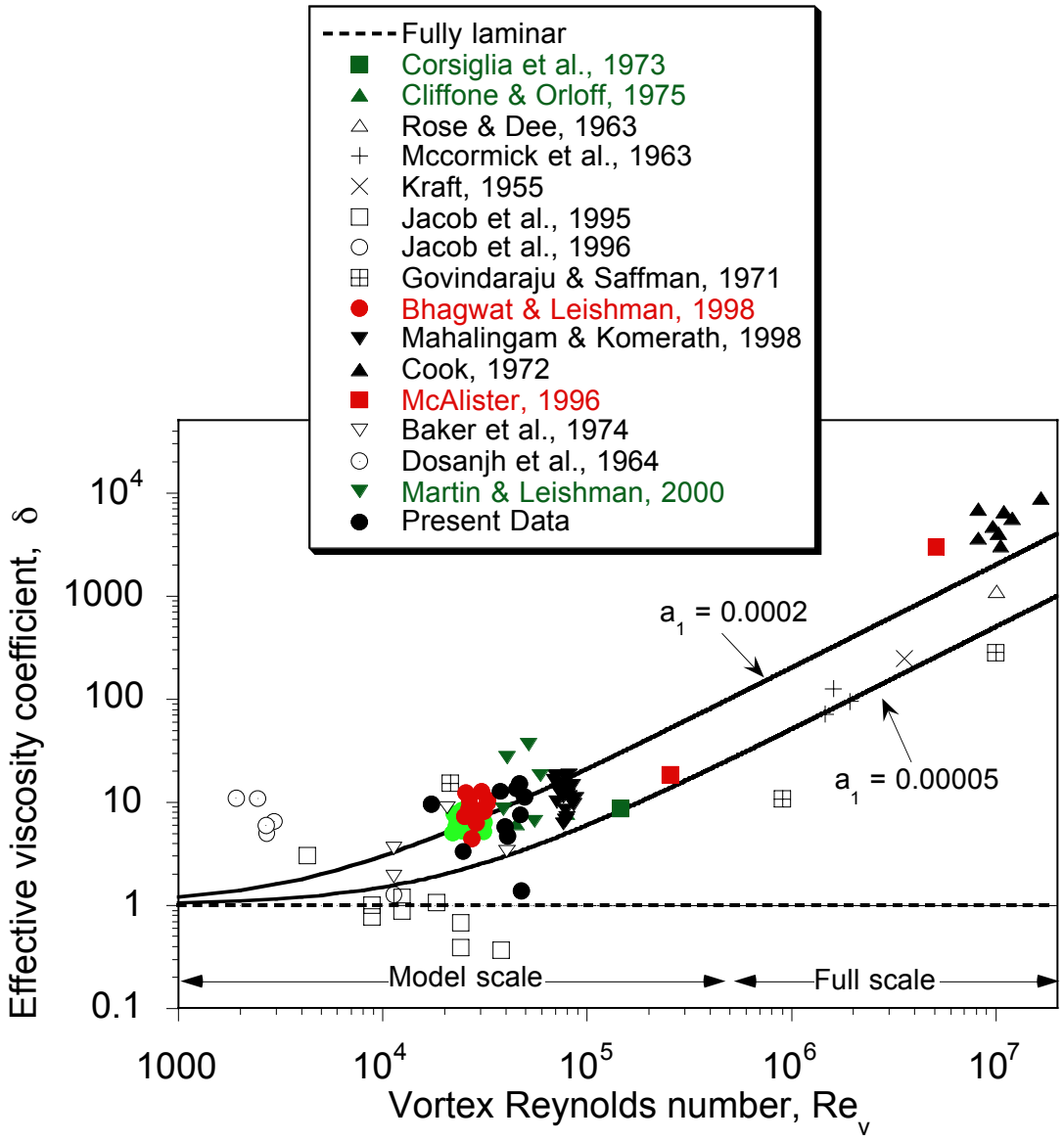

Figure 3.19: Effective diffusion parameter, δ, as a function of vortex Reynolds number, Re_v.

pothesis that turbulent diffusion of vorticity from within the vortex core is directly proportional to the vortex Reynolds number.

Figure 3.20 shows the same experimental data in the form of Squire's parameter, a_1. Bhagwat & Leishman [101] estimated the overall value of a_1 from these measurements to be in the range $O\left(10^{-3}\right)$ to $O\left(10^{-4}\right)$. By considering only the rotating wing measurements, the value of a_1 was found to be higher ($O\left(10^{-4}\right)$ when compared with that of the fixed wing alone ($O\left(10^{-5}\right)$. The reason for the difference in the value of a_1 was attributed to the the implicit effects of vortex straining in the case of rotating wing that results from filament curvature and other wake distortion effects.

However, it would be ideal to have a single value for a_1 for the development of models. Moreover, the hypothesis suggested by Squire, which was used for determining a_1, does not consider the effects of flow rotation on the evolution of turbulent tip vortices. This suggests the need for developing an eddy viscosity model (because δ relates the eddy viscosity and kinematic viscosity) that includes flow rotation effects on the evolution of tip vortices. By applying this model to the N–S equations, the solution of which upon comparing with the Squire's core growth model can produce in a single value for a_1. This will enable the development of a more comprehensive tip vortex model that includes stretching effects, flow rotation effects and vortex Reynolds number effects.

It can be concluded that Eq. 3.11 provides a best available model for the growth of the viscous core of a trailing tip vortex, with the value of the empirical parameter a_1 being determined from various vortex experiments, as described previously [101]. For full-scale helicopter rotors, which will have much larger values of Re_{v}, the correlation curve would suggest values of $\delta \approx 1000$. This suggests that the tip vortex may exhibit diffusive characteristics that are orders of magnitude larger than those expected on the

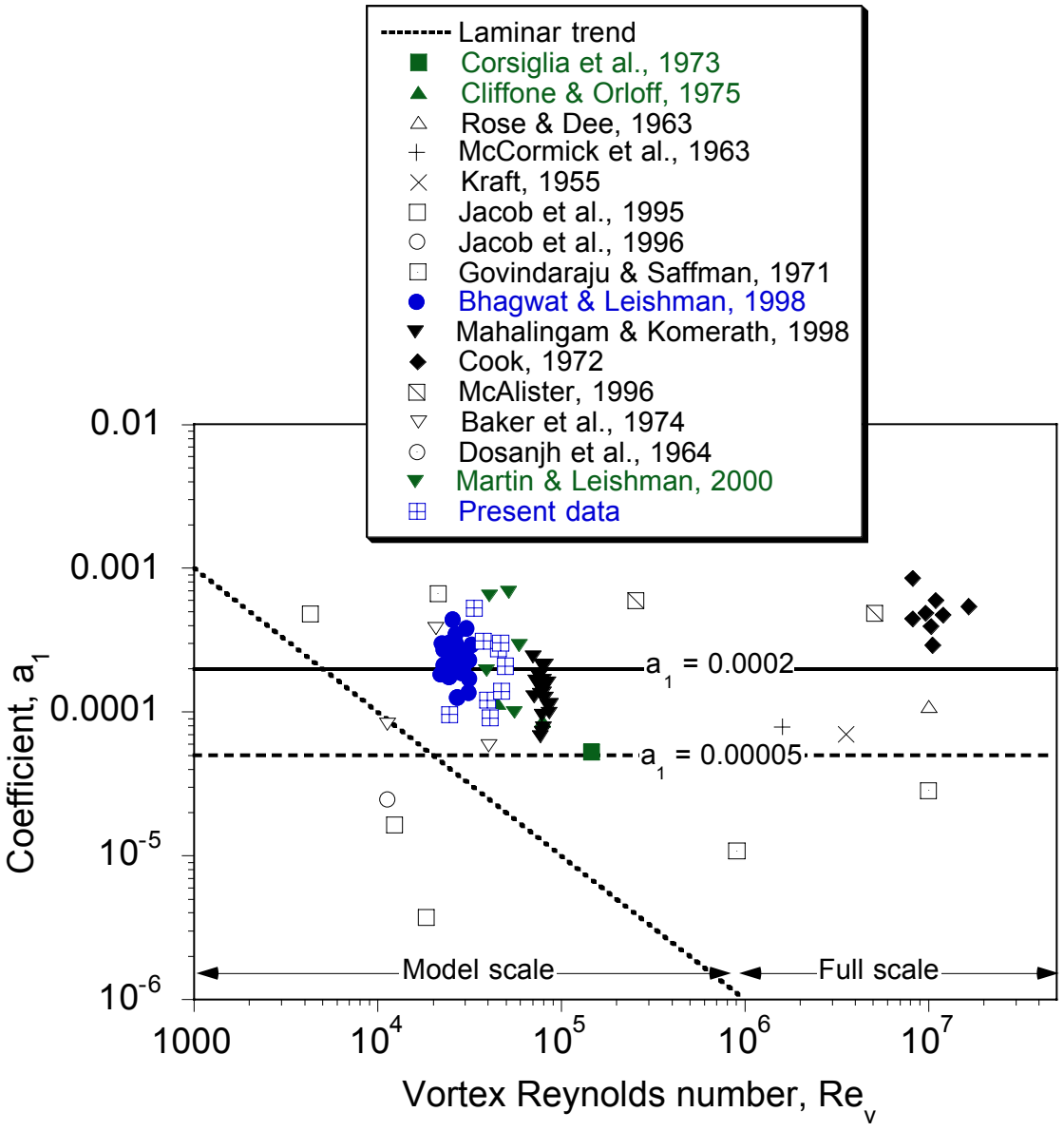

Figure 3.20: Effective viscosity parameter, a_1, as a function of vortex Reynolds number, Re_v.

basis of laminar diffusion alone.

Finally, some estimate for r_0 is in order. The initial core radius of trailing vortices has been measured to be typically $5-10\%$ of chord, i.e., of the order of the airfoil thickness at the blade tip where the vortex originated. The effective origin offset, z_0 or ζ_0, can then be established from the initial core radius, r_{c_0}, by using Eq. 3.4 or Eq. 3.11. It would seem that from the data shown, ζ_0 is typically between 20 and 25 degrees.

Aperiodicity and Axial Velocity

The effect of vortex filament stretching on the core growth properties of tip vortices have been measured and quantified. Aperiodicity correction played a significant role in determining the relationship between the strain and core growth properties. Figure 3.21 shows the measured core size of tip vortices before and after correction for aperiodicity effects. It can be observed from the uncorrected measurements that the size of the vortex core appears to be increasing even when the tip vortices are closer to the ground plane and the vortex filaments are stretched significantly. This can be explained using Fig. 2.7, which shows that the aperiodicity of tip vortices increases in both radial and axial direction for increase in wake age. As a result, the core appears to be larger in the uncorrected measurements. The measured aperiodicity, which was later used for correcting the measurements (using the scheme developed by Leishman [69] and explained in Appendix A), brought the results back to what would have been expected in the absence of aperiodicity effects. The corrected profiles show a clear decrease in the core size for increasing wake age as the tip vortices approach the solid boundary.

However to measure the effects of vortex filament strain on the axial velocity of

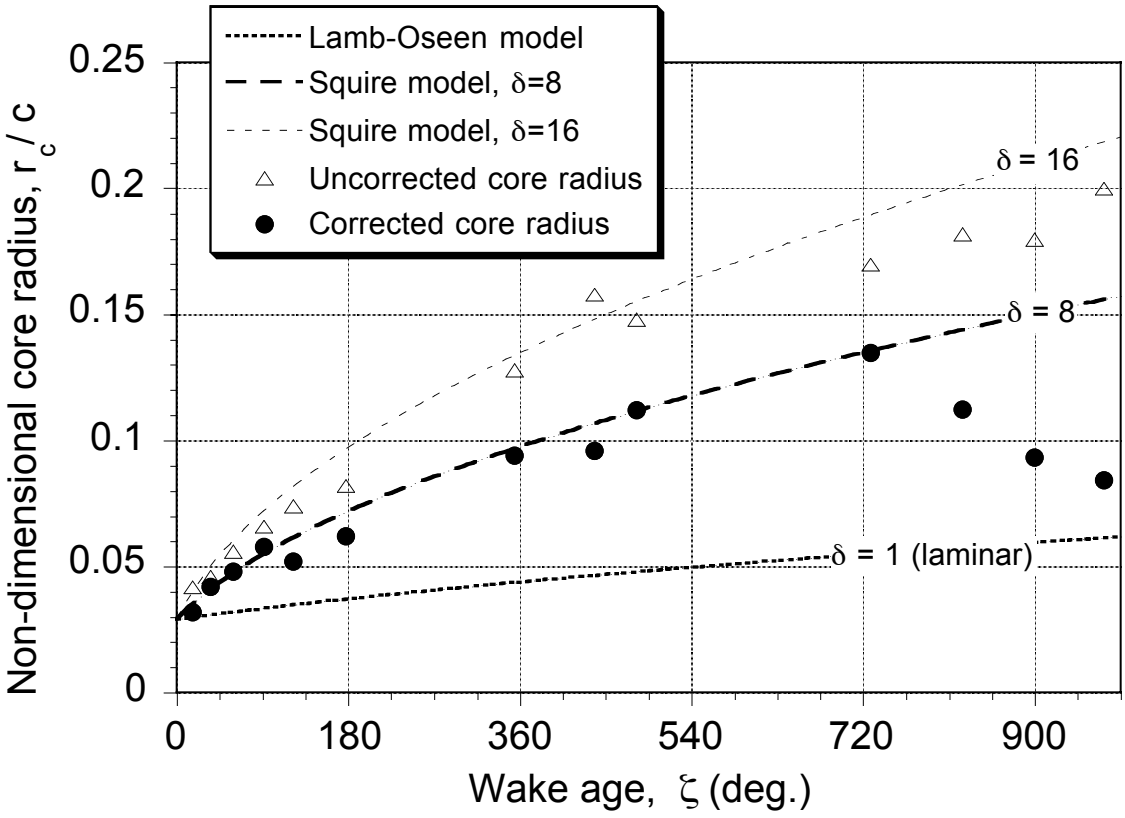

Figure 3.21: Measured core size of tip vortices at various wake ages - before and after correction for aperiodicity effects.

the tip vortices, it is essential to understand the practical difficulties involved in not only measuring the axial velocity profile in a known strain field but also in correcting for the effects of aperiodicity. The axial velocity has its peak at the center of the tip vortex. As a result, aperiodicity will have significant effects on the peak axial velocity. Even though the principle of correcting the axial velocity profile is identical to that of the swirl velocity profile, no scheme has yet been developed in the past to correct for the effects of aperiodicity on the axial velocity profiles. Also, there had been results suggesting that the axial velocity reduces substantially within one-quarter of the rotor revolution [8]. Even though in the current experiment, it was possible to make swirl velocity measurements at very old wake ages (972°) (a by-product of filament stretching that countered diffusion), it may not be possible to make axial velocity measurements at such old wake ages. This is because the vortex filament stretching may not be large enough to have measurable effects on the axial velocity inside the tip vortices.

3.3 Generalized Transitional Vortex Model

In this section, the circulation, peak swirl velocity and the core growth predicted by the new generalized transitional vortex model are given. The results are then validated with the available experimental measurements. The results are plotted both in terms of wake age as well as in terms of vortex Reynolds number so that measurements made at different scales can be compared. A numerical solution to the governing equation for the vortex given by Eq. 2.50 was obtained using a Runge-Kutta integration scheme nested with a shooting technique that is explained in detail in Section 2.2.8 .

The final expression (circulation distribution as a function of normalized distance

from the vortex core center) is

$$\frac{\Gamma}{\Gamma_{\mathrm{v}}}\left(\frac{r}{r_c}\right) = \gamma\left(\frac{\eta}{\eta_c}, Re, Ri\right) \tag{3.24}$$

where

$$\frac{\eta}{\eta_c} = \sqrt{\frac{r}{r_c}} \tag{3.25}$$

is a function of vortex Reynolds number that also takes into account the effects of flow rotation (Richardson number) on the development of the tip vortices. The effects of Richardson number appear in the expression for the VIF, which as described in Section 2.2.7 models the variation of eddy viscosity across the tip vortex. Swirl velocity profiles can be obtained from the circulation distribution equation that, in turn, helps in the process of determining the core radius and peak swirl velocity.

3.3.1 Swirl Velocity and Circulation

The resulting swirl velocity distribution versus non-dimensional radial distance is shown in Fig. 3.22, along with the measurements obtained from Ramasamy et al. [38] for $Re_{\mathrm{v}} = 48{,}000$. This figure also includes the velocity distribution obtained from the laminar Lamb–Oseen model and the completely turbulent Iversen model for comparison. It is apparent that the new model predicts the velocity much better than either of the other two models primarily because the new model is able to demarcate the three different regions of the vortex.

Figure 3.23 shows the distribution of the ratio of local circulation Γ to large radius circulation Γ_{v} versus non-dimensional radial distance. By plotting the measurements from Ref. 38 it is evident that the new model predicts the non-dimensional circulation distribution much better than the constant viscosity model (Lamb) or the variable viscosity model (Iversen), or even the multi-region vortex model (Tung).

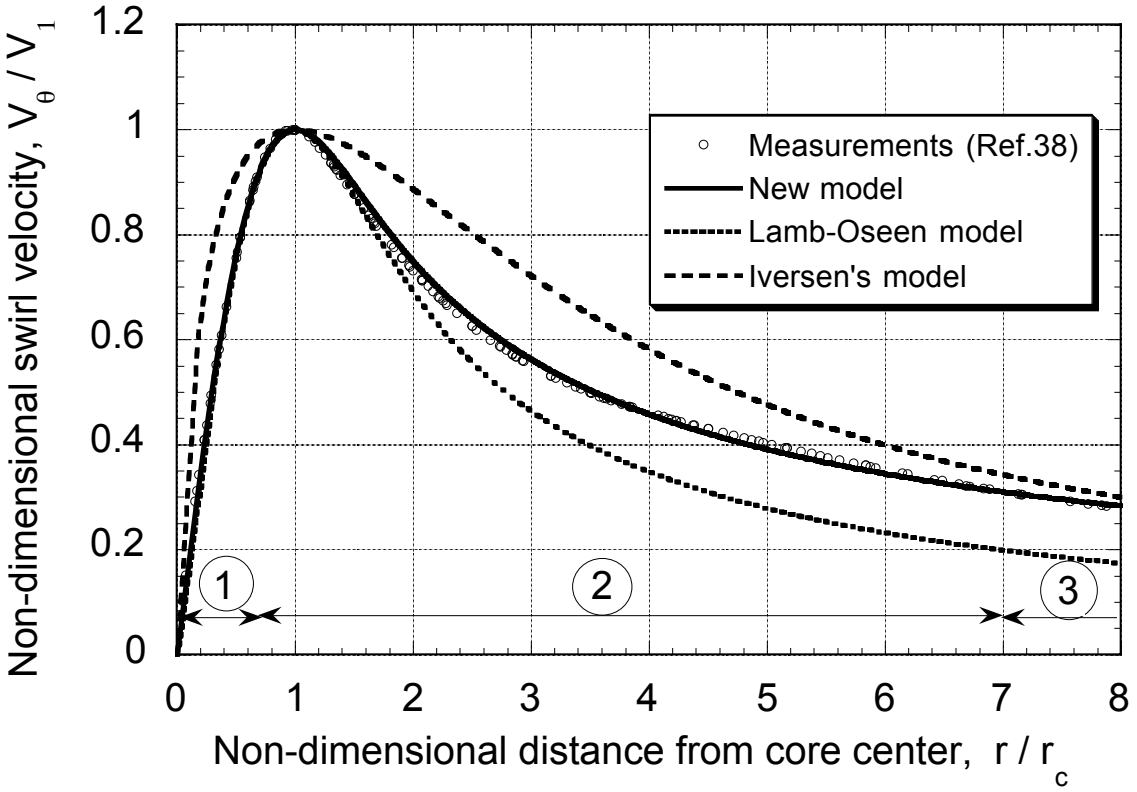

Figure 3.22: Swirl velocity distribution using new model for $Re_v = 48,000$, (1) Laminar region, (2) Transitional region, (3) Turbulent region.

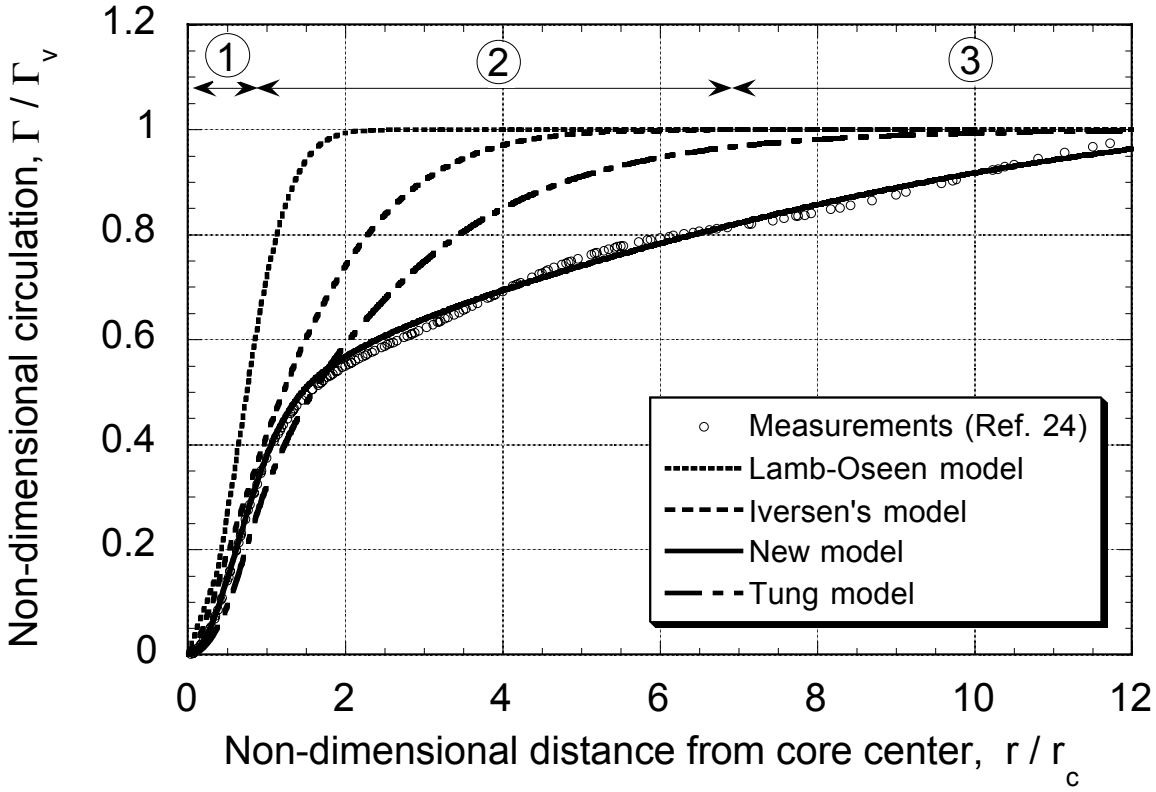

Figure 3.23: Ratio of circulation to circulation ar large distance, $Re_{\mathrm{v}} = 48{,}000$, (1) Laminar region, (2) Transitional region, (3) Turbulent region.

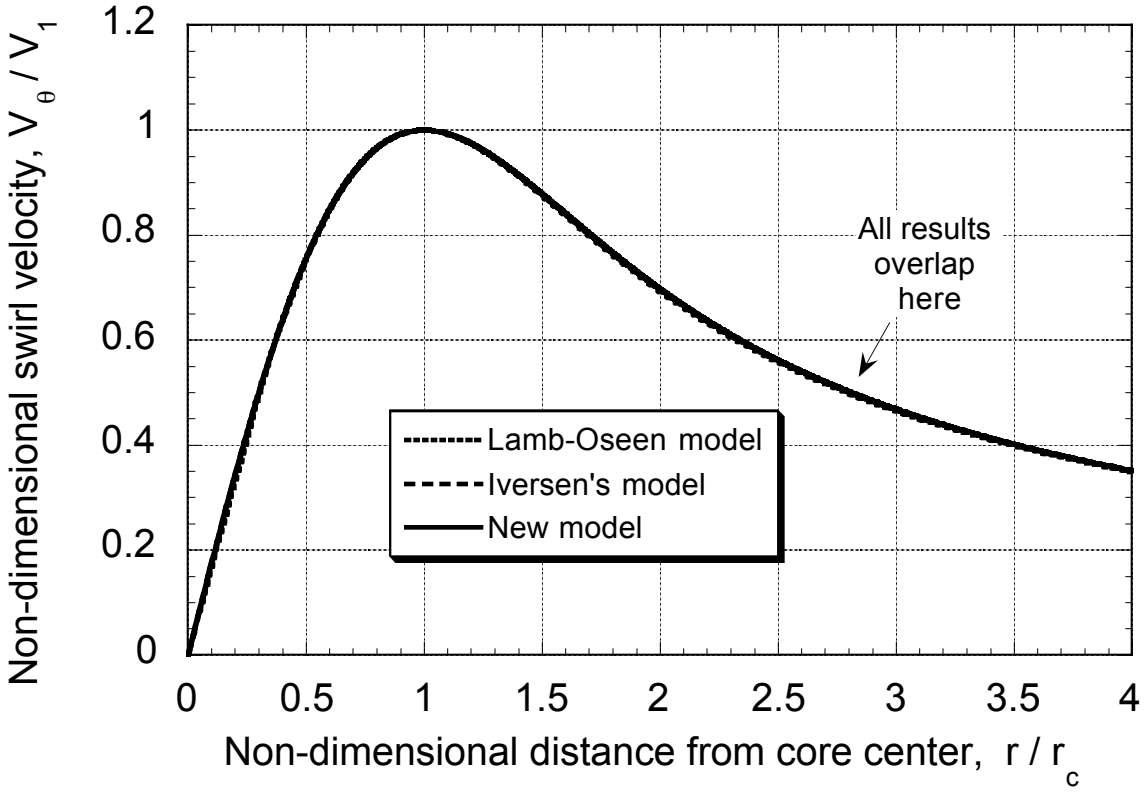

Figure 3.24: Predicted swirl velocity profiles at $Re_v = 200$.

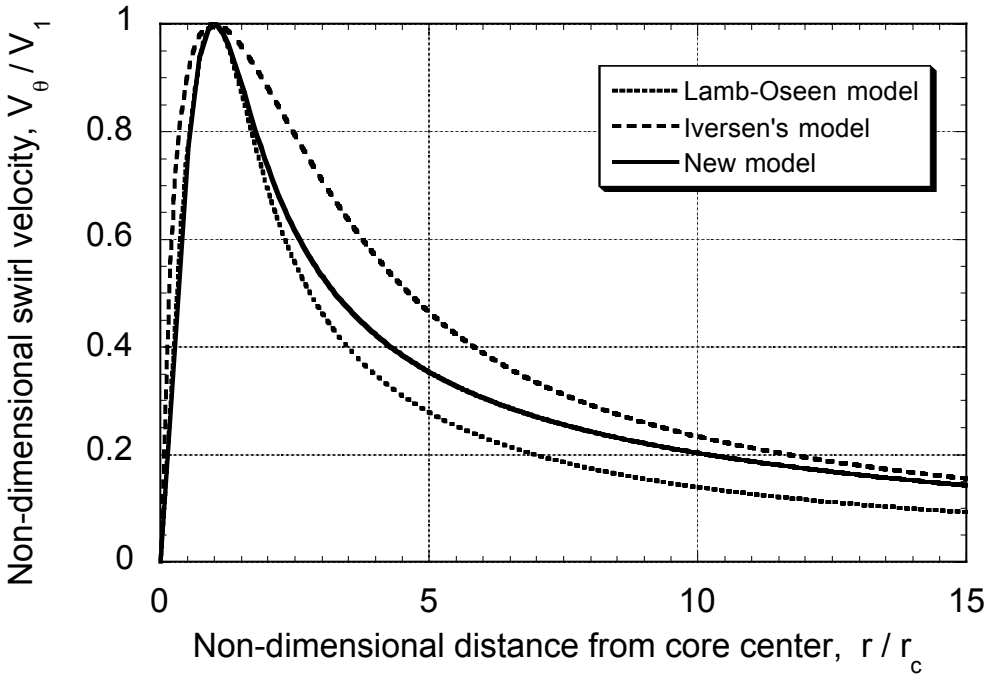

Figure 3.25: Predicted swirl velocity profiles at $Re_v = 25,000$.

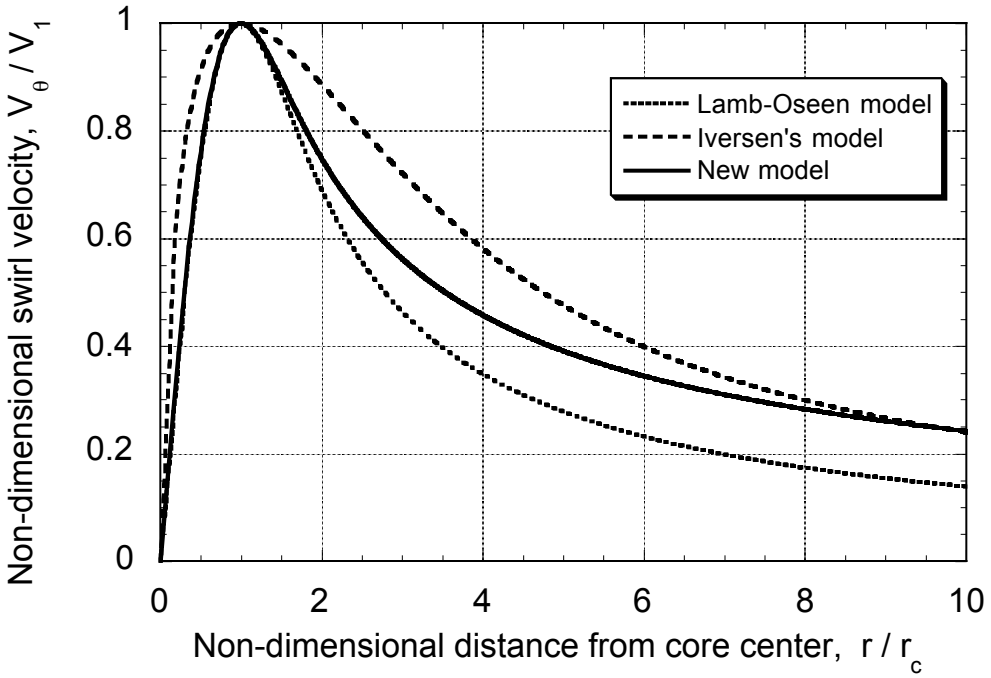

Figure 3.26: Predicted swirl velocity profiles at $Re_v = 48,000$.

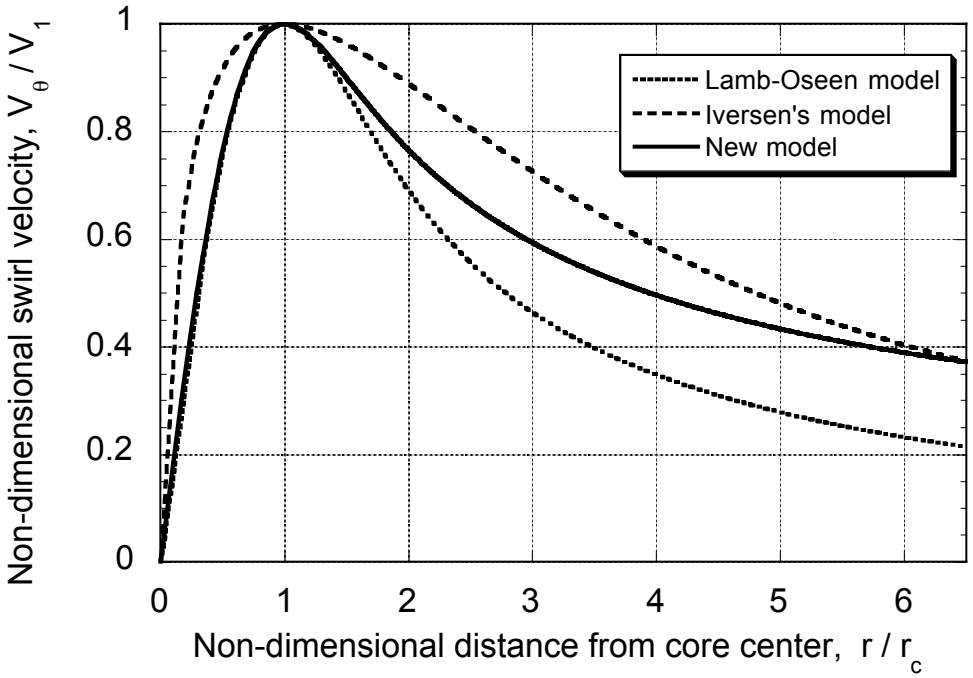

Figure 3.27: Predicted swirl velocity profiles at $Re_v = 75,000$.

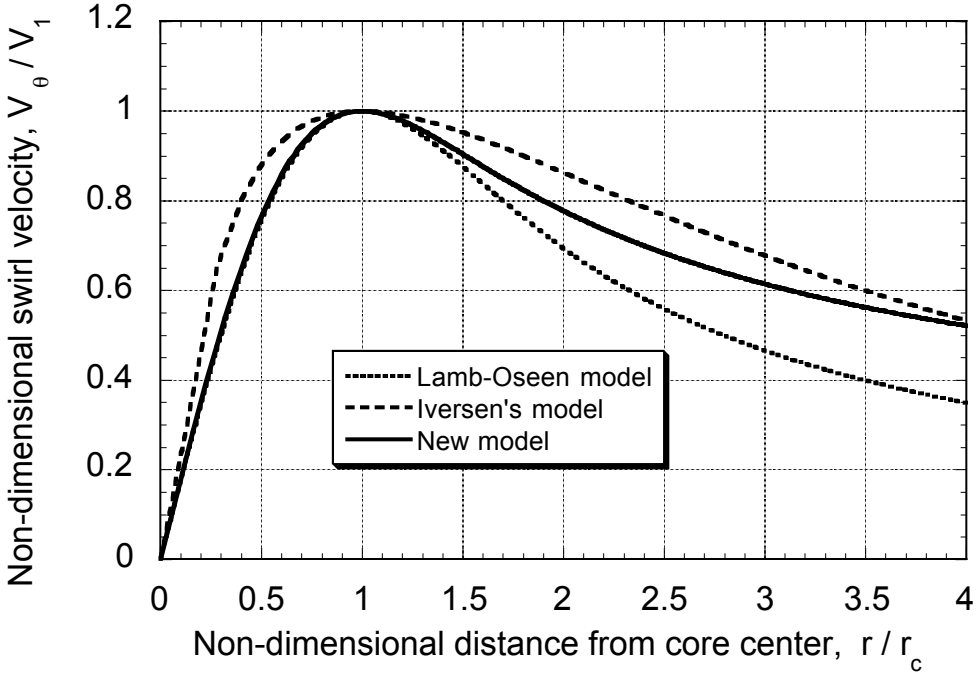

Figure 3.28: Predicted swirl velocity profiles at $Re_v = 1 \times 10^5$.

Figures 3.24 through 3.28 show the predicted distribution of swirl velocities at four different Reynolds numbers of 200, 25,000, 48,000 75,000 and 10^5 respectively. For reference, all the figures include the swirl velocity distribution from the laminar Lamb–Oseen model and the turbulent Iversen model. It can be observed from Fig. 3.24 that the predicted swirl velocity distribution from the new model (as well as Iversen model) lie on the constant viscosity results, indicating that all three models behave like the fully laminar model at low Reynolds numbers. As the Reynolds number increases, however, the eddy viscosity increases and the completely turbulent Iversen model shows a different profile to the laminar profile. The new model, which suppresses the turbulence near the vortex core axis depending on vortex Reynolds number, behaves like a laminar model near the core axis. As the radial distance increases, it slowly transitions to the completely turbulent flow model. The swirl velocity profiles obtained from the new model for a range of vortex Reynolds numbers is summarized in Fig. 3.29. It is apparent that the velocity profile changes with increasing vortex Reynolds number, and becomes closer to a more fully turbulent velocity profile at high vortex Reynolds numbers.

The Richardson number predicted by the new model along with the measurements from Ref. 38 is shown in Fig. 3.30. Again, this plot includes results from the Lamb–Oseen model and Iversen's model for reference. It is apparent that the new model behaves exactly the same way to the measurements by being laminar until a particular radial distance from the center of the vortex is reached (where the Richardson number is above the stratification threshold). It then slowly transitions to a completely turbulent profile at a large distance away from the center of the vortex. The ability of the model to predict three distinct regions of the tip vortex, and follows the measurements better when compared with the other existing vortex models.

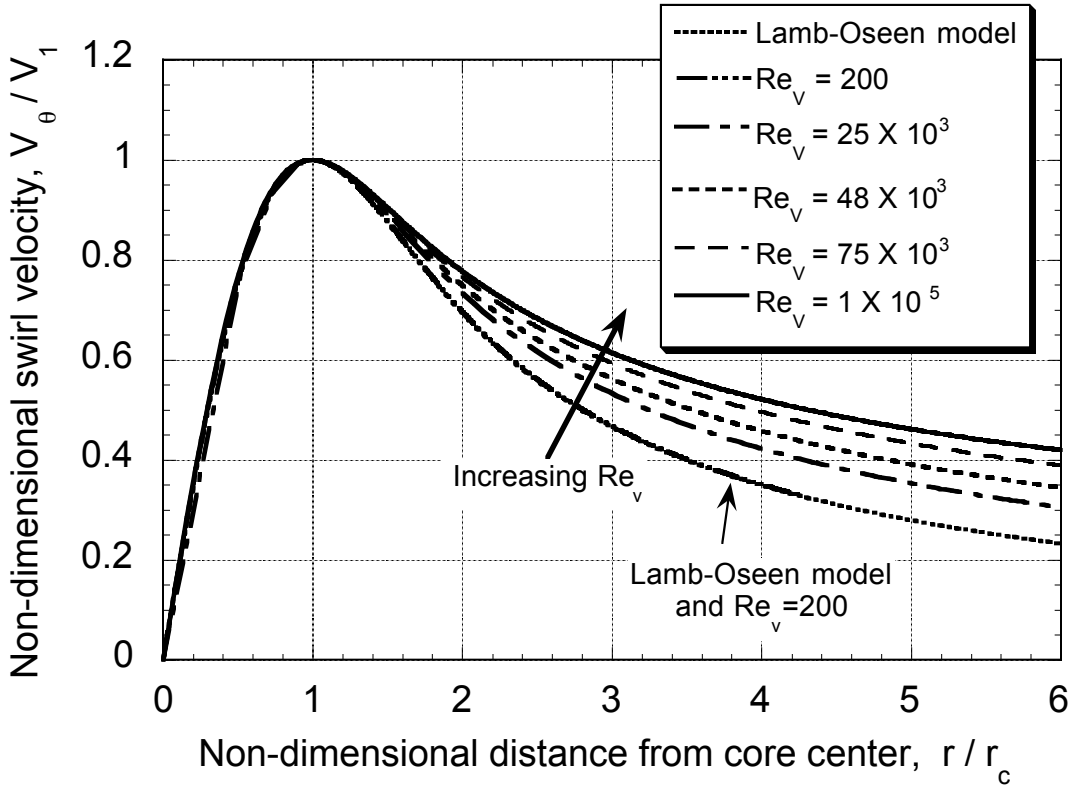

Figure 3.29: Predicted swirl velocity profiles at various vortex Reynolds numbers.

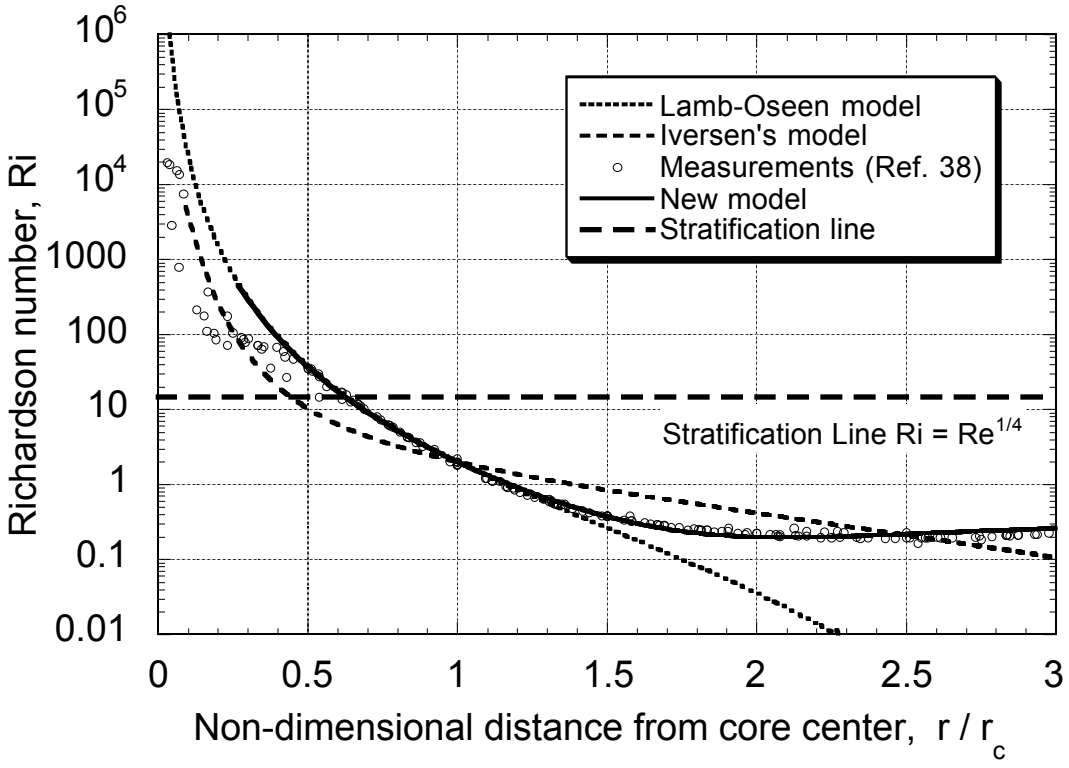

Figure 3.30: Variation of Richardson number for various models with non-dimensional radial distance, $Re_{\mathrm{v}} = 48,000$.

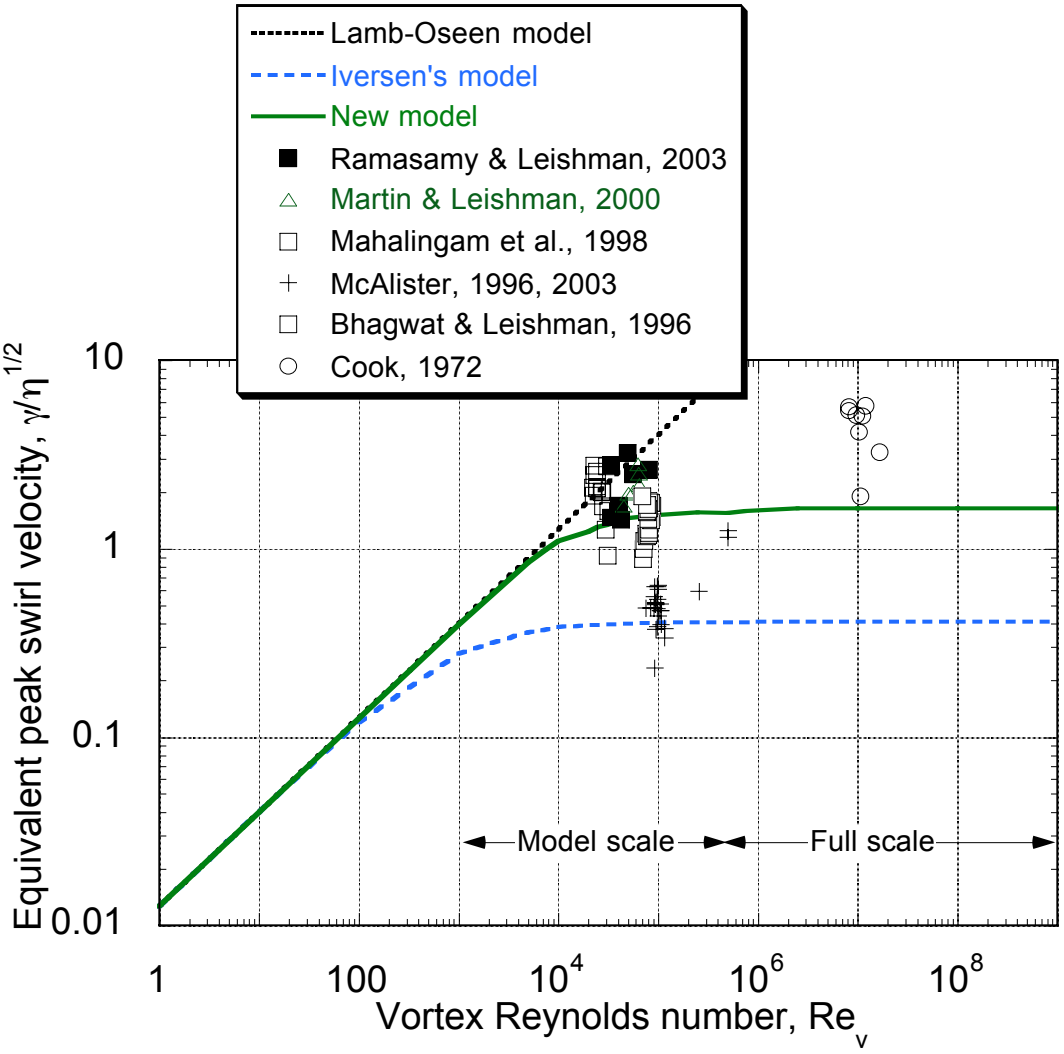

Figure 3.31: Variation of peak swirl velocity with vortex Reynolds number.

3.3.2 Peak Swirl Velocity and Core Radius

The variation of non-dimensional peak swirl velocity obtained from the numerical solution of Eq. 2.45 versus Reynolds number is shown in Fig. 3.31. Values from various experiments are included in this figure. It can be observed that the new model predicts the peak swirl velocity better than either of the Lamb–Oseen and Iversen models. Because this new model is developed on the basis Iversen model, both the new model and the completely turbulent Iversen model shows the tendency to asymptote to a constant value at high vortex Reynolds numbers. The asymptotic value, however, is different in both models because of the difference in the way the eddy viscosity varies in each case. It should be noticed that the peak swirl velocity V_1 for large Reynolds number is proportional to ${\Gamma_1}^{1/2}\ t^{1/2}$, which is independent of Reynolds number.

The variation of peak swirl velocity and core radius with wake age for various vortex Reynolds numbers is shown in Figs. 3.32 and 3.33, respectively. It can be seen that as the vortex Reynolds number increases the rate at which the peak swirl velocity reduces with increasing wake age. Similarly, the vortex core size increases rapidly with increasing wake age for high vortex Reynolds numbers. This is important because a small change in the strength or the size of the vortex can have a significant impact on predicting the unsteady airloads and propagated noise of helicopter rotors.

3.3.3 Core Growth

The ratio of apparent to actual viscosity for the new model can be used to determine the growth rate of the vortex core. The similarity variable $\overline{\eta}$ at the core radius is given by

$$\overline{\eta}_1 = \frac{{r_c}^2}{4{\alpha_{\text{new}}}^2 \gamma_v t}$$

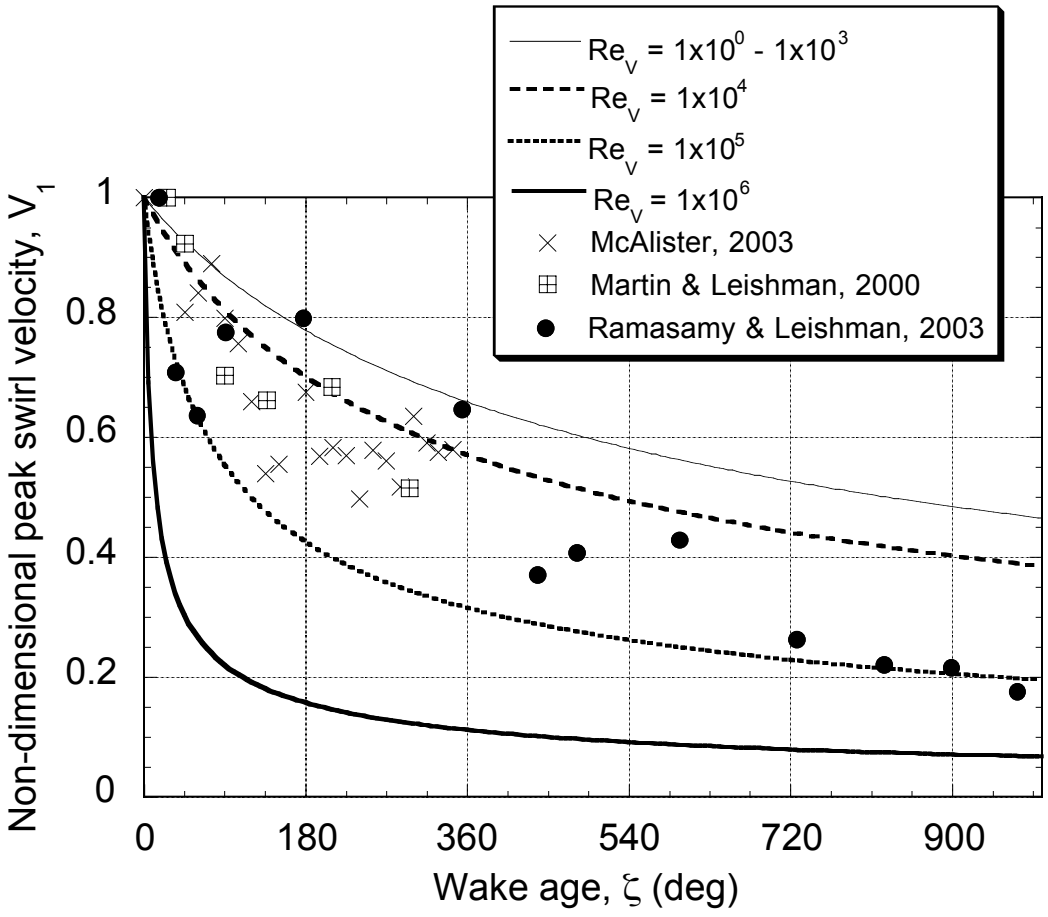

Figure 3.32: Variation of peak swirl velocity with wake age for various vortex Reynolds numbers.

i.e.,

$$\begin{aligned} {r_c}^2 &= 4\gamma_v {\alpha_{\text{new}}}^2 \overline{\eta}_1 t = \frac{4}{2\pi}(Re_{\text{v}}\nu){\alpha_{\text{new}}}^2 \overline{\eta}_1 t \\ &= 4\left[\frac{Re_{\text{v}}\ {\alpha_{\text{new}}}^2 \overline{\eta}_1}{2\pi}\right]\nu t \end{aligned} \tag{3.26}$$

From the Squire model

$${r_c}^2 = 4\alpha_L \delta \nu t \tag{3.27}$$

where α_L is Lamb's constant ($\alpha_L = 1.25643$). By comparing Eqs. 3.26 and 3.27

$$\alpha_L \delta = \frac{Re_{\text{v}} {\alpha_{\text{new}}}^2}{2\pi}\left[\frac{\Gamma_{v\text{Lamb}}}{V_{1\text{new}}}\right]^2$$

where $V_{1\text{new}}$ is the peak swirl velocity obtained from the new model at a given vortex Reynolds number. This means that

$$\delta = \frac{Re_{\text{v}}\ {\alpha_{\text{new}}}^2}{2\pi\alpha_L}\left[\frac{\Gamma_{v\text{Lamb}}}{V_{1\text{new}}}\right]^2 \tag{3.28}$$

A plot showing the variation of δ with Reynolds number for the new model along with the Lamb–Oseen and Iversen models (using rotating-wing measurements) is given in Fig. 3.34. Clearly the completely turbulent Iversen model over predicts the core growth. Also, the laminar Lamb–Oseen model under predicts the core growth because molecular diffusion is the only source of momentum transport. However, the new model predicts the core growth better than either of the Lamb–Oseen and Iversen's models. It can also be observed that at low vortex Reynolds numbers, both the new model and the Iversen's model approach the laminar solution ($\delta = 1$).

3.3.4 Combining Filament Strain and Flow Rotation Effects

Developing a comprehensive tip vortex model that combines vortex filament stretching effects, flow rotation effects, and vortex Reynolds number effects for numerical

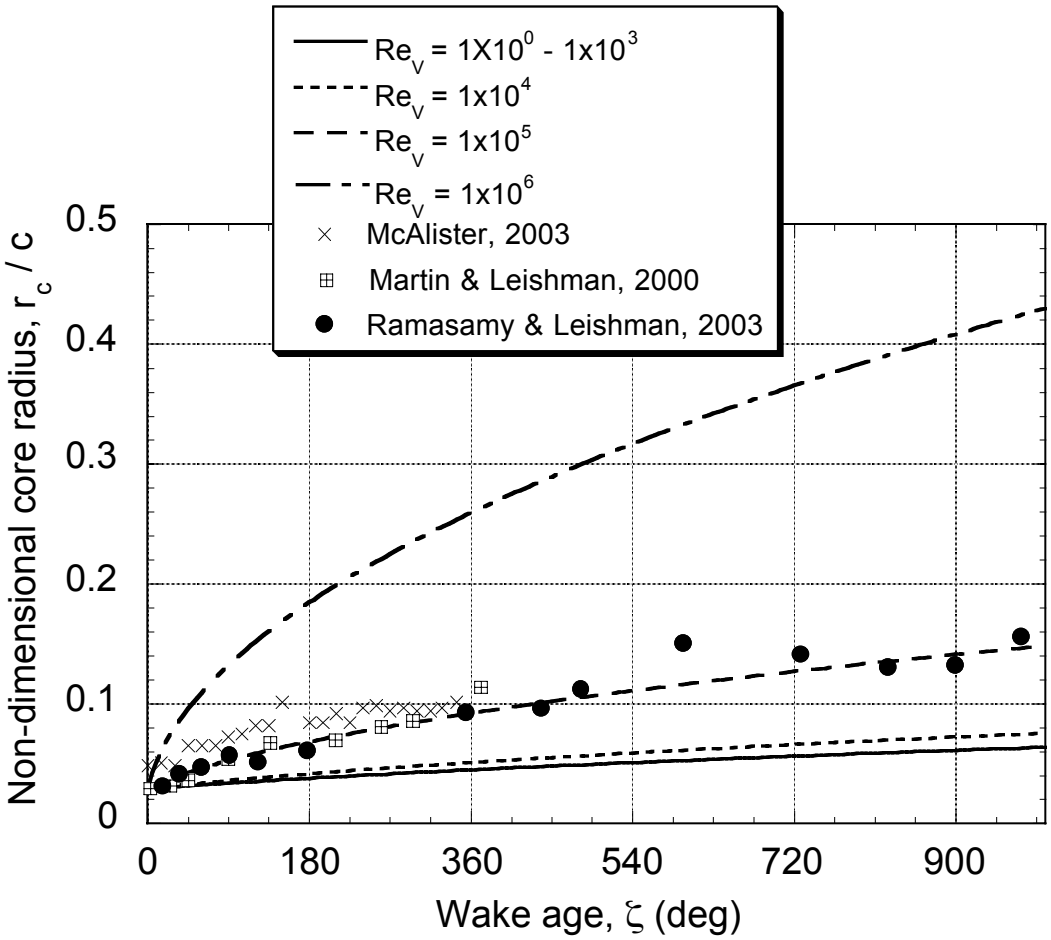

Figure 3.33: Variation of vortex core radius with wake age for various vortex Reynolds numbers.

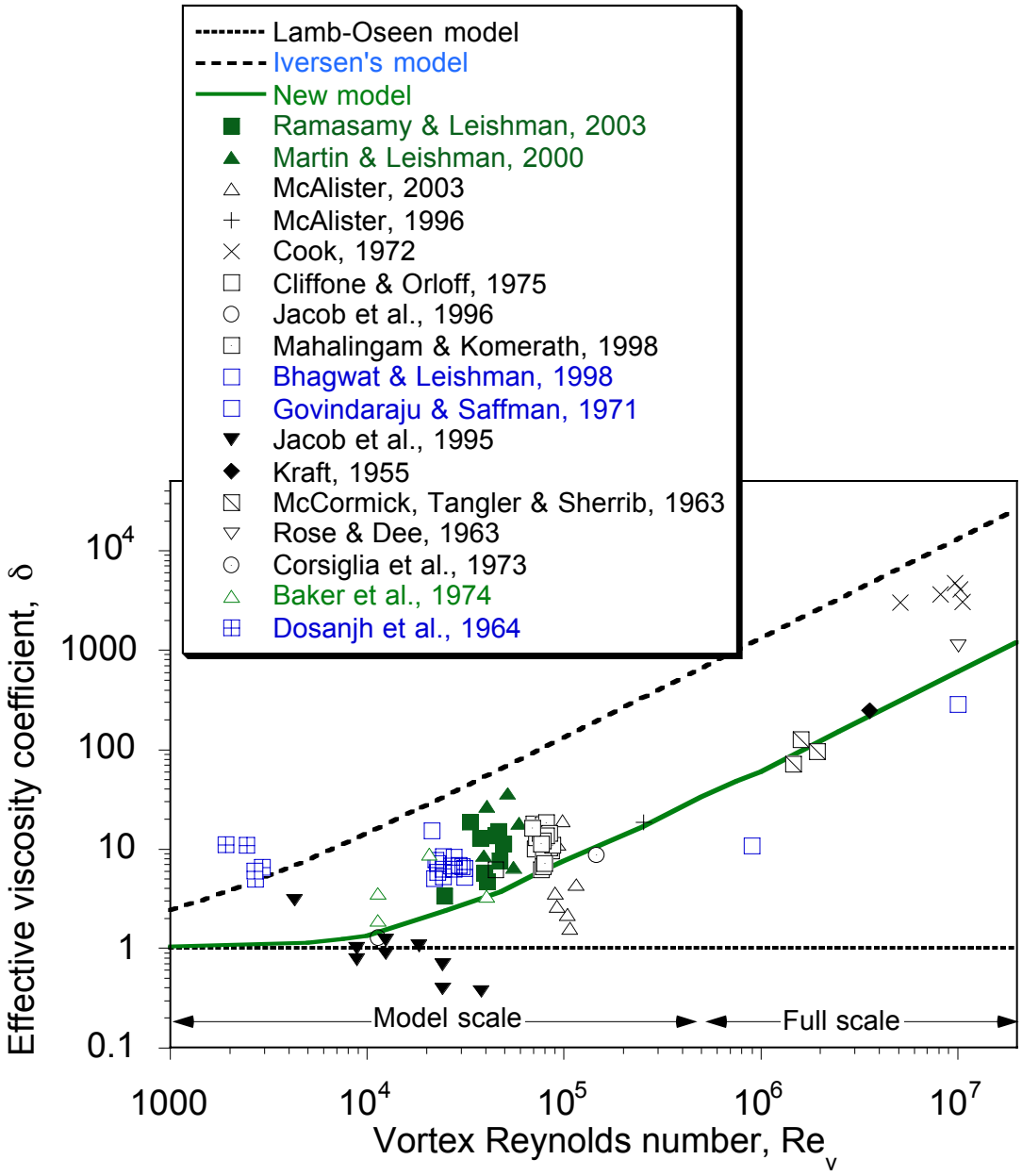

Figure 3.34: Variation of δ with vortex Reynolds number.

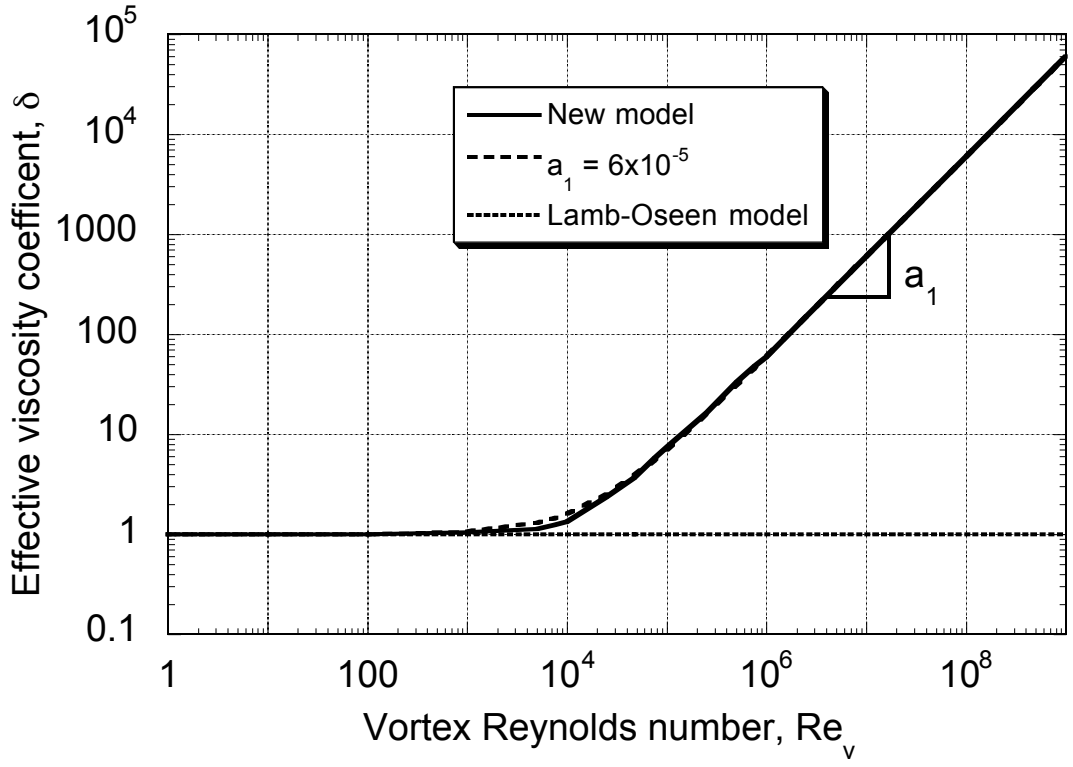

Figure 3.35: Variation of δ with vortex Reynolds number to determine a_1.

applications is one of the primary objectives of this work. It would be ideal to have the combined model in algebraic form to apply it directly to any numerical applications such as free vortex-wake. Algebraic models have gained popularity over the past few years, as mentioned earlier in Section 1.6, because of their low computational cost. Examples of such models include Scully & Sullivan [112, 113], Kaufmann [92], and a family of vortex models suggested by Vatistas [91, 114]. The success of these algebraic models that were derived from the N–S equations was motivation for developing an engineering model for the growth rate of the tip vortices. Combining the generalized transitional model (Eq. 2.50) that includes flow rotation effects and vortex Reynolds number effects within the strain model (Eq. 3.14) requires a comparison of a particular property of the tip vortex that is common to both models.

The growth rate of the vortex core is one of the most important properties of the tip vortex that largely depends upon the vortex Reynolds number. The rate of growth of the vortex core was found to vary between 10 for sub-scale to 1000 for full-scale flight conditions when compared with the constant viscosity, Lamb–Oseen type laminar growth rate [11, 13, 16, 59]. Besides vortex Reynolds number, this increased growth rate results from the presence of turbulence inside the vortex core. This is usually modeled in terms of eddy viscosity variation across the vortex [13, 14, 59]. Because the new generalized vortex model is also developed by modeling an eddy viscosity function that represents the turbulence structure present inside the vortex based on Richardson number, it would be ideal to compare the integral effects of the proposed eddy viscosity function that appears in the growth rate of the tip vortex with the core growth rate of the strain model.

By plotting δ from the Squire's eddy viscosity model as given by Eq. 2.11, i.e.,

using

$$\delta = 1 + \frac{a}{2\pi}\left(\frac{\Gamma_v}{\nu}\right) = 1 + a_1\,(\mathrm{Re}_v) \tag{3.29}$$

for various vortex Reynolds number against the δ variation predicted by the new model (as shown in Fig. 3.35) the constant a_1 (=$a/2\pi$) was determined to be 6×10^{-5}. This value of a_1 lies within the range suggested by Bhagwat & Leishman [101], as shown in Fig. 3.36.

This results is an added benefit of determining a unique value of a_1 that will help rotorcraft analysts in various applications. This, in turn, will result in better prediction of growth rate of the vortex in a physically correct manner and, therefore, help predict unsteady blade airloads and rotor noise to a higher level of fidelity. Notice that by having a unique value for a_1 from the generalized transitional vortex model, the effective eddy viscosity parameter δ now includes the effects of flow rotation on the turbulence present inside the vortex core, and is also a function of vortex Reynolds number.

Finally, the growth rate of the tip vortex core that takes into account the effects of vortex filament strain, flow rotation effects, and that is also a function of vortex Reynolds number can be written as

$$r_c(\zeta,\varepsilon) = \sqrt{r_0^2 + \frac{4\alpha\nu(1+a_1 Re_v)}{\Omega}\int_{\zeta_0}^{\zeta}\left[1+\varepsilon(\zeta)\right]^{-1} d\zeta} \tag{3.30}$$

where $a_1 = 6 \times 10^{-5}$.

The core growth predicted by the new model for different vortex Reynolds numbers is shown in Fig. 3.37. This include vortex Reynolds numbers that corresponds to a full-scale, $1/7^{th}$-scale, $1/15^{th}$-scale UH-60 rotor, along with a completely laminar Lamb–Oseen model for reference. Because there are no full-scale UH-60 measurements available, vortex measurements from various available sources at different

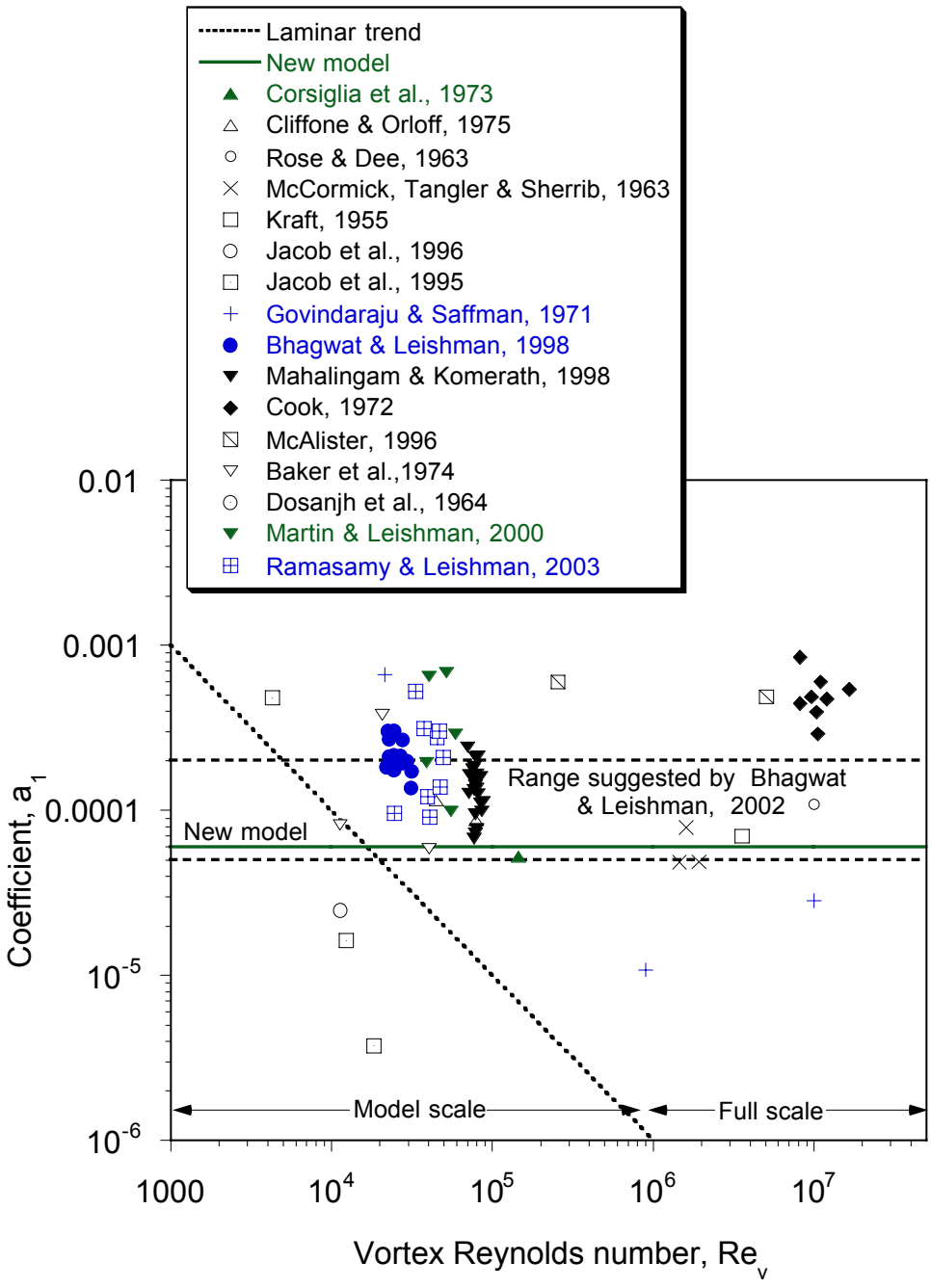

Figure 3.36: Effective viscosity parameter, a_1, as a function of vortex Reynolds number.

vortex Reynolds number are shown in the figure. It can be observed that the core size predicted by the new model correlates well with the measurements that are performed at different scales (different vortex Reynolds numbers). An increase in the vortex Reynolds number corresponds to an increase in the overall extent of turbulence present inside the tip vortices and, therefore, increases the diffusion of vorticity and so increases the turbulent growth rate of the tip vortex cores. It can be observed that for full-scale flight conditions the vortex core size grows up to 30% of the blade chord within 360° of wake age, and up to 40% in two rotor revolutions. In all cases a logarithmic growth rate can be observed at older wake ages. The model reduces to the laminar Lamb–Oseen model for very low values of vortex Reynolds numbers ($Re_\nu < 1000$), as expected.

The importance of vortex filament strain on the growth properties of tip vortices can be illustrated with reference to the viscous development of a rectilinear vortex at a particular vortex Reynolds number. The effects on the filaments were examined as a function of prescribed strain rate that is defined by $V_\varepsilon = d\varepsilon/dt$. Figure 3.38 shows the growth rate of the rectilinear vortex filament at a vortex Reynolds number of 5×10^4, which is a representative value of most model-scale rotor measurements. By applying a uniform strain rate of the form

$$V_\varepsilon(\psi) = \text{constant} \tag{3.31}$$

on the rectilinear vortex filaments, the predicted core growth is shown in also shown in Fig. 3.38. It can be observed that the growth rate of the vortex cores alter significantly depending on whether the filament undergoes positive strain or negative strain. An application of positive filament strain results in a reduced core size. This is expected because when the filament length increases to infinity, the core size would approach zero to conserve circulation. This infinite increase in length of tip vortex filaments

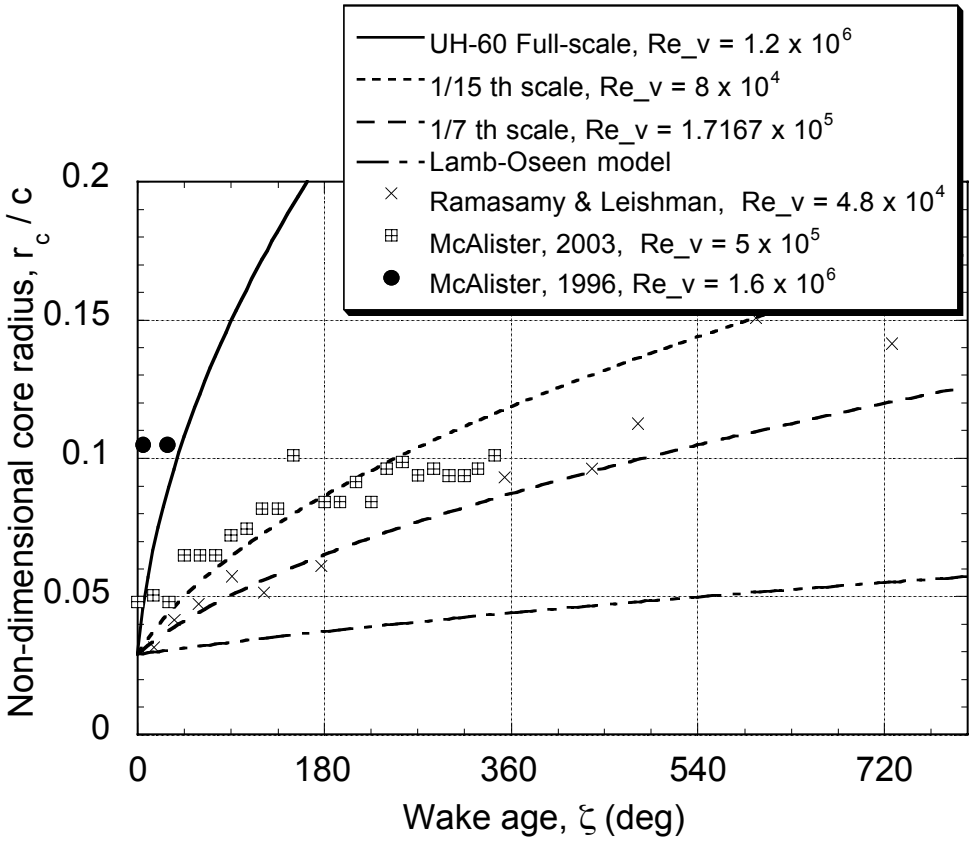

Figure 3.37: Core growth predicted by the new vortex model at different vortex Reynolds numbers.

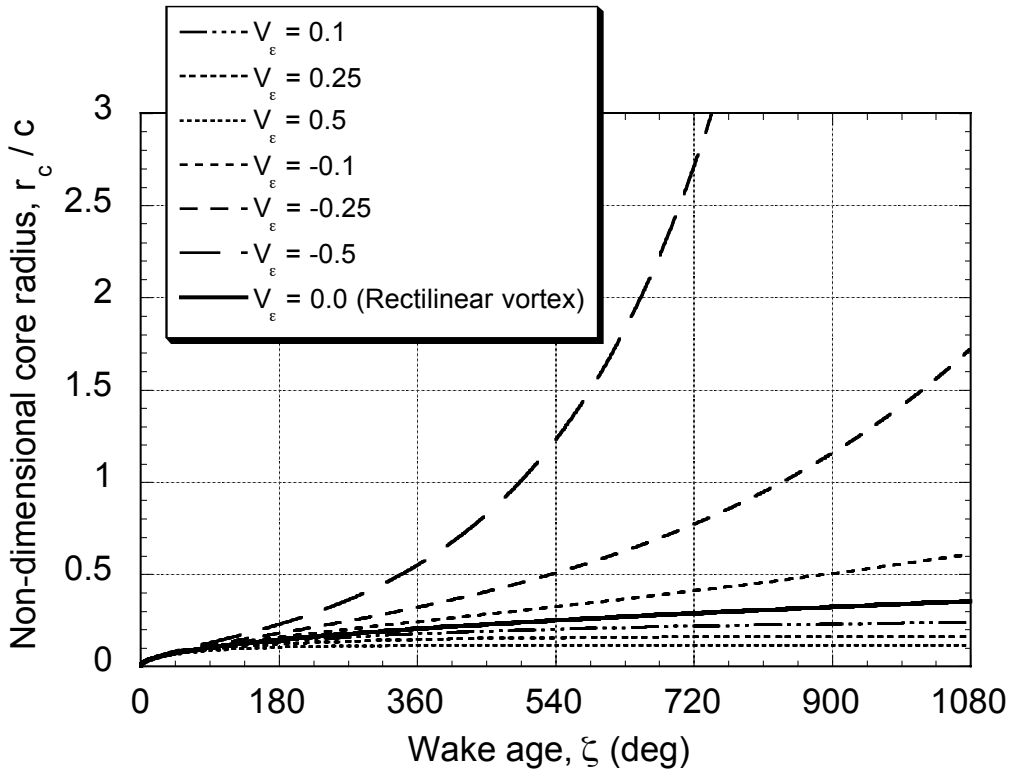

Figure 3.38: Variation of core growth predicted by the new model for different values of uniform strain rates at $\mathrm{R}e_v = 4.8 \times 10^4$.

results in the classical Lamb–Oseen model. This also suggests that the effects of stretching when a filament develops in a three-dimensional flow field can counter the effects of diffusion by producing a notable reduction in the core size. Conversely, a negative filament strain results in an increased core growth rate, suggesting that the effects of strain can enhance the effects of diffusion.

The core growth predicted by the new model for the measured strain rates obtained from current set of measurements is shown in Fig. 3.39. This figure also includes the predicted core growth of rotor tip vortices for twice the measured strain rates as well as half the measured strain values. It can be observed that the core growth predicted by

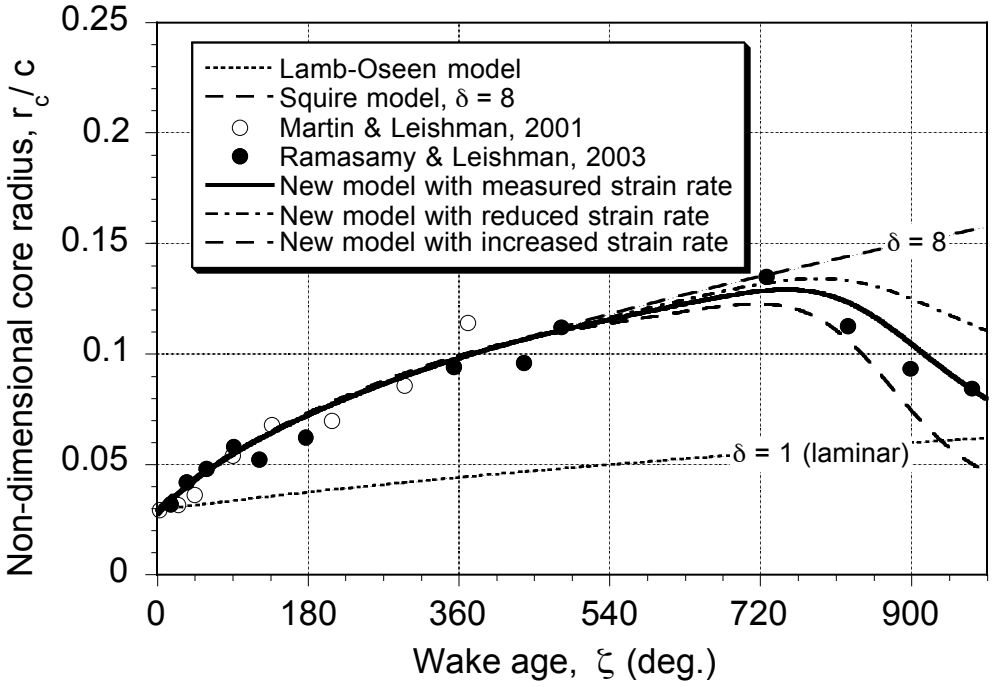

Figure 3.39: Core growth predicted by the new model for measured values of strain rates.

the new model, for the value of δ that would appropriately represent the core growth with pure diffusion alone, correlated well with the experimental measurements. As the tip vortices approach the ground plane, the high velocity gradients associated with the flow stretched the vortex filaments radially resulting in a reduction of vortex core size. It can be observed that an increase or decrease in strain rate will alter the core growth prediction significantly. These changes in core size as the vortices convect and strain in the rotor wake can significantly alter the resulting wake geometry and, therefore, the prediction of BVI effects. Being algebraic in nature, the comprehensive core growth model can be directly applied to any numerical application for prediction of airloads, vibration, and noise. However, developing an algebraic expression for the swirl velocity profile for the generalized transitional vortex model is beyond the scope of this dissertation and is left for future work.

Chapter 4

Conclusions

This final chapter discusses the conclusions that have been derived from both the experimental measurements and theoretical development made in the current study. The overall purpose of the present work was to better understand the various properties of helicopter blade tip vortices and effects that may affect their evolution. Filament strain is one such effect, and is often neglected in explaining the physics of rotor flow fields. This is despite the fact that the magnitude of the strain found in rotor wakes is large enough to have substantial effects on the growth properties of the tip vortices. Measurements that are made in both sub-scale and full-scale helicopter rotor experiments always inherently include the effects of vortex filament strain. Isolating and quantifying the effects of strain on the development of the tip vortices becomes essential for developing better vortex models for rotor analyses. Also, most existing measurements are made on sub-scale model rotors, where the vortex Reynolds number is smaller by orders of magnitude when compared to full-scale flight conditions. As a result, tip vortex models that may be developed based on measurements made on sub-scale rotor models may not predict accurately the physics of tip vortex flow at full-scale flight conditions. Similarly, the effects of flow rotation on the turbulence

present inside the tip vortex and, therefore, its evolution has not previously been taken into account in the development of vortex models for helicopter rotor applications. All existing vortex models have assumed either completely laminar or completely turbulent flows, even though various measurements and flow visualization images suggest a multi-region vortex model.

4.1 Summary of Contributions

An experiment was conducted in an attempt to isolate and quantify the effects of vortex filament strain on the evolution of helicopter rotor blade tip vortices. The work included both flow visualization and high resolution, three-dimensional LDV measurements. A known strain field was imposed in the rotor flow field by placing a ground plane parallel to the rotor plane. The presence of the ground plane stretched the tip vortex filaments as the wake approached the solid boundary. Measurements were made to quantify the interdependence of the filament strain and diffusion of the tip vortices. The measurements and flow visualization images were later used to understand the effects of flow rotation on the turbulent structures present inside the tip vortices. This allowed the development of a comprehensive tip vortex model that was a function of vortex Reynolds number. This model took into account the effects of vortex filament strain and flow rotation effects on the evolution of blade tip vortices.

Chapter 1 has discussed the work done in the past, both experimentally and theoretically, to understand the various properties of lift generated tip vortices. The special challenges involved in making measurements in a helicopter rotor flow field were also discussed in detail. Chapter 2 has explained the approach that was followed in both making measurements and in developing a mathematical model for rotor blade tip

vortices from the N–S equations. The first section (experimental approach) included detailed explanation of the rotor facility that was used, the technique used to strain the vortex filaments, the steps that are involved in making flow visualization images, the three-dimensional LDV measurements, and the post processing procedures in obtaining the final results from the measurements. A section explaining the alignment procedure of the 3-component laser was also given. Aperiodicity (the random movement of the tip vortex cores at a given wake age) was analyzed and a procedure was used to correct the measurements. The second part (theoretical approach) discussed, in detail, the effects of flow rotation on the turbulent structures present inside the tip vortices. This was followed by a description of the process followed in developing a new model for transitional blade tip vortices that is a function of vortex Reynolds number.

The results that were obtained both from the experiment and from the vortex model that was derived from the Navier-Stokes equations were given in Chapter 3. These measurements helped to quantify the interdependence of filament straining and the viscous/turbulent diffusion of the tip vortices. This understanding was later used, in conjunction with other vortex measurements, to develop an mathematical model for core growth of the tip vortices that accounts for the combined effects of both viscous diffusion and straining.

Images of the tip vortices from the laser sheet flow visualization technique suggested a multi-region vortex model. The tip vortex appeared to be made of three regions: 1. An inner laminar region, where there is no interaction between adjacent layers of fluid, 2. A transitional region with eddies of different sizes, and 3. A fully turbulent outer region. Self-similar velocity profiles were obtained by normalizing the measured swirl velocity profiles obtained at different wake ages by core radius

and peak swirl velocities at the corresponding wake ages. The measurements seemed to follow the fully laminar Lamb–Oseen vortex model for a particular distance from the center of the vortex, slowly transitioning towards the fully turbulent Iversen-like model.

As a result of these observations, a generalized vortex model was developed from the N–S equations that included the effects of flow rotation on turbulence present inside the tip vortex. The model was developed using an intermittency function invoking the concept of local Richardson number. This function represented the eddy viscosity variation across the vortex, and accounted for the effects of flow rotation on turbulence development. One hypothesis used was that the vortex cannot develop or sustain any turbulence until the local Richardson number falls below a threshold value. The new model was able to demarcate these three distinct regions of the vortex, and is consistent with flow visualization and velocity field measurements. It is shown that the vortex velocity profile predicted by the new model is initially laminar until a particular radial distance from the vortex core axis, and then slowly transitions to a fully turbulent region away from the center of the vortex.

4.2 Conclusions

1. The experimental procedure designed to stretch the tip vortex filaments was found to be successful in imposing a strain field on the developing rotor wake. The magnitude of the filament strain that is estimated from the measured spatial locations was found to be sufficiently large when the tip vortex filaments were closer to the ground plane.

2. The effect of the vortex filament stretching on the development of tip vortices

was found to counter the effect of diffusion, depending on the nature and magnitude of strain exerted on the vortex filaments. A large positive strain of the tip vortex filaments, (as it occurred near the solid boundary) was found to balance the effects of diffusion on the growth properties of tip vortices by reducing the size of the vortex core. A mathematical model for the effects of stretching was used to correct the measurements, which brought the results into agreement with what would be expected on the basis of diffusion alone.

3. As a byproduct of the process of stretching the vortex filaments, it allowed their properties to be measured to much older wake ages than would otherwise have been possible. Corrected results for zero strain field were used to compare with other measurements, and to augment previous correlations where measurements could not be made at older wake ages. The new results were used to help support a more general vortex model valid for older wake ages that is suitable for use in a variety of aeroacoustic applications.

4. An engineering model for the core growth of the tip vortex was suggested that combined the effects of diffusion and strain on the vortex core growth. The empirical constants of this model have been derived based on an average of various available measurements that have documented the viscous core growth of trailing vortices.

5. The newly developed, vortex Reynolds number dependent, generalized model for transitional blade tip vortices that takes into account the effects of flow rotation on their development was found to correlate well with the experimental measurements. The new model clearly demarcates three distinct regions of tip vortex. The core growth predicted by the new model at different vortex

Reynolds numbers was found to agree well with available measurements from various sources.

6. The Reynolds number dependency of the model helps understand trends shown in measurements that were made using both sub-scale models and full-scale rotors. The swirl velocity and circulation profiles obtained from the new model changes with an increase in vortex Reynolds number. It is shown that the model reduces to a constant viscosity laminar Lamb–Oseen model at very low Reynolds numbers.

7. It was found that the increase in vortex Reynolds number corresponded to an increase in turbulence present inside the vortex, and would result in an increased core growth rate of the vortex as it ages. This would also lead to a more rapid reduction of peak swirl velocity with increasing time. The peak swirl velocity was predicted to be independent of Reynolds number at large vortex Reynolds numbers. This is consistent with Iversen's model and also with measurements available from other sources.

8. An equivalent average eddy viscosity distribution (first suggested by Squire) was compared with the assumed eddy viscosity variation of the new model to develop a new comprehensive (albeit approximate) vortex Reynolds number dependent core growth model that combines both the effects of vortex filament strain and flow rotation on the evolution of tip vortices. Being algebraic in nature, this model can be directly applied to any numerical application for predictions of rotor airloads, vibration levels, and noise.

4.3 Recommendations for Further Research

4.3.1 Measurement Techniques

Improvement in the optics and instruments directly translate into higher quality measurements. The following are few suggestions that are proposed for further improvements in the measurement techniques.

1. Installing a micrometer to adjust the incident angle of the transmitting probes. Currently, the probes are mounted on a swivel head to be adjusted manually while aligning beams. As the transmitting probes are at a considerable distance away from the tip of the blade, where all 6 beams coincides, a small change in the angular position of the probe can result in large deviation from the coincident point. The presence of micrometer will reduce the time consumed by the alignment procedure.

2. Mounting the beam profiler on a stage-micrometer for improved accuracy.

3. Currently, the power of violet beams are much smaller compared with the other two beams: green and blue. An additional laser can be used to produce the violet beam pair so that the power on all three channels are equal.

4.3.2 Tip Vortex Analysis

Even though the developed model that takes into account the effects of vortex filament strain, the effects of flow rotation, and the effects of vortex Reynolds number is developed, the complete understanding of the flow inside the tip vortices is far from complete. There are numerous issues that need to be analyzed. The following are a few suggestions for further research.

1. The effects of strain on the axial velocity component of tip vortices is still not fully quantified. Axial velocity measurements should be made in the wake of a hovering rotor and should be analyzed with the measurements that are made in a known strain field. The same experimental set up that is used in this work could be used in making those measurements.

2. The new generalized transitional vortex model was developed based on an eddy viscosity function with its empirical constants, in part, derived from the mean velocity measurements. However, it would be ideal to have a three-dimensional turbulence measurements in the rotor flow field to validate the model. In this case, it should be noted that there are 6 components of shear stress whereas the new model just uses only one ($\overline{uv}$) in developing the model.

Appendix A

Aperiodicity Correction

Aperiodicity is the inherent random movement of the phase-resolved spatial locations of the vortex cores inside the rotor wake. Measurements of aperiodicity were made using laser light-sheet illumination of the seeded flow. A laser pulse duration on the order of nanoseconds was achieved using an Nd:YAG laser. The laser was synchronized to the rotor so that the aperiodicity of the vortex core position could be measured at a fixed wake age. A CCD camera with a micro lens acquired the images, which were digitized and the vortex positions quantified with respect to a calibration grid.

Various methods have been proposed for correcting measurements for aperiodicity or "wandering" (Refs. 69, 71, 81, 100). The method of Leishman [69] is used here, and accounts for an arbitrary velocity distribution and anisotropic variations in aperiodicity. The procedure that was developed by Leishman [69] to correct the swirl velocity profiles for aperiodicity of tip vortices in rotor flow fieldt is given below.

Consider the two-dimensional aperiodic motion of a tip vortex at a given wake age, ζ. Define the LDV measurement location, which is fixed with respect to the rotor axes system, as (r_p, z_p). The current location of the vortex core axis relative to

a rotor based axis system is assumed to be (r_v, z_v) - see Fig. A.1. The velocity field measured at (r_p, z_p) at a wake age ζ will be functions of r and z and the position of the measurement point relative to an axis at the center of the vortex, i.e.,

$$V(r, z, \zeta) = V(r_p - r_v, z_p - z_v, \zeta) \tag{A1}$$

Over a sufficiently large number of rotor revolutions, the aperiodicity of the vortex location relative to the measurement point can be described by using a probability density function (p.d.f.), say $p = p(r_v, z_v, \zeta)$. Following Devenport et al. [81], it may be initially assumed that the aperiodicity is normal (Gaussian) so that a joint normal p.d.f. can be defined as

$$p(r_p, z_p, \zeta) = \frac{1}{2\pi\sigma_r\sigma_z\sqrt{1-e^2}} \exp\left[\frac{-1}{2(1-e^2)}\left(\frac{r_v^2}{\sigma_r^2} + \frac{z_v^2}{\sigma_z^2} - \frac{2\,e\,r_v z_v}{\sigma_r\sigma_z}\right)\right] \tag{A2}$$

where $\sigma_r = \sigma_r(\zeta)$ and $\sigma_z = \sigma_z(\zeta)$ are the measured r.m.s. aperiodicity amplitudes in the radial and axial directions at each wake age, respectively, and $e = e(\zeta)$ is the correlation coefficient. Using Eq. A2, the actual or measured velocity $\overline{V}(r_p, z_p, \zeta)$ can then be determined by convolution where

$$\overline{V}(r_p, z_p, \zeta) = \int\!\!\int_{-\infty}^{\infty} V(r_p - r_v, z_p - z_v, \zeta)\;\; p(r_v, z_v)\;\; dr_v\, dz_v \tag{A3}$$

The discrete equivalent of Eq. A3 is

$$\overline{V}(r_p, z_p, \zeta) = \sum\sum V(r_p - r_v, z_p - z_v, \zeta)\;\; p(r_v, z_v)\;\; \Delta r_v\, \Delta z_v \tag{A4}$$

This latter equation is solved by re-expressing V in a Cartesian coordinate system, and the summations are taken over length scales that are at least one order of magnitude larger than σ. An advantage of the numerical solution using Eq. A4 is that very general velocity profiles such as the non-axisymmetric tangential profiles generally found in

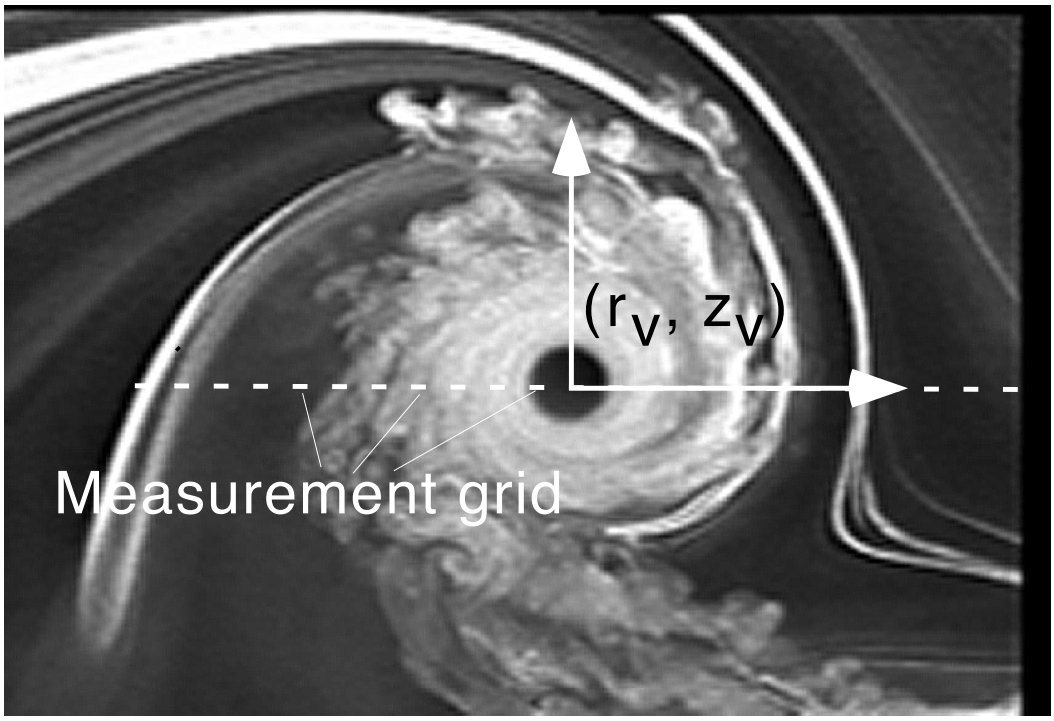

Figure A.1: Flow visualization image of the vortex core, showing the measurement grid and the coordinate system relative to the vortex axis.

rotor wakes can be solved to establish actual quantitative effects of aperiodicity on the results.

Starting from an initial (assumed) tangential velocity profile without any aperiodicity, a profile with the effects of aperiodicity can be obtained numerically by using Eq. A4. By comparing in point by point sense this new profile with a specified amplitude of aperiodicity to the actually measured velocity profile, then a correction can be applied and a new guess made at the true tangential velocity. The process can be repeated using Eq. A4 until convergence is obtained, which is typically within a few iterations. This technique, therefore, yields an estimate of the true velocity field based on the measured velocity field and measurements of the aperiodicity of the tip vortex locations. Figure A.2 shows the swirl velocity profile before and after correcting for the aperiodicity effects. It can be seen that the corrected profile shows higher peak swirl velocity and a decreased core radius when compared to the uncorrected profile.

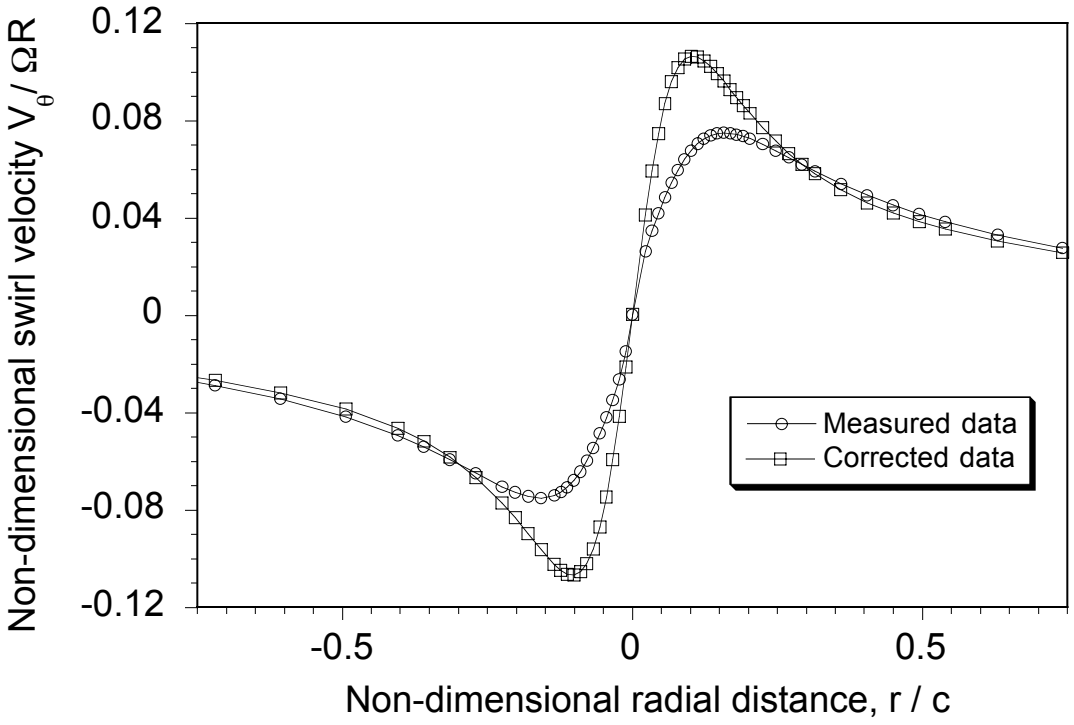

Figure A.2: Example of a swirl velocity profile before and after correcting for aperiodicity of the vortex position.

Bibliography

[1] Leishman, J. G., *Principles of Helicopter Aerodynamics,* Cambridge University Press, New York, 2000.

[2] Bacon, D. L., "The Distribution of Lift Over Wing Tips and Ailerons," NACA TN 161, 1924.

[3] Green, S. J., and Acosta, A. J., "Unsteady Flow in Trailing Vortices," *Journal of Fluid Mechanics*, Vol. 227, 1991, pp. 107–134.

[4] Munk, M. M., "Note on Vortices and Their Relation to the Lift of Airfoils," NACA TN 184, 1924.

[5] Zeman, O., "The Persistence of Trailing Vortices: A Modeling Study," *Physics of Fluids*, Vol. 7, No. 1, January 1995, pp. 135–143.

[6] Sarpkaya, T., "Decay of Wake Vortices of Large Aircraft," *AIAA Journal*, Vol. 36, No. 9, September 1998, pp. 1671–1679.

[7] McAlister, K., "Rotor Wake Development During the First Rotor Revolution," American Helicopter Society 59th Annual National Forum, Phoenix, Arizona, May 6–8 2003.

[8] Martin, P. B., Pugliese, G., and Leishman, J. G., "High Resolution Trailing Vortex Measurements in the Wake of a Hovering Rotor," American Helicopter Society 57^{th} Annual National Forum, Washington, DC, May 9–11, 2001.

[9] Ciffone, D. L., and Orloff, K. L., "Far-Field Wake-Vortex Characteristics of Wings," *Jorunal of Aircraft*, Vol. 12, No. 5, May 1975, pp. 464–470.

[10] Baldwin, B. S., Chigier, N. A., and Sheaffer, Y. S., "Decay of Far-Flowfield in Trailing Vortices," *AIAA Journal*, Vol. 11, No. 12, December 1973, pp. 1601–1602.

[11] Dosanjh, D. S., Gasparek, E. P., and Eskinazi, S., "Decay of a Viscous Trailing Vortex," *The Aeronautical Quarterly*, Vol. 3, No. 3, 1962, pp. 167–188.

[12] Govindraju, S. P., and Saffman, P. G., "Flow in a Turbulent Trailing Vortex," *Physics of Fluids*, Vol. 14, No. 10, October 1971, pp. 2074–2080.

[13] Squire, H. B., "The Growth of a Vortex In Turbulent Flow," *Aeronautical Quarterly*, Vol. 16, August 1965, pp. 302–306.

[14] Owen, P. R., "The Decay of a Turbulent Trailing Vortex," *The Aeronautical Quarterly*, Vol. 10, February 1969, pp. 69–78.

[15] Kantha, L. H., "Empirical Model of Transport and Decay of Aircraft Wake Vortices," *Journal of Aircraft*, Vol. 35, No. 4, April 1998, pp. 649–652.

[16] Cook, C. V., "The Structure of the Rotor Blade Tip Vortex," Paper 3, Aerodynamics of Rotary Wings, AGARD CP-111, September 13–15, 1972.

[17] Caradonna, F., Hendley, E., Silva, M., Huang, S., Komerath, N., Reddy, U., Mahalingam, R., Funk, R., Wong, O., Ames, R., Darden, L., Villareal, L., and

Gregory, J., "An Experimental Study of a Rotor in Axial Flight," Proceedings of the AHS Technical Specialists' Meeting for Rotorcraft Acoustics and Aerodynamics, Williamsburg, VA, October 28–30, 1997.

[18] Mahalingam, R., and Komerath, N. M., "Measurements of the Near Wake of a Rotor in Forward Flight," AIAA Paper 98-0692, 36^{th} Aerospace Sciences Meeting & Exhibit, Reno, NV, January 12–15, 1998.

[19] McAlister, K. W., "Measurements in the Near Wake of a Hovering Rotor," AIAA Paper 96-1958, Proceedings of 27^{th} AIAA Fluid Dynamic Conference, New Orleans, June 18–20, 1996.

[20] McAlister, K. W., Tung, C., and Heineck, T. J., "Devices that Alter the Tip Vortex of a Rotor," NASA TM2001-209625, 2001.

[21] Boisard, R., and Baeder, J. D., "Impact of Three-Dimensional and Compressible Effects of Blade Loading on BVI Noise Signature," American Helicopter Society 57^{th} Annual National Froum, Washington D.C, May 9-11 2001.

[22] Brand, A. G., "Aerodynamic Analysis and Measurement of a Subwing Blade Tip Shape for Blade-Vortex Interaction Noise Reduction," American Helicopter Society 53^{rd} Annual National Forum, Virginia Beach, VA, April 29–May 1, 1997.

[23] Berry, J., and Bettschart, N., "Rotor-Fuselage Interaction: Analysis and Validation with Experiment," American Helicopter Society 53^{rd} Annual National Forum, Virginia Beach, VA, April 29–May 1, 1997.

[24] Bagai, A., and Leishman, J. G., "A Study of Rotor Wake Development and Wake/Body Interactions in Hover," *Journal of the American Helicopter Society*, Vol. 37, No. 4, October 1992, pp. 48–57.

[25] Crouse, Jr., G. L., *An Analytical Study of Rotor/Airframe Interactions in Hover and Forward Flight,* PhD thesis, University of Maryland, 1992.

[26] Crouse, G. L., Leishman, J. G., and Bi, N., "Theoretical and Experimental Study of Unsteady Rotor/Body Aerodynamic Interactions," *Journal of the American Helicopter Society*, Vol. 37, No. 1, January 1992, pp. 55–65.

[27] Leishman, J. G., and Bagai, A., "Challenges in Understanding the Vortex Dynamics of Helicopter Rotor Wakes," *AIAA Journal*, Vol. 36, No. 7, July 1998, pp. 1130–1140.

[28] Landgrebe, A. J., "The Wake Geometry of a Hovering Rotor and its Influence on Rotor Performance," *Journal of the American Helicopter Society*, Vol. 17, No. 4, October 1972, pp. 2–15.

[29] Iversen, J. D., and Corsiglia, V. R., "Hot-Wire, Laser-Anemometer, and Force Measurements of Interacting Trailing Vortices," *Journal of Aircraft*, Vol. 16, No. 7, July 1979, pp. 448–454.

[30] Schmitz, F. H., "Rotor Noise," In *Aeroacoustics of Flight Vehicles: Theory and Practice*, Vol. 1. NASA Reference Publication, August 1991, Ch. 2, p. 1258.

[31] Gandhi, F., and Tauszig, L., "A Critical Evaluation of Various Approaches for the Numerical Detection of Helicopter Blade-Vortex Interactions," *Journal of the American Helicopter Society*, Vol. 45, No. 3, 2000, pp. 179–190.

[32] Kocurek, J. D., and Tangler, James, L., "Laser Velocimetry and Blade Pressure Measurements of a Blade-Vortex Interaction," *Journal of the American Helicopter Society*, Vol. 40, No. 2, April 1995, pp. 15–23.

[33] Torok, M. S., and Ream, D. T., "Investigation of Empennage Airloads Induced by a Helicopter Main Rotor Wake," American Helicopter Society 49th Annual National Forum, St. Louis, MO, May 19–21, 1993.

[34] Ringler, T. D., George, A. R., and Steele, J. B., "The Study of Blade-Vortex Interaction Sound Generation and Directionality," Proceedings of the AHS Technical Specialists Meeting, Philadelphia, PA, October 1991.

[35] Leishman, J. G., "Aeroacoustics of 2-D and 3-D Blade Vortex Interaction Using the Indicial Method," American Helicopter Society 52*nd* Annual Forum, Washington, DC, June 4–6, 1996.

[36] Lim, J., and Tung, C., "2GCHAS Predictions of HART Blade-Vortex Interaction Loading," Proceedings of the AHS Technical Specialists' Meeting for Rotorcraft Acoustics and Aerodynamics, Williamsburg, VA, October 28–30, 1997.

[37] Ananthan, S., Leishman, J. G., and Ramasamy, M., "The Role of Filament Stretching in the Free-Vortex Modeling of Rotor Wakes," American Helicopter Society 58th Annual National Forum, Montréal, Canada, June 11–13, 2002.

[38] Ramasamy, M., and Leishman, J. G., "The Interdependence of Straining and Viscous Diffusion Effetcs on Vorticity in Rotor Flow Fields," American Helicopter Society 59th Annual National Forum, Phoenix, Arizona, May 6–8 2003.

[39] Quackenbush, T. R., Lam, C. M. G., Wachspress, D. A., and Bliss, D. B., "Analysis of High Resolution Unsteady Airloads for Helicopter Rotor Blades," American Helicopter Society 50^{th} Annual National Forum, Washington, DC, May 11–13, 1994.

[40] Bramwell, A. R. S., Done, G., and Balmford, D., *Bramwell's Helicopter Dynamics* AIAA, Inc., Reston, VA, 2001.

[41] Harris, F. D., "Articulated Rotor Blade Flapping Motion at Low Advance Ratios," *Journal of the American Helicopter Society*, January 1972, pp. 41–48.

[42] Phillips, W. R. C., "The Turbulent Trailing Vortex During Roll-Up," *Journal of Fluid Mechanics*, Vol. 105, 1981, pp. 451–467.

[43] Tung, C., Pucci, S. L., Caradonna, F. X., and Morse, H. A., "The Structure of Trailing Vortices Generated by Model Helicopter Rotor Blades," NASA TM 81316, 1981.

[44] Yu., Y. H., and Tung, C., "The HART-II Test: Rotor Wakes and Aeroacoustics with Higher Harmonic Pitch Control (HHC) Inputs," American Helicopter Society 58th Annual National Forum, Montréal, Canada, June 11–13 2002.

[45] Beddoes, T. S., "A Wake Model for High Resolution Airloads," Proceedings of the 2^{nd} International Conference on Basic Rotorcraft Research, Triangle Park, NC, 1985.

[46] Egolf, T. A., and Landgrebe, A. J., "Helicopter Rotor Wake Geometry and its Influence in Forward Flight, Vol. 1 — Generalized Wake Geometry and Wake Effects in Rotor Airloads and Performance," NASA CR-3726, October 1983.

[47] Lorber, P. F., Stauter, R. C., and Landgrebe, A., "A Comprehensive Hover Test of the Airloads and Airflow of an Extensively Instrumented Model Helicopter Rotor," American Helicopter Society 45^{th} Annual National Forum, Boston, MA, May 22–24, 1989.

[48] Sadler, S. G., "A Method for Predicting Helicopter Wake Geometry, Wake-Induced Inflow and Wake Effects on Blade Airloads," American Helicopter Society 27^{th} Annual National Forum, Washington, DC, May 1971.

[49] Scully, M. P., "Computation of Helicopter Rotor Wake Geometry and Its Influence on Rotor Harmonic Airloads," Massachusetts Institute of Technology Report No. ASRL TR 178-1, March 1975.

[50] Johnson, W., "Airloads, Wakes and Aeroelasticity," AGARD-R-781, November 1990.

[51] Rahier, G., and Delrieux, Y., "Influence of Vortex Model on Blade-Vortex Interaction Load and Noise Predictions," Proceedings of the AHS Technical Specialists' Meeting for Rotorcraft Acoustics and Aerodynamics, Williamsburg, VA, October 28–30, 1997.

[52] Kraft, C. C., "Flight Measurements of The Velocity Distribution and Persistence of the Trailing Vortices of an Airplane," NACA TN 3377, 1955.

[53] McCormick, B. W., Tangler, J. L., and Sherrieb, H. E., "Structure of Trailing Vortices," *Journal of Aircraft*, Vol. 5, No. 3, July 1968, pp. 260–267.

[54] Rose, R., and Dee, W. F., "Aircraft Vortex Wake and Their Effects on Aircraft," Aeronautical Research Council Report No. CP-795, 1965.

[55] Corsiglia, V. R., Schwind, R. G., and Chigier, N. A., "Rapid Scanning, Three Dimensional Hot Wire Anemometer Surveys of Wing-Tip Vortices," NASA CR-2180, 1973.

[56] Baker, G. R., Barker, S. J., Bofah, K. K., and Saffman, P. G., "Laser Anemometer Measurements of Trailing Vortices in Water," *Journal of Fluid Mechanics*, Vol. 65, 1974, pp. 325–336.

[57] Ciffone, D. L., and Orloff, K. L., "Far-Field Wake-Vortex Characteristics of Wings," *Journal of Aircraft*, Vol. 12, No. 5, May 1975, pp. 464–470.

[58] Lamb, H., *Hydrodynamics*, 6th ed., Cambridge University Press, Cambridge, 1932.

[59] Iversen, J. D., "Correlation of Turbulent Trailing Vortex Decay Data," *Journal of Aircraft*, Vol. 13, No. 5, May 1976, pp. 338–342.

[60] Rayleigh, L., "On the Dynamics of Revolving Fluids," *Proc. Roy. Soc. London Ser*, Vol. 93, 1880, pp. 148–154.

[61] Bradshaw, P., "The Analogy Between Streamline Curvature and Buyoyancy in turbulent Shear Flows," *Journal of Fluid Mechanics*, Vol. 36, 1969, pp. 177–191.

[62] Baldwin, B. S., Chigier, N. A., and Sheaffer, Y. S., "Decay of Far-Flowfield in Trailing Vortices," AIAA 2nd Atmospheric Flight Mechanics Conference, Palo Alto, California, Sep 11–13 1972, 72-989.

[63] Donaldson, C. D., "Calculation of Turbulent Shear Flows for Atmospheric and Vortex Motions," AIAA Paper 71-217, AIAA 9^{th} Aerospace Sciences Meeting, 1971.

[64] Hoffman, E. R., and Joubert, P. N., "Turbulent Line Vortices," *Journal of Fluid Mechanics*, Vol. 16, 1963, pp. 395–411.

[65] Cotel, A. J., and Breidenthal, R. E., "Turbulence Inside a Vortex," *Physics of Fluids*, Vol. 11, No. 10, October 1999, pp. 3026–3029.

[66] Cotel, A. J., "Turbulence Inside a Vortex: Take Two," *Physics of Fluids*, Vol. 14, No. 8, August 2002, pp. 2933–2934.

[67] Bhagwat, M. J., and Leishman, J. G., "Correlation of Helicopter Tip Vortex Measurements," *AIAA Journal*, Vol. 38, No. 2, February 2000, pp. 301–308.

[68] Martin, P. B., Leishman, J. G., Pugliese, G., and Anderson, S., "Stereoscopic PIV MEasurements in the Wake of a Hovering Rotor," American Helicopter Society 56^{th} Annual National Forum, Virginia Beach, VA, May 2–4, 2000.

[69] Leishman, J. G., "Measurements of the aperiodic wake of a hovering rotor," *Experiments in Fluids*, Vol. 25, 1998, pp. 352–361.

[70] Gurusul, I., and Xie, W., "Origin of Vortex Wandering over Delta Wings," *Journal of Aircraft*, Vol. 37, No. 2, 2000, pp. 348–350.

[71] Heineck, J. T., Yamauchi, G. K., Wadcock, A. J., and Lourenco, L., "Application of Three-Component PIV to a Hovering Rotor Wake," American Helicopter Society 56^{th} Annual National Forum, Virginia Beach, VA, May 2000.

[72] Bagai, A., and Leishman, J. G., "Flow Visualization of Compressible Vortex Structures Using Density Gradient Techniques," *Experiments in Fluids*, Vol. 15, 1993, pp. 431–442.

[73] Bagai, A., Moedershiem, E., and Leishman, J. G., "Developments in the Visualization of Rotor Wakes using the Wide-Field Shadowgraph Method," *Journal of Flow Visualization & Image Processing*, Vol. 1, No. 3, July–Sept. 2003, pp. 211–233.

[74] Bhagwat, M. J., and Leishman, J. G., "On the Stability of the Wake of a Rotor in Axial Flight," American Helicopter Society 56^{th} Annual National Forum, Virginia Beach, VA, May 2–4, 2000.

[75] Bhagwat, M. J., and Leishman, J. G., "Measurements of Bound and Wake Circulation on a Helicopter Rotor," *Journal of Aircraft*, Vol. 37, No. 2, March-April 2000, pp. 227–234.

[76] Bhagwat, M. J., and Leishman, J. G., "On the Relationship between the Blade Lift and the Tip Vortex Characteristics," American Helicopter Society 54^{th} Annual National Forum, Washington, DC, May 20–22, 1998.

[77] Bhagwat, M. J., Martin, P. B., Franke, M., and Leishman, J. G., "Flow Visualization and Measurements in the Wake of a Rotor with a Subwing Tip," American Helicopter Society 55^{th} Annual National Forum, Montréal, QC, May 25–27, 1999.

[78] Coyne, A. J., Bhagwat, M. J., and Leishman, J. G., "Investigation into the Rollup and Diffusion of Rotor Tip Vortices using Laser Doppler Velocimetry,"

American Helicopter Society 53rd Annual National Forum, Virginia Beach, VA, April 29–May 1, 1997.

[79] Han, Y. O., Leishman, J. G., and Coyne, A. J., "On the Turbulent Structure of a Tip Vortex Generated by a Rotor," *AIAA Journal*, Vol. 35, No. 3, March 1997, pp. 477–485.

[80] Boatwright, D. W., "Three-Dimensional Measurements of the Velocity in the NearFlow Field of a Full-Scale Hovering Rotor," Mississippi State University EIRS-ASE-74-4, 1974.

[81] Devenport, W. J., Rife, M. C., Liapis, S. I., and Follin, G. J., "Turbulence Structure and Scaling in Trailing Vortices," AIAA Paper 95-0588. 33rd AIAA Aerospace Sciences Meeting & Exhibit, Reno, NV, January 9–12, 1995.

[82] Chigier, N. A., and Corsiglia, V. R., "Tip Vortices – Velocity Distributions," American Helicopter Society 27th Annual National V/STOL Forum, Washington, DC, May 1971.

[83] Chigier, N. A., and Corsiglia, N. A., "Wind Tunnel Data for Wing Trailing Vortex Flow Survet," NASA TM X-62,148, May 1972.

[84] Newman, B. G., "Flow in a Viscous Trailing Vortex," *The Aeronautical Quarterly*, Vol. 1, May 1959, pp. 167–188.

[85] Lezius, D. K., "Water Tank Study of the Decay of Trailing Vortices," *AIAA Journal*, Vol. 12, No. 8, August 1974, pp. 1065–1071.

[86] Caradonna, F. X., and Tung, C., "Experimental and Analytical Studies of a Model Helicopter Rotor," *Vertica*, Vol. 5, 1981, pp. 149–161.

[87] Tangler, J. L., Wohlfeld, R. M., and Miley, S. J., "An Experimental Investigation of Vortex Stability, Tip Shapes, Compressibility, and Noise for Hovering Model Rotors," NASA CR-2305, September 1973.

[88] Tangler, J. L., "The Design and Testing of a Tip to reduce Blade Slap," American Helicopter Society 31^{st} Annual National Forum, Washington, DC, May 13–15, 1975.

[89] Tangler, J. L., "Schlieren and Noise Studies of Rotors in Forward Flight," American Helicopter Society 33^{rd} Annual National Forum, Washington, DC, May 9–11, 1977.

[90] Tangler, J. L., "Experimental Investigation of the Subwing Tip and Its Vortex Structure," NASA CR-3058, November 1978.

[91] Vatistas, G. H., Kozel, V., and Mih, W. C., "A Simpler Model for Concentrated Vortices," *Experiments in Fluids*, Vol. 11, 1991, pp. 73–76.

[92] Kaufmann, W., "Uber die Ausbreitung kreiszlindrischer Wirbel in zahen Flussigkeiten," *Ing. Arch.*, Vol. 31, No. 1, 1962, p. 1.

[93] Saffman, P. G., *Vortex Dynamics* Cambridge University Press, Cambridge, U.K, 1992, Ch. 1.

[94] Martin, P. B., Bhagwat, M. J., and Leishman, J. G., "Strobed Laser-Sheet Visualization of a Helicopter Rotor Wake," Paper PF118, Proceedings of PSFVIP-2, Honolulu, HI, May 1999. Also, *Journal of Flow Visualization & Image Processing* (in press).

[95] Light, J. S., and Norman, T., "Tip Vortex Geometry of a Hovering Helicopter Rotor in Ground Effect," American Helicopter Society 45th Annual National Foru, 22-24, May 1989.

[96] Leishman, J. G., "On Seed particle Dynamics in Tip Vortex Flows," *Journal of Aircraft*, Vol. 33, No. 4, July/August 1996, pp. 823–825.

[97] Barrett, R. V., and Swales, C., "Realization of the Full Potential of the Laser Doppler Anemometer in the Analysis of Complex Flows," *Aeronautical Journal*, Vol. 102, No. 1016, 1998, pp. 313–320.

[98] Leishman, J. G., "On the Aperiodicity of Helicopter Rotor Wakes," *Experiments in Fluids*, Vol. 25, 1998, pp. 352–361.

[99] Heyes, A. L., Jones, R. F., and Smith, D. A. R., "Wandering of Wing Tip Vortices," 12th International Symposium on Applications of Laser Techniques to Fluid Mechanics, Lisbon, Portugal, 12-15, July 2004.

[100] Gurusul, I., and Xie, W., "Origin of Vortex Wandering over Delta Wings," *Jpornal of Aircraft*, Vol. 37, No. 2, April 1999, pp. 348–350.

[101] Bhagwat, M. J., and Leishman, J. G., "Generalized Viscous Vortex Core Models for Application to Free-Vortex Wake and Aeroacoustic Calculations," Proceedings of the 58th Annual Forum of the American Helicopter Society International, Montréal Cananda, June 11–13 2002.

[102] Devenport, W. J., Rife, M. C., Liapis, S. I., and Follin, G. J., "The Structure and Development of a Wing-Tip Vortex," *Journal of Fluid Mechanics*, Vol. 312, 1996, pp. 67–106.

[103] Martin, P., and Leishman, J. G., "Trailing Vortex Measurements in the Wake of a Hovering Rotor with Various Tip Shapes," Proceedings of the 58th Annual Forum of the American Helicopter Society International, Montréal Canada, June 11–13, 2002.

[104] Holzapfel, A. Hofbauer, T., Gerz, T., and Schumann, U., "Aircraft Wake Vortex Evolution and Decay in Idealized and Real Environtments: Methodologies, Benefits and Limitations," Proceedings of the Euromech Colloquium, 2001.

[105] Cotel, A. J., Gjestvang, J. A., RamKhelawan, N. N., and Breidenthal, R. E., "Laboratory Experiments of a Jet Impinging on a Stratified Surface," *Experiments in Fluids*, Vol. 23, No. 2, June 1997, pp. 155–160.

[106] Schlichting, H., *Boundary Layer Theory*, 7th ed., McGraw-Hill, 1979.

[107] Townsend, A. A., "Equilibrium Layers and Wall Turbulence," *Journal of Fluid Mechanics*, Vol. 11, 1961, p. 97.

[108] Batchelor, G. K., and Townsend, A. A., "The Nature of Turbulent Motion at Large Wake Numbers," Proceedings of the Royal Society, London, 1949, A199, pp. 238–255.

[109] Oseen, C. W., "Uber Wirbelbewegung in Einer Reibenden Flussigkeit," *Ark. J. Mat. Astrom. Fys.*, Vol. 7, 1912, pp. 14–21.

[110] Jacob, J., Savas, O., and Liepmann, D., "Trailing Vortex Wake Growth Characteristics of a High Aspect Ratio Rectangular Airfoil," *AIAA Journal*, Vol. 35, 1995, p. 275.

[111] Jacob, J., Savas, O., and Liepmann, D., "Experimental Investigation of Forced Wake Vortices on a Rectangular Wing," AIAA Paper 96-2497, 14th AIAA Applied Aerodynamics Conference, New Orleans, LA, June 1996.

[112] Scully, M. P., and Sullivan, J. P., "Helicopter Rotor Wake Geometry and Airloads and Development of Laser Doppler Velocimeter for Use in Helicopter Rotor Wakes," Massachusetts Institute of Technology Aerophysics Laboratory Technical Report 183, MIT DSR No. 73032, August 1972.

[113] Scully, M. P., "A Method of Computing Helicopter Vortex Wake Distortion," Massachusetts Institute of Technology Report No. ASRL TR 138-1, June 1967.

[114] Vatistas, G. H., "New Model for Intense Self-Similar Vortices," *Journal of Propulsion and Power*, Vol. 14, No. 4, April 1998, pp. 462–469.